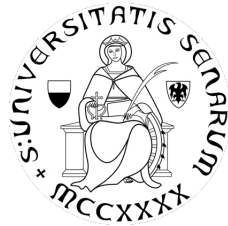


Università degli Studi di Siena

DIPARTIMENTO DI SCIENZE FISICHE DELLA TERRA E DELL'AMBIENTE
SEZIONE DI FISICA



Tracking and Identification of Proton and Helium in CALET and Perspectives for Flux Measurements

Tesi di Dottorato di Ricerca in Fisica Sperimentale

In Partial Fulfillment of the Requirements for the Ph.D. Degree in Experimental Physics

Candidate:
Paolo Brogi

Supervisor:
Prof. Pier Simone Marrocchesi

Tutor:
Dr. Paolo Maestro

Ciclo di Dottorato XXVII

Contents

Introduction	5
1 Cosmic-Ray physics	9
1.1 A brief introduction to Cosmic Rays	9
1.2 Energy Spectrum and composition	12
1.3 Acceleration mechanism and possible sources	18
1.3.1 An introduction to Fermi mechanism	20
1.3.2 Second order Fermi mechanism	21
1.3.3 First order Fermi mechanism	24
1.3.4 UHECRs and the Hillas criterion	27
1.4 Cosmic-Ray propagation in our galaxy	28
1.4.1 The transport equation	29
1.4.2 A simplified model: The Leaky-Box	33
2 The CALorimetric Electron Telescope	39
2.1 The experiment on the ISS	40
2.2 The telescope	42
2.2.1 Charge detector	43
2.2.2 Imaging calorimeter	46
2.2.3 The total absorption calorimeter	50
2.3 The CALET trigger	51
2.4 The CALET acceptances and geometrical factors	54
2.5 Monte Carlo simulation of the CALET telescope	55

3	CALET expected performances and main physics goals	59
3.1	Main anticipated performances of the CALET telescope	59
3.1.1	Energy and angular resolution	60
3.1.2	Electron-proton discrimination	61
3.2	The CALET physics program	65
3.2.1	Search for electron nearby sources	66
3.2.2	All-sky gamma ray survey	69
3.2.3	Search for Dark Matter candidates	70
3.2.4	Study of the nuclear component of cosmic rays	75
3.2.5	The detection of ultra-heavy nuclei	78
4	Tracking with the IMC detector	81
4.1	The combinatorial Kalman filter	82
4.2	Implementation of a Kalman filter tracking algorithm for the IMC . .	84
4.3	IMC tracking performances	88
4.3.1	Fluka simulated data	89
4.3.2	Beam test data	94
5	Charge measurement with the IMC	101
5.1	Reconstruction of the interaction point	102
5.2	Particle identification	108
5.2.1	The truncated mean method	108
5.2.2	The probability method	111
5.2.3	The log-likelihood ratio method	115
5.3	Performance of helium-proton discrimination	117
5.4	Helium-proton discrimination combining IMC and CHD information .	123
5.5	Performances of charge tagging with test beam data	127
6	The Proton and Helium fluxes measurement	131
6.1	Brief overview of proton and helium spectra	132
6.1.1	Recent measurement from PAMELA and AMS-02	137
6.2	Expected CALET performances	141

6.2.1	An estimate of proton and helium events in CALET	142
6.2.2	Flux measurements perspectives with the CALET telescope .	146
	Present status of CALET	155
	Conclusions	157
	Brief summary of candidate's activity	161
	Acknowledgements	163
	Bibliography	165

Introduction

The CALorimetric Electron Telescope (CALET) is a space based experiment designed for long-term observations of high-energy Cosmic Rays (CRs) on the International Space Station (ISS).

The mission, funded by the Japanese Space Agency (JAXA), in collaboration with the Italian Space Agency (ASI) and NASA, performed the first phase studies in 2007-09, followed by the construction and commissioning of the payload, leading to a successful launch of the instrument on 19 August 2015 from the Tanegashima Space Center (Japan). CALET reached the ISS on 24 August on board of the transfer vehicle (Kounotori-5) and was emplaced on the Exposed Facility of the Japanese Experimental Module (JEM-EF). At the beginning of October the preliminary phase of on-orbit check-out and calibrations were accomplished, without remarkable issues, and at the present time the instrument is in science data mode, transmitting data to the ground stations.

The purpose of the experiment is to perform precise measurements of high energy cosmic rays over a period of five years, to accomplish an extensive physics program that includes the detection of possible nearby sources of high energy electrons; searches for signatures of dark matter both in electron and γ -ray spectra; long exposure observations of cosmic nuclei from proton to iron and trans-iron elements; measurements of the CR relative abundances and secondary-to-primary ratios; monitoring of gamma-ray transients with a dedicated Gamma-ray Burst Monitor (CGBM) and the study of solar modulation.

The telescope is an all-calorimetric instrument, with a total thickness of 30 radiation length (X_0) and 1.3 proton interaction length (λ_I), preceded by a particle identification system. It is composed of two different calorimeters: a fine grained pre-shower,

known as imaging calorimeter (IMC), followed by a total absorption calorimeter (TASC). The individual chemical elements identification is entrusted to a Charge Detector (CHD), designed to provide incident particle charge measurement over a wide dynamic range, from $Z = 1$ to $Z = 40$ with sufficient charge resolution to resolve individual elements. The IMC is a sampling calorimeter, composed of 8 pairs of layers of scintillating fibers (with a squared section of 1 mm^2), arranged along the x and y direction, and spaced out by 7 layers of tungsten plates. It can image the early shower profile and reconstruct the incident direction of cosmic rays with good angular resolution. The TASC is a $27 X_0$ thick homogeneous calorimeter composed of 12 alternate layers of lead-tungstate (PWO) logs, oriented perpendicular to each other to provide $x - y$ coordinates of the shower core. It measures the total energy of the incident particle and discriminates electrons and gamma-rays from hadrons.

In the thesis the candidate describes the research activity performed during his Ph.D. term with the Italian team for the CALET collaboration. The crucial detector for this work was the imaging calorimeter, whereby the candidate has focused most of his efforts in exploiting the IMC capabilities in tracking and charge detection. Moreover he has taken part to three different campaigns of calibrations and tests of the instrument, carried out at the CERN North Area facility in 2012, 2013 and 2015.

The first chapter of the thesis provides an introduction to cosmic-ray physics. Acceleration models and propagation in the galaxy are briefly described. In chapter 2 the main detectors of CALET are described in detail, with a particular attention to the IMC, and to the trigger and acceptance definitions. The following chapter describes the anticipated telescope performances and the experimental program. Starting from the fourth chapter the original work of the candidate is presented, in particular the development of a Kalman filter algorithm for particle tracking is described, as well as its validation with both Monte Carlo and Test Beam data. In chapter 5 it is described the work done to exploit the capability of the IMC detector in reconstructing the particle interaction point, and to accomplish a charge identification, focusing on proton and helium events. Finally in chapter 6 an overview on previous and present spectral measurements of charged cosmic rays is given, in view

of an accurate determination of proton and helium fluxes with CALET from space. In particular, the expected performances of the telescope for tracking and charge identification are discussed, and the anticipated proton and helium spectra in the energy range under investigation are shown, together with their relative statistical uncertainties.

Chapter 1

Cosmic-Ray physics

1.1 A brief introduction to Cosmic Rays

Nowadays, it is well known that Earth is under a continuous bombardment of radiation incoming from outer space. However this phenomenon was completely unknown until about a century ago. The existence of cosmic radiation was discovered by Victor Hess [1], an Austrian physicist, who in 1912 measured the rate of ionization in the atmosphere at an altitude of 5300 meters, with an historic balloon flight, and found that it was about three times larger than at sea level. Hess concluded that there was an unknown ionizing radiation penetrating the atmosphere and coming from space. The existence of this radiation and its cosmic origin were then confirmed in 1925 by Robert Millikan, that for the first time named it “Cosmic Rays” (CRs). The nature of CRs was first believed to be purely electromagnetic, because high energy photons, at that time, were believed to be the most penetrating radiation. It was only after the discovery of the geomagnetic effect, noticed for the first time by J. Clay [2] in 1927 and then confirmed from many other experiments, that the nature of primary cosmic rays as charged particles became evident. In fact the modulation of CRs intensity with latitude indicates that they are deflected by the geomagnetic field and proves indeed that they have an electric charge. The discovery of the “East-West effect”, measured in the 1930s by three different experiments [3–5], shows that low energy cosmic rays incoming from the East direction are suppressed if compared to those from the West. This could be explained with the presence of the Earth’s

magnetic field, that prevents certain “forbidden” trajectories and as consequence proves that primaries CRs are mainly composed by positive charged particles. At present, we know that these charged particles are mostly (at the level of $\sim 99\%$) fully stripped ions of atomic elements, with the remaining 1% dominated by electrons. The composition of cosmic-ray nuclei includes about 89% of protons, 10% of helium and heavier nuclei for the remaining 1%.

From the early 1930s till the 1950s, the experimental study of cosmic rays provided a great boost to particle physics until the advent of high-energy particle accelerators, that became an artificial source of high energy particles providing a more controlled environment to test specific processes. In 1932, using a cloud chamber placed into a magnetic field, Carl Anderson was able to discover the existence of the positron [6], the anti-particle of electron, in the flux of atmospheric cosmic rays. This was the first experimental evidence of anti-matter, theorized by Dirac a few years earlier. This achievement was of extreme importance for particle physics, and was soon followed by the discovery of the muon (Anderson, 1937), and of other subatomic particles like the pion, the kaon, hyperons and several more. This huge variety of subatomic particles is produced in the collisions of high energy primary CRs (coming from space) with the atoms of the upper atmosphere generating, via cascade processes, showers of secondary particles propagating down to the ground. These secondary cosmic rays include kaons and pions (that quickly decay to produce muons, neutrinos and gamma rays), as well as electrons and positrons produced by muon decay and by gamma ray interactions with the atmospheric atoms.

The existence of these “air showers” was reported for the first time in 1937 by Pierre Auger, who experimentally detected [7] a large number of coincidences (in excess of the expected accidental rate) between widely separated detectors on the ground. This implied that the incoming cosmic shower was originated by a single event upstream.

Another important contribution to cosmic rays astrophysics is due to Enrico Fermi, who in 1949 proposed an interesting model of their origin [8], describing a mechanism - now referred to as second-order Fermi acceleration - capable to accelerate charged particles moving through an interstellar magnetic field (“magnetic clouds”). This

mechanism is not able to explain how cosmic rays could reach the very high energies recorded by the experiments, but in 1977 theorists realized that Fermi acceleration is particularly efficient in the case of shocks from Supernova Remnants (SNR). This process, known as first-order Fermi acceleration, could explain the observed high energy CRs.

Nowadays, after more than one hundred years from their discovery, the origin, composition and propagation of cosmic rays are still under investigation. The clarification of these phenomena can provide valuable insight to our understanding of the universe and its evolution. Also, particle physicists working at accelerators are looking again into CRs, hoping to get some answers to long standing questions. For instance, many authors believe that a possible signature of the existence of Dark Matter can be found in CR spectra.

Under the name of Dark Matter (DM) we refer to an unobserved part of the mass of the universe, that should exist, because inferred from observations of the CMB and of the rotational dynamics of galaxies: one of the most fascinating open problems in Physics. Most popular models of DM postulate the existence of neutral Weakly Interacting Massive Particles (WIMPs), that would account for non-baryonic (yet gravitating) mass. In this case it is possible that a signature of WIMPs decays might one day be seen in CRs.

At the present time, the experimental study of CRs is carried out along three main different paths: space and balloon experiments for the direct identification and detection of primary cosmic rays; indirect detection (where the nature of the primary is inferred statistically via models of their interactions with the atmosphere) by large ground experiments, that measure the extended air showers (EAS) produced by high energy CRs (mostly above 10^{14} eV); under-ground/water/ice facilities to investigate neutrinos and muons. Ground experiments are based both on large area detectors arrays, to measure directly the shower at ground level, and on optical instruments, to measure atmospheric Cherenkov and fluorescence lights produced by the shower during its development through the atmosphere. Experiments carried by air balloons or aboard satellites or the ISS, have to be, for obvious reasons, as compact and lightweight as possible, designed to identify the incoming particles and to measure

their charge, energy and direction.

1.2 Energy Spectrum and composition

The main topics in present cosmic ray research include the investigation of the acceleration sources and their localization, the study of the acceleration mechanism (especially at very high energies) and of the particle propagation in the interstellar medium (ISM).

For these reasons it is of fundamental importance to characterize the elemental composition of CRs flux and their energy spectra, hence the interest in this type of measurements, not only in the light of interpretation of the past experiments but with an eye at present and future instruments.

For CRs energy spectrum we mean the particle flux (i.e. mean number of events per unit surface, time and solid angle) reaching the Earth, in dependence on energy. To a first approximation, the all-particle flux is found to follow roughly a decreasing power law (eq. 1.1) with spectral index α , spanning a wide range both in energy (about 11 orders of magnitude) and intensity (which decrease by more than 30 orders of magnitude according to energy).

$$\frac{dN}{dE} \propto E^{-\alpha} \quad (1.1)$$

The power law behaviour of the all-particle spectrum, shown in figure 1.1, is distinctive of a non thermal origin for the accelerated particles. Above a few GeV, it does not exhibit any relevant spectral structure, decreasing rather featureless with $\alpha \approx 2.7$ until a spectral break – with a slight change of slope and known as the “knee” – appears at about 4×10^{15} eV. The power-law behavior is usually taken as evidence of an unique acceleration mechanisms for cosmic rays, at least in the region below the knee. The origin of the latter is still unclear, despite the many theoretical models trying to explain it.

For low energies, up to about 1 GeV per nucleon, the spectrum is not described by a power law, due to Solar Modulation. The intensity of this modulation depends on

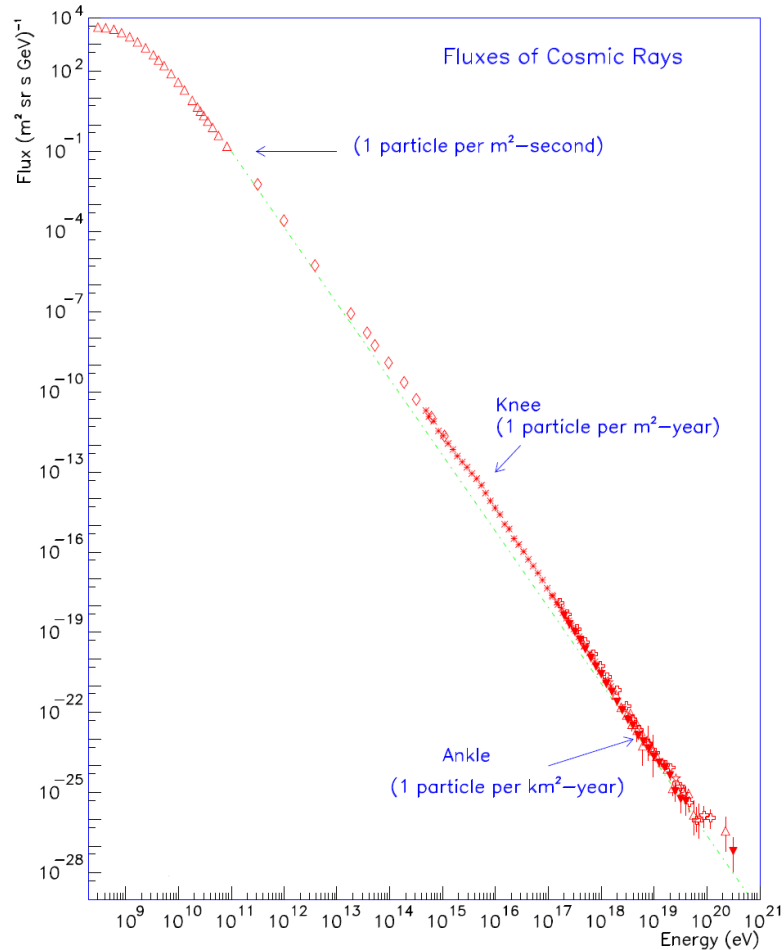


Figure 1.1: The cosmic-ray spectrum for all particles inclusively.

solar activity with CR flux increasing during periods of low solar activity and vice versa, as low energy particles are influenced by the effects of the solar wind and its transport in the Earth magnetosphere.

At energies above 10^9 eV, the “knee” – located approximately at ~ 4.5 PeV and where the spectral index α changes from ~ 2.7 to ~ 3.1 – is not the only noticeable spectral feature. In fact other structures are present at higher energies, they are more evident in figure 1.2, where the all-particle energy spectrum is multiplied by $E^{2.6}$ to highlight any small change of α .

At about 400 PeV there is the so called “second knee”, where the spectrum seems to have a second drop to $\alpha \approx 3.3$. However, the presence of this second knee is not so evident and its existence is still under debate.

Moving to higher energies, in the region close to 10^{19} eV, there is another spectral

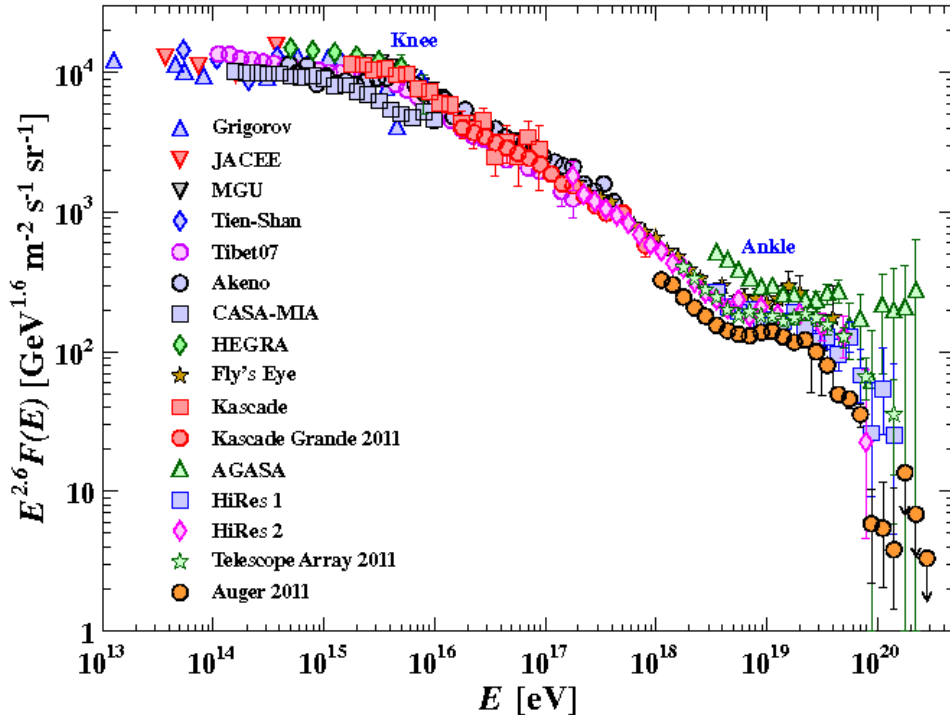


Figure 1.2: The inclusive particle spectrum as a function of E (energy-per-nucleus) [9].

feature, known as the “ankle”, where the spectrum rises again to $\alpha \approx 2.7$, before reaching a region where the spectrum rolls off. This picture emerges from the data at about 5×10^{19} eV and is often associated with the GZK effect [10, 11].

Current popular models on CRs origin hypothesize that particles with energies below the knee are produced in the Galaxy via acceleration in supernova remnants (SNR) [12]. In this case the knee may reflect the maximum acceleration energy reached by a galactic source, but could also be a consequence of the magnetic containment of CRs in the galaxy. The latter follows from calculation of the gyro-radius [13] due to the Lorentz force with an average galactic magnetic field of $3 \mu\text{G}$ (measured with different techniques [14, 15]). In fact, for energies above the PeV, it is expected that particles start to leak off the galaxy, and this can contribute to the steepening of the spectrum.

Some models try to explain the acceleration of particles in the energy region between

the knee and the ankle with effects taking place in the galaxy. For example Bell and Lucek [16] suggested that the magnetic field in SNR can be amplified non-linearly by the interaction with the accelerated cosmic rays to a value many times larger than the pre-shock value. In this way, it is estimated that the protons could reach energies up to 10^{17} eV and also the acceleration rate could significantly increase. Another model by Biermann and Casinelli [17] explains the possibility that explosions of Wolf-Rayet stars could push particle energies up to 3×10^{18} eV. Moreover, similar energies could be attained also by a new class of trans-relativistic supernovae (TRSNe) [18], recently observed in association with gamma-ray bursts.

In the domain of Ultra High Energy Cosmic Rays (UHECRs), i.e. in the region of the ankle and above, extragalactic sources are to be considered as the dominant contribution to the cosmic rays flux. In particular, a number of extragalactic sources are proposed to be responsible for the acceleration in the ankle region [19], including: Active Galactic Nuclei (AGN), Gamma Ray Bursts (GRB), Gravitational Accretion Shocks, Neutron Stars, Pulsars, Black Holes, Colliding Galaxies, Giant Radio Galaxies and Cluster of Galaxies.

Looking at energies of about 5×10^{19} eV, above the ankle, the CRs flux seems to exhibit a cut-off. This behaviour might denote an upper limit for the energy of particles, as pointed out in 1966 by Greisen, Zatsepin and Kuzmin.

The GZK effect is attributed to the presence of the cosmic microwave background radiation (CMB). In particular, it is predicted that an energy of 5×10^{19} eV might be the threshold for the production of a Δ resonance in the interaction between the CMB photons (γ_{CMB}) and the cosmic rays (protons), with photo-disintegration:

$$\gamma_{CMB} + p \rightarrow \Delta^+ \rightarrow p + \pi^0$$

$$\gamma_{CMB} + p \rightarrow \Delta^+ \rightarrow n + \pi^+$$

The produced Δ^+ can decay both into a proton or a neutron (plus the pion), but since neutrons then decay into protons, this is essentially only an energy loss mechanism for protons. Obviously, the energy lost by the proton via the GZK effect depends on the propagation distance through the CMB, and it is possible to calculate that

particles reach the GZK limit at about 100 Mpc from the source [20], to be compared with the radius of our Galaxy which is about 20 kpc.

Finally, it is important to notice that, so far, only particles with energies up to ~ 100 TeV could be directly measured with balloon or space experiments, as present instruments have a typical detection area not exceeding of 1 m^2 . Therefore the measurement of higher energy events would require a too long exposure time, due to the small fluxes. For this reason, energies above the PeV scale could only be explored so far by observing extensive air showers with ground based experiments, using the atmosphere as a calorimeter. This technique allow to increase considerably the detection area and to reach energies in the order 10^{20} eV. However, with ground experiment it is not possible to detect directly the incoming particle, and its nature must be inferred from the observation of the shower parameters. This implies, in particular, to rely on Monte Carlo simulations to parametrize the atmospheric shower development with consequently large systematic uncertainties.

The other feature that characterizes cosmic rays is their composition, i.e. the relative abundances of the different species in the particles flux. As already mentioned, CRs are mainly protons, but also include heavier nuclei, electrons, photons and neutrinos. One of the most interesting thing is to measure the elemental composition of the nuclear part of the cosmic radiation and to compare it with the relative abundances of the chemical elements in the solar system. This is shown in figure 1.3. At first look, the relative abundances of the different elements seem very similar both in the solar system and in the CRs (notice also that in the figure the ordinate is in logarithmic scale). Also, the odd-even effect (well known and arising from nuclear stability) is visible in cosmic ray composition, as well as in the chemical elemental abundance. This indicates that cosmic particles are nothing but regular matter accelerated to high energies.

However some important differences appear at a more detailed observation. In particular a lack of H and He in the cosmic radiation, and an over-abundance of two groups of elements, the ones with masses directly below carbon (Li, Be, B) and the ones below iron (Sc, Ti, V). These elements are almost absent in the solar system while their presence in CRs is relevant (similar considerations apply also to elements

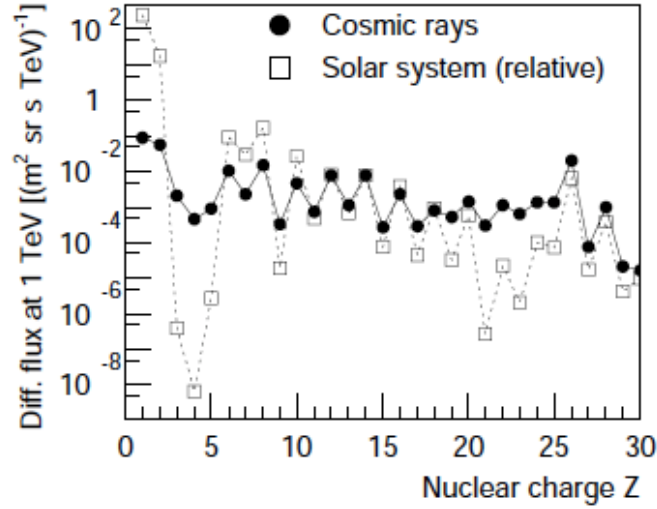


Figure 1.3: Abundance of elements (with $Z \leq 28$) in CRs (at 1 TeV) compared with the solar system composition [21].

below Pb, that are not shown in figure). The under-abundance of He and H is not really understood at the moment. A possible explanation is that these nuclei are harder to ionize (and consequently to accelerate) with respect to the heavier ones or maybe it could reflect the composition of the source itself [15,22].

The other differences instead can be explained with the interaction of the nuclei from the source (*primaries*) with the interstellar medium. This process, known as “spallation”, causes the fragmentation of *primaries* (i.e. Fe, C and O) to produce *secondaries* as for instance Li, Be, B for C, O and Sc, Ti, V, Cr, Mn for Fe. As these *secondaries* elements are essentially not produced in nucleosynthesis, taking into account their relative abundance with respect to *primaries*, it is possible to estimate the amount of material traversed by cosmic rays in their path from the source to the Earth.

One of the most important measurements in this sense is the ratio of B over C. As carbon is produced only in nucleosynthesis, and boron only by spallation of C, this ratio provides a very important constraint to verify propagation models. Moreover, using the values of the spallation cross sections and working in the opposite direction it is possible to infer the composition at the sources.

Another important piece of information to study CRs propagation is given by the

measurement of long-lived radioactive isotopes produced by spallation with the ISM (again). These radioactive nuclei can be used like “propagation clocks”. In fact, by comparing them with the relative amounts of stable *secondaries* (e.g. ^{10}Be with respect to ^9Be), it is possible to infer the confinement time of cosmic rays in the galaxy and to investigate the quantity of matter encountered by particles.

At low energies the fluxes are large enough to allow the measurement, by direct detection, of the spectra species by species. This is shown in figure 1.4, for *primary* CRs.

1.3 Acceleration mechanism and possible sources

One of the main unknown topic in cosmic rays physics is their origin and the mechanism that allows the acceleration of a such great number of charged particles up to extremely high energies. A possible mechanism to explain cosmic-ray acceleration has to meet at least three basic requirements. The first one is obviously to be able to reproduce the energy spectrum. Then, it has to explain the chemical abundances of elements and the extremely high energies of about 10^{20} eV reached. Finally a good candidate model must be efficient enough to accelerate a relatively large number of CRs.

At the moment, the most promising scheme to explain the acceleration of charged particles in space is the Fermi mechanism. This method was originally proposed in 1949 by Enrico Fermi [8] in his “second order” formulation. It is based on the fact that charged particles can stochastically gain energy in head-on collisions with moving magnetic clouds in the galaxy, which are capable to deflect them acting as “magnetic mirrors”. This process does predict a power law spectrum, but in this hypothesis the mechanism is not efficient enough to explain the observed cosmic ray spectrum.

A way to circumvent this problem is to consider acceleration in shock phenomena as in the case of supernova remnants blast waves [23], leading to the formulation of the “first order” Fermi mechanism. In this scheme particles crossing the shock front are accelerated in a much more efficient way, and the spectral features of CRs could

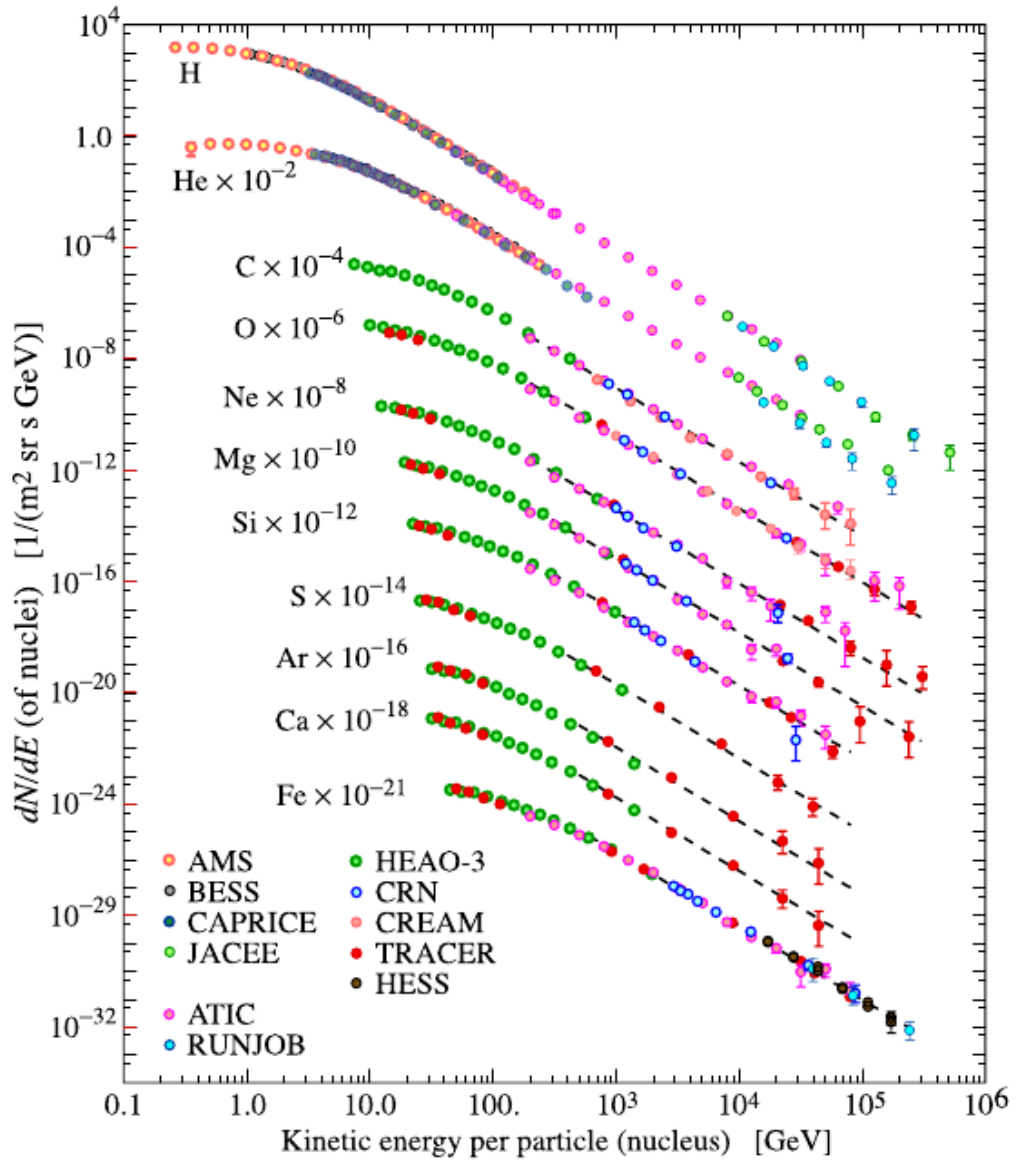


Figure 1.4: Fluxes of primary cosmic nuclei depending on E, from measured data [9].

be reproduced at least for energies below the knee.

This is one of the reasons for which SNRs are considered, at the moment, the most promising sources of acceleration. Another main argument to support this hypothesis is a general consideration of energy balance, originally proposed in 1934 by Baade and Zwicky [24] and then again in 1964 by Ginzburg and Syrovasky [25]. The idea is that from the observed total energy densities of CRs $\rho_{CR}^E \approx 1 \text{ eV/cm}^3$ (about 0.83 eV/cm^3 from protons only and $\sim 0.27 \text{ eV/cm}^3$ from He and heavier nuclei) the power required to supply the CRs measured intensity can be calculated as:

$$W_{CR} = \frac{\rho_{CR}^E V_G}{\tau_c} \approx 5 \cdot 10^{33} \text{ J/s}$$

where the volume of the galaxy is $V_G \approx \pi R^2 d \approx \pi \cdot (15 \text{ kpc})^2 \cdot (200 \text{ pc}) \approx 4 \cdot 10^{66} \text{ cm}^3$ and τ_c is the confinement time of cosmic rays in the galaxy, estimated in about $6 \cdot 10^6$ years. On this basis it is possible to conclude that only a few percent of the energy released in supernova explosions is needed to support CRs acceleration at the observed intensity, as the 2-3 events per century expected to occur on average in our galaxy, are capable of a total power estimated in about $3 \cdot 10^{35} \text{ J/s}$.

1.3.1 An introduction to Fermi mechanism

Due to the importance of the previously mentioned Fermi acceleration mechanism, a brief excursus to describe in more detail how it works is in order [26].

The main concept, on which Fermi (both first and second) acceleration mechanism rely, is that a particle can gain a certain amount of energy, proportional to its current energy, in an acceleration cycle:

$$\Delta E = \epsilon E \tag{1.2}$$

this means that the total energy of the particle after n “cycles” is:

$$E = E_0(1 + \epsilon)^n \tag{1.3}$$

or alternatively:

$$n = \frac{\ln(E/E_0)}{\ln(1 + \epsilon)} \quad (1.4)$$

gives the number n of cycles needed to the particle to reach a certain energy E .

If P is the probability that the particle undergoes another acceleration ($P = 1 - P_{esc}$, where P_{esc} is the escape probability from the acceleration region), the number N of particles that remain after n acceleration cycles is:

$$N = N_0 P^n \quad (1.5)$$

where N_0 is the initial number of particles.

Now we can do some algebra and substitute the 1.4 into the 1.5:

$$\ln(N/N_0) = n \ln P = \frac{\ln(E/E_0) \ln P}{\ln(1 + \epsilon)} = \ln(E_0/E)^\alpha \quad \Rightarrow \quad \frac{N}{N_0} = \left(\frac{E_0}{E}\right)^\alpha \quad (1.6)$$

with

$$\alpha = -\frac{\ln P}{\ln(1 + \epsilon)}. \quad (1.7)$$

Because N is the number of particles with energy $\geq E$ (for construction), if the equation 1.6 is differentiated with respect to energy E , the resulting energy spectrum is:

$$\frac{dN(E)}{dE} \propto E^{-(1+\alpha)}. \quad (1.8)$$

This result shows that this mechanism of repeated acceleration cycles, with an energy gain proportional to the particle energy itself, leads naturally to a power law spectrum. The spectral index depends on the characteristics of the accelerating source.

In the following, this process is described in more detail for two different environments in which it can take place.

1.3.2 Second order Fermi mechanism

In the first paper on this subject [8] Fermi proposed that particles, during their travel along the galaxy, can collide into moving magnetized clouds, that can act as

“magnetic mirrors” scattering the particles back, after a diffusion process inside the cloud itself. This scattering is not due to the particle’s interaction with the matter of the cloud, because of the low density of the plasma in this environment, but it is a consequence of the irregular magnetic fields present in the cloud, so the incoming particle does not lose its energy.

Basically it is possible to distinguish between two different cases: the “head-on” collisions, whereby the cloud and the particle move toward each other, and the “tail” collisions, when the particle catch up the cloud that is moving in the same direction (thanks to its much larger velocity). In head-on collisions the particle energy increases, at expense of the cloud, but (due to its approximately infinite mass) the cloud energy loss can be neglected, and its velocity doesn’t change after the collision. On the other hand in tail collisions the particle loses energy in favour of the cloud.

As an example it is convenient to take a simplified mono dimensional version of the problem [15], but the result holds also in more complex cases. In this scheme, if the cloud is moving with velocity V , then the energy of the particle in the reference frame of the cloud can be written as:

$$E' = \gamma_{cl}(E + Vp) \quad \text{where:} \quad \gamma_{cl} = \sqrt{1 - \frac{V^2}{c^2}} \quad (1.9)$$

and the three-momentum is:

$$\mathbf{p}' = \gamma_{cl}\left(\mathbf{p} + \frac{\mathbf{V}E}{c^2}\right). \quad (1.10)$$

Now, we take into account that the collision conserves the particle’s energy ($E'_{before} = E'_{after}$), while the momentum reverses its sign ($\mathbf{p}'_{before} = -\mathbf{p}'_{after}$). Therefore, if the energy is transformed back to the observer’s frame:

$$E'' = \gamma_{cl}(E' + Vp') \quad (1.11)$$

with a little of manipulation it can be expressed in the form:

$$E'' = E + 2\gamma_{cl}^2 E \frac{V}{c} \left(\frac{V}{c} + \frac{v}{c} \right) \quad (1.12)$$

where v is the particle's velocity. From the 1.12 it follows:

$$\Delta E = 2\gamma_{cl}^2 E \frac{V}{c} \left(\frac{V}{c} + \frac{v}{c} \right) \quad (1.13)$$

that in case of a “tail” collision (with the consequent energy loss) becomes:

$$\Delta E = -2\gamma_{cl}^2 E \frac{V}{c} \left(\frac{v}{c} - \frac{V}{c} \right) \quad (1.14)$$

but, since there is a lower probability to have a tail than a head-on collision, on average this process leads to an increase of the particle's energy.

The collision probability is $\frac{1}{2}(V + v)/v$ in the head-on case and $\frac{1}{2}(v - V)/v$ in the other one, as it depends on the relative velocity between the cloud and the particle, that is: $(V + v)$ if they are moving one against the other and $(v - V)$ if the particle is “overtaking” the cloud. The resulting average energy gain per collision is then:

$$\Delta E = -\frac{1}{2} \left(\frac{v + V}{v} \right) 2\gamma_{cl}^2 E \frac{V}{c} \left(\frac{v + V}{c} \right) - \frac{1}{2} \left(\frac{v - V}{v} \right) 2\gamma_{cl}^2 E \frac{V}{c} \left(\frac{v - V}{c} \right) \quad (1.15)$$

that simplifies in:

$$\frac{\Delta E}{E} = 4\gamma_{cl}^2 \left(\frac{V}{c} \right)^2 \quad (1.16)$$

and for a non-relativistic cloud speed $V \ll v$ it becomes:

$$\frac{\Delta E}{E} = 4 \left(\frac{V}{c} \right)^2 = 4\beta_{cl}^2. \quad (1.17)$$

With a more complete derivation, taking into account also the angle of incidence between the particle and the cloud, it is possible to show that [22]:

$$\epsilon = \frac{\Delta E}{E} \sim \frac{4}{3}\beta_{cl}^2. \quad (1.18)$$

Because of the dependence by the square of β , this is called second-order Fermi mechanism, and it is a very slow acceleration process (notice that $\beta \ll 1$).

To calculate the spectral index from equations 1.7 it is possible to show that:

$$\alpha = -\frac{\ln\left(\frac{1}{1-P_{esc}}\right)}{\ln(1+\epsilon)} \approx \frac{P_{esc}}{\epsilon} = \frac{1}{\epsilon} \frac{\tau_{acc}}{\tau_{esc}} \quad (1.19)$$

where τ_{acc} and τ_{esc} are the characteristic time of the acceleration cycle and the escape time from the acceleration region respectively, while their ratio is the probability per encounter to escape from the acceleration region (P_{esc}). Thus if $\tau_{acc} \sim \frac{1}{c\rho_{cl}\sigma_{cl}}$, the equation 1.8 becomes:

$$\frac{dN(E)}{dE} \propto E^{-\left(1+\frac{4}{3}\beta_{cl}^2 c\rho_{cl}\sigma_{cl}\tau_{esc}\right)} \quad (1.20)$$

where the cosmic-ray velocity is approximated with c and ρ_{cl} , σ_{cl} are the density and the cross-section of the cloud, respectively. There is to notice that the spectral index is not unique, but it depends on the details of the acceleration process.

1.3.3 First order Fermi mechanism

It seems evident that one of the main disadvantages of the previously described (second order) mechanism is that particles can lose energy in following collisions: this leads to a dependence from the square of β and thus to a very slow process. This issue can be solved in the case of collisions which are exclusively head-on: in this case, from expression 1.13 the energy gain is $\sim 2\frac{V}{c}$, first order in $\beta = \frac{V}{c}$, that is precisely what we mean by “first order” Fermi mechanism. It is a much more efficient process to accelerate particles, and can occur in the presence of strong shock waves [27, 28] (e.g. plasma shocks of supernova remnants). For strong shocks we mean a propagation velocity v much larger than the speed of sound in the ISM, that is $v_s \sim 10 \text{ Km} \cdot \text{s}^{-1}$ (this holds true for SNR where $v \sim 10^4 \text{ Km} \cdot \text{s}^{-1}$).

With a calculation [15] similar to the one used to derive equation 1.13, in the case of normal incidence between the particle and the shock front, the energy gain in one

acceleration cycle turns out to be:

$$\bar{\epsilon} = \left\langle \frac{\Delta E}{E} \right\rangle = 2 \frac{\Delta v}{c} \quad (1.21)$$

where it is assumed that the particle's velocity is approximately c , and $\Delta v = v_1 - v_2$ is the difference of the velocities of the gas flow upstream (1) and behind (2) the shock. A more complex derivation, taking into account all the possible angles of incidence between the cosmic ray and the shock front, leads to the following result:

$$\bar{\epsilon} = \frac{4}{3} \frac{\Delta v}{c}. \quad (1.22)$$

Now, in order to obtain the spectral index generated by this first order process it is clear – from expressions 1.8 and 1.7 – that the other quantity needed is the escape probability (\bar{P}_{esc}) of the particle from the accelerating region. From a simple argument of classical kinetic theory [27], it follows that:

$$\bar{P}_{esc} = \frac{4u_2}{c} \quad (1.23)$$

These results (equations 1.22 and 1.23) allow to obtain the spectral index, according to the approximation of eq. 1.19, as:

$$\alpha \approx \frac{\bar{P}_{esc}}{\bar{\epsilon}} = \frac{3}{v_1/v_2 - 1} \quad (1.24)$$

Since it is known that the density enhancement upon crossing the shock [29] is:

$$\frac{\rho_2}{\rho_1} = \frac{\gamma + 1}{\gamma - 1} \quad (1.25)$$

and that the mass flow through the shock must be conserved (Rankine-Hugoniot equation):

$$\rho_1 v_1 = \rho_2 v_2 \quad (1.26)$$

It is possible to calculate that $\rho_2/\rho_1 = v_1/v_2 = 4$, because the ratio γ of the specific heats, for a fully ionized gas is $5/3$.

Thus, substituting $v_1/v_2 = 4$ in 1.24 a value of $\alpha = 1$ is obtained and consequently from equation 1.8, one gets:

$$\frac{dN(E)}{dE} \propto E^{-2} \quad (1.27)$$

which is the spectrum predicted by a first order Fermi acceleration mechanism.

Although the observed exponent of 2.7 is not reproduced, the spectral index arising from first order processes is only mildly dependent of the acceleration environments condition. This means that a variety of different sources can produce almost the same spectrum, resolving one of the critical aspect of second order mechanism. For this reason, as well for its greater efficiency and capability of reproduce the CRs spectral shape, the first order Fermi model is considered as the most likely mechanism of acceleration of cosmic rays, at least below $10^{14} - 10^{18}$ eV. In fact, it is possible to calculate an upper limit for the energy that this method allows to attain in a SNR environment.

A particle, that encounters a propagating supernova blast wave, is accelerated as described previously, gaining an amount of energy ($\propto E$) each time that it crosses the shock front from upstream to downstream and vice versa, accomplishing a “cycle”. It is obvious that the maximum energy is attained by the particle that does not escape from the shock, but that continues its acceleration “cycles” for all the time τ in which the blast wave is active. In this limit, and assuming a minimal diffusion length equal to the Larmor radius of the particle, the maximum achievable energy is:

$$E_{max} \approx ZeB\tau\beta_{shock}^2 \quad (1.28)$$

where Ze is the charge of the particle and B is the magnetic field behind and ahead of the shock. If we assume $\tau \sim 1000$ years, $B = B_{ISM} \sim 3\mu\text{G}$ and a Type II supernova explosion, the upper limit implied by equation 1.28 is [30]:

$$E_{max} \approx Z \cdot 100 \text{ TeV} \quad (1.29)$$

However, for some particular type of supernova, more recent calculations [31] predict

a maximum energy of:

$$E_{max} \approx Z \cdot 5 \text{ PeV} \quad (1.30)$$

In conclusion, first order acceleration from SNR seems to work well in describing the CRs spectrum below the “knee” (see figure 1.1), while it fails to account for larger energies. However, in the energy domain above 10^{18} eV, the particle’s Larmor radius r_L in the galactic magnetic field is comparable in size with the galactic disk. For this reason, a transition from galactic to extra-galactic cosmic rays is expected at these energies, and new sources can be involved in the CRs production.

1.3.4 UHECRs and the Hillas criterion

To understand what kind of sources can allow for the acceleration of Ultra High Energy CRs up to more than 10^{20} eV, a simple geometrical argument can be used. As the acceleration of a UHECR inside a candidate source can take place only as long as it is contained within the dimension of the source itself, this leads to the “Hillas criterion” [32]. If a candidate source have an extension R and a magnetic field B , a simple “pre-selection” criterion states that:

$$r_L(E_{max}) \leq R \quad (1.31)$$

where r_L is the Larmor radius of the accelerated particle.

Since it is known that $r_L \approx E/ZeB$ for a nucleus of charge Ze , it is possible to rewrite the equation 1.31 as follows:

$$E_{max} \leq ZeBR. \quad (1.32)$$

The result obtained using this criterion can be visualised with the “Hillas plot” shown in figure 1.5, where protons are the accelerated CRs, and candidate sources are plotted in a $B - R$ “phase-space” plane.

From this plot it results evident that most astrophysical objects are not able to reach the energy limit of the observed spectrum. Source candidates that pass the Hillas requirement are neutron stars, Active Galactic Nuclei (AGN), lobes of giant

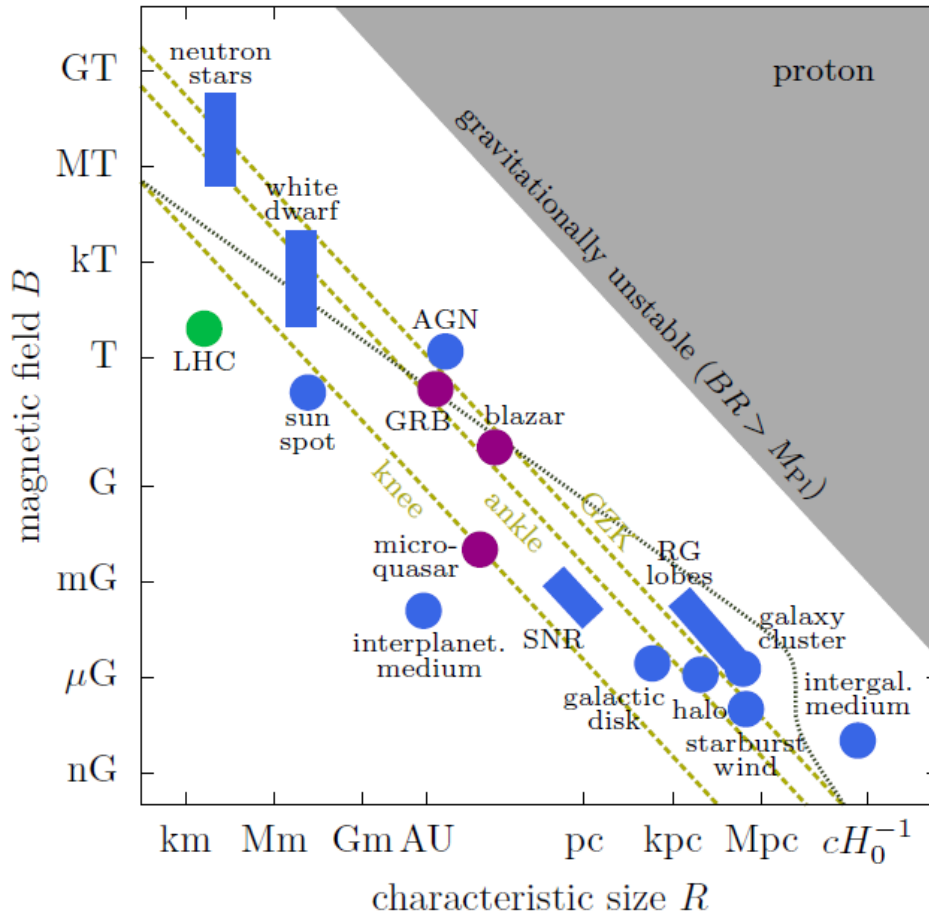


Figure 1.5: The Hillas plot, for various CR source candidates. Both axis are in logarithmic scale [33].

radio-galaxies, and accretion shocks in the intergalactic medium.

Clearly, Hillas criterion is a necessary, but not sufficient, condition for a certain astrophysical object to be a source of UHECRs.

1.4 Cosmic-Ray propagation in our galaxy

In the previous sections, only the acceleration and generation of cosmic rays at the sources were taken into account. However, on their way from the sources to us, CRs undergo numerous physical processes, including: diffusion along magnetic field lines, scattering on magnetic irregularities, energy losses, radioactive decays and interactions with the interstellar gas. These effects need to be taken into account to explain the cosmic-ray spectra observed at Earth, and to infer the original spectra

at the source. This section is dedicated to describe the propagation of cosmic ray in our galaxy.

1.4.1 The transport equation

Nowadays the diffusion model, with the inclusion of convection, is considered the most adequate tool to provide the description of cosmic rays propagation in the galaxy (for energies below $\sim 10^{17}$ eV).

In this scheme, the general transport equation for a selected nucleus is written in the form [34]:

$$\begin{aligned} \frac{\partial \psi(\mathbf{r}, p, t)}{\partial t} = & Q(\mathbf{r}, p, t) + \nabla \cdot (D_{xx} \nabla \psi - \mathbf{V}_c \psi) + \frac{d}{dp} p^2 D_{pp} \frac{d}{dp} \frac{1}{p^2} \psi \\ & - \frac{\partial}{\partial p} \left[\dot{p} \psi - \frac{p}{3} (\nabla \cdot \mathbf{V}_c) \psi \right] - \frac{1}{\tau_f} \psi - \frac{1}{\tau_r} \psi \end{aligned} \quad (1.33)$$

where:

- $\psi(\mathbf{r}, p, t)$ is the particle density per unit of momentum p at position \mathbf{r} and at time t ;
- $Q(\mathbf{r}, p, t)$ is the source term, that include the contributions of primaries, spallation reactions and decays;
- D_{xx} is the spatial diffusion coefficient;
- \mathbf{V}_c is the convection velocity, due to the Galactic wind;
- D_{pp} is the diffusion coefficient in momentum space, describing the re-acceleration process;
- finally τ_f and τ_r represent the time scales for fragmentation losses and radioactive decays respectively.

Clearly, for the injection part, the isotopic composition and spectrum at the sources are needed. The primaries injection spectrum is supposed to be a power law in momentum (see 1.34) for all the nuclei, with the exponent γ that can vary from one

element to another.

$$dQ(p)/dp \propto p^{-\gamma} \quad (1.34)$$

While the isotopic composition is usually based on the primordial solar composition, it can be modified to take account of the measured composition of the CR themselves. A subset of $Q(\mathbf{r}, p, t)$ describes the fragmentation of primary species into lighter element. This process is known as “spallation” and (for relativistic nuclei), in first approximation, it conserves the kinetic energy per nucleon of the progenitor. The source contribution from spallation $Q_s(\mathbf{r}, p)$ depends on the cross sections $\sigma(E)$ and the gas density ρ of all the progenitor species. If H and He are assumed as the only relevant targets for spallation (due to their relative abundance in the ISM), this source term can be written as:

$$Q_s(\mathbf{r}, p) = \beta c \psi_p(\mathbf{r}, p) [\sigma_H^{sp}(p) \rho_H(\mathbf{r}) + \sigma_{He}^{sp}(p) \rho_{He}(\mathbf{r})], \quad (1.35)$$

where $\sigma_H^{sp}(p)$, $\sigma_{He}^{sp}(p)$ are the production cross sections from the progenitors (on H and He targets respectively), ψ_p is the progenitor density, and ρ_H , ρ_{He} are the interstellar hydrogen and helium densities.

The coefficient D_{xx} describes the isotropic diffusion, which is a function of \mathbf{r} , β and of the rigidity $R = p/z$ (i.e. momentum per unit of charge which determines the Larmor radius in a given magnetic field).

Furthermore, during propagation, when cosmic rays scatter on random magnetic fields, they can be re-accelerated via the second order Fermi mechanism. This process is described in the transport equation as diffusion in momentum space and is related to the diffusion coefficient D_{pp} , that can be estimated [35,36] as:

$$D_{pp} = \frac{p^2 V_A^2}{9 D_{xx}}, \quad (1.36)$$

where V_A is the Alfvén velocity, the characteristic velocity of weak disturbances propagating in a magnetic field.

It is worth to notice that equation 1.33 is time dependent, but often the steady-state solution is required. It can be obtained with two procedures: by setting $\partial\psi/\partial t = 0$

or following the time dependence until a steady state is reached. This second way has the advantage that is much easier to implement numerically. The time dependence of Q instead can be neglected if the stochastic nature of sources or nearby recent sources are not studied.

Moreover, different boundary conditions can be chosen for several models, depending on the scope of the model. A usual assumption is $\psi = 0$ at the “halo boundary”, an approximation that neglects the intergalactic flux and that has to be relaxed for models interested in a physical treatment of the boundary.

To understand the CR spectra observed experimentally at Earth, one has to solve the transport equation not only for primaries but also for secondaries, tertiaries, etc. To do this, one can start from the solution for the heaviest primaries and then use the result to compute the spallation of their products, and so on, solving iteratively the complete system.

At this point, the complete solution can be compared with direct observations. Also solar modulation can be included if required.

The propagation of cosmic electrons, positrons and anti-protons can be considered as special cases of equation 1.33, in fact they differ from the treatment of nuclei only for energy losses and production rates. For nuclei, the losses in the ISM are mainly due to ionization, Coulomb scattering, fragmentation and radioactive decays. For electrons, in addition to ionization and Coulomb scattering, the main relevant processes include bremsstrahlung, Compton and synchrotron losses.

The solution for stable secondaries

Stable secondary cosmic rays have a very important role in the study of the propagation mechanism, as they are produced only in the intergalactic medium via spallation and are not affected by radioactive decay.

For this reason, the decay term in equation 1.33 can be neglected. In addition, also the term $\frac{\partial}{\partial p} \dot{p} n$ is set to zero, in the approximation of no ionization losses, which is valid above several GeV/n.

Then, in order to work with the steady state solution of the transport equation, the CRs intensity is supposed to be constant in time. As many experiments suggest [37],

it has not changed significantly in the last hundred million years.

Moreover, for simplicity, also re-acceleration processes and the effect of the galactic wind (which in any case seems not to be relevant in our galaxy) are neglected. In other words, we can set $D_{pp} = 0$ and $\mathbf{V}_c = 0$.

Taking into account all these approximations, the transport equation 1.33 can be written, for any given element i , in the form:

$$Q_i + \nabla \cdot (D_i \nabla \psi_i) - \frac{1}{\tau_i} \psi_i + \sum_{j>i} \frac{P_{ji}}{\tau_{j \rightarrow i}} \psi_j = 0 \quad (1.37)$$

where τ_i is the spallation lifetime of the i -th species (consequently the term $\frac{1}{\tau_i} \psi_i$ describes the spallation losses). In the last term, P_{ij} is the probability that in an inelastic collision the nucleus j , with spallation lifetime τ_j , is destroyed and the element i is created. Thus, the term $\sum_{j>i} \frac{P_{ji}}{\tau_{j \rightarrow i}} \psi_j$ describes all nuclei with $j > i$ which give contributions to ψ_i .

Alternatively, if one describes the spallation contributions in terms of inelastic cross sections, instead of lifetimes, equation 1.37 transforms to:

$$Q_i + \nabla \cdot (D_i \nabla \psi_i) - \rho_H \beta c \sigma_i \psi_i + \sum_{j>i} \rho_H \beta c \sigma_{k \rightarrow i} \psi_j = 0 \quad (1.38)$$

where ρ_H represent the hydrogen density in the ISM (that for simplicity is assumed as the only target for spallation), and $\sigma_{j \rightarrow i}$ is the cross section for the nucleus j to fragment into the nucleus of specie i .

Now it is not unreasonable to assume that the spatial distribution of sources does not depend on the kind of the nucleus. Under this assumption, that can be written as: $Q_i(\mathbf{r}) = q_i \chi(\mathbf{r})$, where q_i are constants related to the abundances of the various nuclei, it is possible to show [22], that equation 1.38 admits solutions of the following type:

$$\psi_i(\mathbf{r}) = \int_0^\infty \psi_i^{(\sigma)}(x) G(\mathbf{r}, x) dx \quad (1.39)$$

where $\psi_i^{(\sigma)}$ and G (which are both function of the parameter x , expressed in g/cm^2), have to satisfy the following equations:

$$m_H \rho_H \beta c \frac{\partial G}{\partial x} - \nabla \cdot (D \nabla G) = 0 \quad \text{with} \quad m_H \rho_H \beta c G(\mathbf{r}, 0) = \chi(\mathbf{r}) \quad (1.40)$$

$$\frac{d\psi_i^{(\sigma)}}{dx} + \frac{\sigma_i}{m_H} \psi_i^{(\sigma)} - \sum_{j>i} \frac{\sigma_{j \rightarrow i}}{m_H} \psi_j^{(\sigma)} = 0 \quad \text{with} \quad \psi_i^{(\sigma)}(0) = q_i \quad (1.41)$$

where m_H is the hydrogen mass, and G must satisfy the same boundary conditions of $\psi_i(\mathbf{r})$, related to the containment volume geometry.

The two equations decouple the astrophysical aspect of the cosmic-ray propagation from the spallation. In fact, G in the expression 1.40 is often called ‘‘path-length distribution’’, and it describes the transport of CRs, being related to the diffusion coefficient (D), to the source distribution ($\chi(\mathbf{r})$) and the ISM structure.

On the other hand, $\psi_i^{(\sigma)}(x)$ represents the variation of the cosmic-ray composition (due only to fragmentation processes) after traversing an amount x of matter, and it is related only to the nuclear cross sections: σ_i and $\sigma_{j \rightarrow i}$.

From equation 1.39, it follows that the cosmic rays density at the position \mathbf{r} is obtained by averaging the composition expressed by $\psi_i^{(\sigma)}(x)$ over the distribution of path lengths $G(\mathbf{r}, x)$ travelled by particles from their sources to the point \mathbf{r} .

1.4.2 A simplified model: The Leaky-Box

One of the first, and more successful, methods to describe cosmic rays propagation is the Leaky Box Model (LBM). In this model [22] the CRs propagate freely in a containment volume, with a constant probability per unit time to escape (τ_{esc}^{-1}). Under some conditions, the LBM can be seen as an approximation of the diffusion model [34].

Usually, under the Leaky-Box model framework, the galaxy is described as a cylinder with thickness about 300-500 pc and radius ~ 8 kpc, with a magnetic field of 3-6 μG . It is assumed that CRs propagate freely inside this containment volume and, when they reach the cylinder boundary, they bounce elastically, but with a finite probability (increasing with the particle’s momentum) to cross the boundary and

escape.

In the Leaky-Box approximation, the diffusion term in equation 1.38 can be replaced with the escape probability from the containment volume:

$$\nabla \cdot (D_i \nabla \psi_i) \rightarrow -\frac{\psi_i}{\tau_{esc}} \quad (1.42)$$

after this substitution is made, and the expression obtained is divided by $m_H \rho_H \beta c$, the set of transport equations for the LBM, can be written as:

$$\frac{Q_i}{m_H \rho_H \beta c} - \frac{\psi_i}{\lambda_i} - \frac{\psi_i}{\lambda_{esc}} + \sum_{j>i} \frac{\psi_j}{\lambda_{j \rightarrow i}} = 0 \quad (1.43)$$

and can be solved analytically.

In the expression 1.43 $\lambda_i = m_H / \sigma_i$ represents the interaction length (expressed in g/cm²) for the considered process with cross-section σ_i , while:

$$\lambda_{esc} = m_H \rho_H \beta c \tau_{esc} \quad (1.44)$$

is the only parameter of the model and it describes the mean amount of matter (in g/cm²), that CRs traverse before they escape from the confinement volume.

This interpretation came naturally from the solution of equation 1.40 in the LBM framework, that is:

$$G_{LBM}(x) \propto \exp^{-x/\lambda_{esc}}. \quad (1.45)$$

While the solution of the transport equation 1.43 for the differential intensity ψ_i of a given specie i is:

$$\psi_i = \frac{1}{\lambda_{esc}^{-1} + \lambda_i^{-1}} \left(\frac{Q_i}{m_H \rho_H \beta c} + \sum_{j>i} \frac{\psi_j}{\lambda_{j \rightarrow i}} \right). \quad (1.46)$$

The secondary-over-primary ratio for λ_{esc} estimation

As explained before, the fundamental parameter for the LBM is λ_{esc} : the escape mean free path from the galaxy. The ratio of stable secondary CRs respect to their primaries can provide an important constraint on this important parameter.

For simplicity only secondary nuclei S with a unique parent nucleus of type P are considered. In this scheme, the set of transport equations 1.43 reduce to a system of two equations:

$$\frac{Q_p}{m_H \rho_H \beta c} - \frac{\psi_P}{\lambda_P} - \frac{\psi_P}{\lambda_{esc}} = 0 \quad (1.47)$$

$$-\frac{\psi_S}{\lambda_S} - \frac{\psi_S}{\lambda_{esc}} + \frac{\psi_P}{\lambda_{P \rightarrow S}} = 0 \quad (1.48)$$

This system can be solved, and the following expression for the secondary-to-primary ratio can be written:

$$S/P = \frac{\psi_S}{\psi_P} = \frac{\lambda_{esc}/\lambda_{P \rightarrow S}}{(1 + \lambda_{esc}/\lambda_S)} \approx \frac{\lambda_{esc}}{\lambda_{P \rightarrow S}} \quad \text{for } \lambda_S \gg \lambda_{esc} \quad (1.49)$$

From this equation it is evident that, in case of a secondary nucleus with a long interaction mean free path, the secondary-to-primary ratio S/P is directly proportional to λ_{esc} .

Therefore, the measured S/P ratio at the Earth can be used to calculate the mean amount of interstellar matter CRs have traversed to reach us, providing also an important constraint to ISM composition and distribution.

For this kind of study, the most important CRs species to take into account are carbon, oxygen and iron, that are primaries and produce respectively lithium, beryllium, boron and *sub - Fe* nuclei as secondaries (from spallation).

In particular, the measurement of the B/C ratio is one of the most important test for the propagation models, since B is purely secondary and have as main progenitor C, a primary. Moreover, as B and C have similar Z , it is less sensitive to systematic errors (including solar modulation at low energies) than other ratios of nuclei with dissimilar charges. The same argument holds also for the sub-iron over iron ratio, although the measurement of this quantity is more difficult, mainly because the relevant fluxes are lower. In figure 1.6 recent data of B/C and *sub - Fe*/ Fe ratios from various experiments are shown.

From the observed relative abundances of stable secondary nuclei with respect to their primaries, and in the framework of the Leaky-Box Model, it is possible to

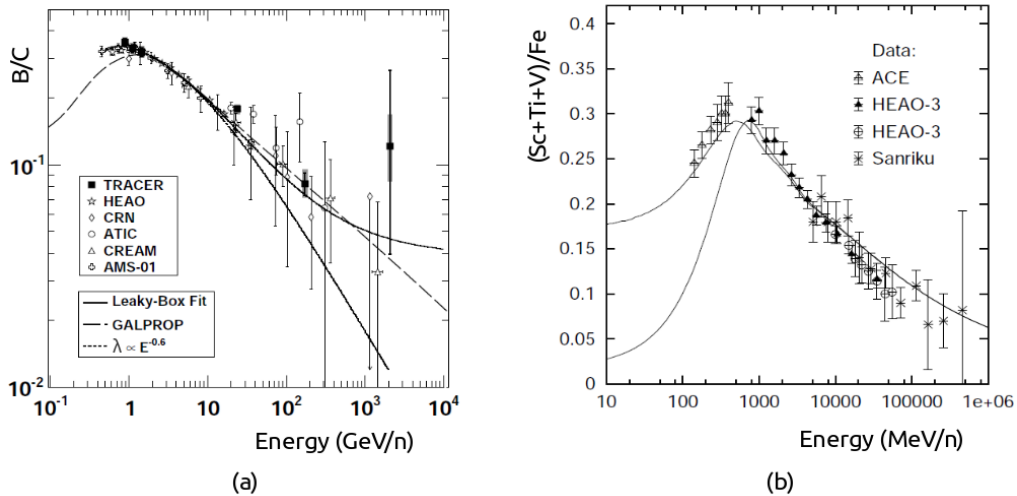


Figure 1.6: a) The B/C ratio as a function of the kinetic energy per nucleon (measured by various experiments [38]) superimposed with the parametrization by [39] (dotted) the GALPROP model (dashed), and a fit to the LBM (solid). b) $sub - Fe/Fe$ ratio as a function of kinetic energy per nucleon, from different measurements [40].

estimate an escape mean free path of:

$$\lambda_{esc} \approx 5-10 \frac{\text{g}}{\text{cm}^2} \quad (1.50)$$

from which it is possible to infer that CRs travel along a distance inside the galaxy that is a factor 10^3 larger than the size of the galaxy itself, before they reach the Earth.

Moreover the energy dependence of the B/C and $(Sc + Ti + V)/Fe$ ratios can be explained if λ_{esc} is of the form [39]:

$$\lambda_{esc}(R) = \frac{26.7\beta \frac{\text{g}}{\text{cm}^2}}{\left(\frac{\beta R}{1.0 \text{ GV}}\right)^\delta + \left(\frac{\beta R}{1.4 \text{ GV}}\right)^{-1.4}} \quad (1.51)$$

where $R = pc/Ze$ is the rigidity, β is the velocity (in units of c) and $\delta \approx 0.5 - 0.6$. The measured B/C suggests also that more energetic particles traverse less matter, as they escape earlier from the galaxy. This is a proof that acceleration occurs before (and not during) the propagation, otherwise this ratio would be constant or increase with energy.

From equation 1.51 it follows that, for high energy particles:

$$\lambda_{esc}(R) = \lambda_0 \left(\frac{R}{R_0} \right)^{-\delta} \quad (1.52)$$

where λ_0 has a typical value of about $10 - 15 \text{ g/cm}^2$ and $R_0 \approx 4 \text{ GV}$ [41].

This means that, due to propagation, the spectra at the Earth should be steeper than at the source: the spectral index γ being reduced by the value of δ .

In other words, the all-particle spectrum observed at Earth with $\gamma \approx 2.7$ suggests that the spectral index of the source is ~ 2.1 , and thus compatible with a CRs acceleration driven by a first order Fermi mechanism (see section 1.3.3).

Furthermore, propagation (i.e. the spallation process) also influences the particle's spectral shape. For this reason, in the hypothesis that all elements have the same energy spectra at the source, the spectra of heavy nuclei, observed at Earth, should be flatter with respect to the ones of light elements [42].

Direct measurements of the energy spectra for different species confirm this expected difference: for instance, the spectral index for protons is measured to be $\gamma_p = -2.71 \pm 0.02$ while for iron $\gamma_{Fe} = -2.59 \pm 0.06$.

Chapter 2

The CALorimetric Electron Telescope

CALET is a Japanese led international collaboration that designed and developed a space experiment to perform direct measurements of high-energy CRs on the International Space Station (ISS). The mission, funded by the Japanese Space Agency (JAXA), in collaboration with the Italian Space Agency (ASI) and NASA, was proposed for the utilization plan of the Exposed Facility (EF) on the Japanese Module (KIBO) of the ISS. The first phase studies started in 2007-09 and led to the successful launch of the detector in August 2015. The expected lifetime of the mission is 2 years with a target of at least 5 years.

The purpose of the CALorimetric Electron Telescope (CALET) is to perform precise measurements of high energy cosmic rays, extending the observations carried out by balloon experiments (as ATIC, TRACER, CREAM), dedicated space missions (like PAMELA, AMS, FERMI, AGILE) and ground based detectors. In particular, it will be able to detect the presence of possible nearby sources of high energy electrons and search for signatures of dark matter. It is expected that CALET will extend the energy reach of present measurements of the secondary to primary ratio (e.g.: boron/carbon and sub-iron/iron), providing information about the energy dependence of cosmic ray propagation in the galaxy. It will also monitor gamma ray transients with a dedicated Gamma-ray Burst Monitor (CGBM) and study solar modulation.

2.1 The experiment on the ISS

The CALET instrument is an all-calorimetric telescope launched on August 19th, 2015 from the Tenegashima Space Center (Japan), with the Japanese HII-B launch carrier. The HTV5 (HII Transfer Vehicle) carrying CALET reached the ISS on August 24th. The instrument was then installed by a robotic arm on the Exposed Facility of the Japanese Experimental Module (JEM-EF), as shown in figure 2.1. After a period of time of a few weeks, needed for degassing, the power-on and on-orbit commissioning procedures of the detector were started and data relayed to the ground stations. At the beginning of October the preliminary calibrations and tests required to start the first science operation period were accomplished, without significant issues. Since October 5th, CALET is collecting science data.

The JEM-EF is a platform of size about $4 \times 6 \text{ m}^2$ directly exposed to outer space,



Figure 2.1: The CALET payload during its installation on the Exposed Facility of the Japanese Experiment Module (credit: JAXA/NASA).

it is designed to host up to 10 experiment payloads at a time, and to provide them electrical power, cooling and data transfer capabilities. The CALET detector [43] is placed on port #9 of the Exposed Facility, one of the two Experimental Facility Units (EFUs) capable of accommodating a large payload with a mass up to 2.5 tons (instead of the 500 kg allowed for standard EFUs). The telescope stands on a standard a pallet of size $1.85 \times 0.8 \times 1.0 \text{ m}^3$, supporting the calorimeter with its

subsystems and allowing the connection to the EFU #9.

Figure 2.2 shows an artistic view of the instrument package inside its Mission Bus Unit (MBU) on the support pallet, that represents the body of the main detector (i.e. the calorimetric telescope) and a number of subsystem including:

- the Flight Releasable Grapple Fixture (FRGF) that provides grapple points for the robotic arm (and the astronauts);
- the Mission Data Controller (MDC) for detector systems management and data handling;
- the Advance Stellar Compass (ASC) and the GPS receiver (GPSR) providing fine position and attitude data;
- the CALET Gamma ray Burst Monitor (CGBM) a sub-detector designed to measure hard X rays and soft γ rays, in a low energy range not covered by the main telescope.

The CGBM [44] consists of two Hard X-ray Monitors (HXMs), for the detection of hard X-rays in the range 7 keV to 1 MeV, and of a Soft Gamma Ray Monitor (SGM) that covers the energy range 100 keV - 20 MeV. Each HXM is comprized of a two-layered scintillator of $\text{LaBr}_3(\text{Ce})$ coupled to a Photo Multiplier Tube (PMT), while the SGM is made of a single BGO crystal again read by a PMT. This sub-detector is designed to provide the capability of Gamma Ray Burst (GRB) observations from the main calorimeter. In fact it is sensitive to lower energy than the telescope, and will allow to measure GRB spectra over a wide range, from X-rays to γ -rays. In addition the CGBM will carry out all-sky observations of various γ -ray transients: soft gamma repeaters, solar flares, terrestrial γ -ray flashes, and X-ray binaries.

The data down link is ensured by two telemetry channels: an Ethernet channel at a medium rate of 600 kbps and a MIL-STD-1553B channel which provides low rate data at 50 kbps. The CALET data are transferred to the JAXA Tsukuba Space Center (TKSC) and independently via the TDRSS satellites system to the US NASA Marshall Space Flight Center, and then sent to the Waseda CALET Operation Center (WCOC) in real time for the on-line monitoring of the events.

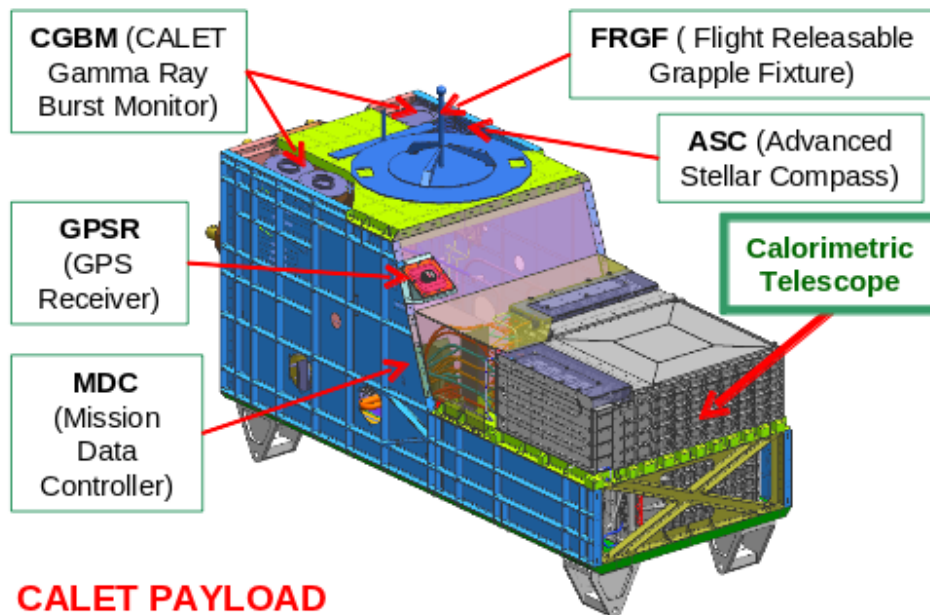


Figure 2.2: The structure of the CALET instrument package.

From the WCOG the data are distributed to the international CALET team for the off-line data analysis.

2.2 The telescope

The CALET main instrument is a completely calorimetric detector, with a total thickness equivalent to 30 radiation length (X_0) and 1.3 proton interaction length (λ_I). The field of view is $\sim 45^\circ$ from the zenith, and the effective geometrical factor is about $1200 \text{ cm}^2\text{sr}$ for high energy electrons.

As it is possible to see in the schematic view of figure 2.3 the telescope is composed of three main subsystems: a charge detector (CHD), an imaging calorimeter (IMC), and a total absorption calorimeter (TASC). The CHD is designed to identify individual chemical elements in the cosmic-ray flux. It is positioned at the top of the CALET instrument, and provides a measurement of the electric charge of the incoming particle via the Z^2 dependence of the specific ionization loss in a double layered, segmented, plastic scintillator array. The IMC follows the charge detector and it is a fine grained pre-shower calorimeter, with tracking capabilities, capable to image the early shower profile and to reconstruct the incoming particle direc-

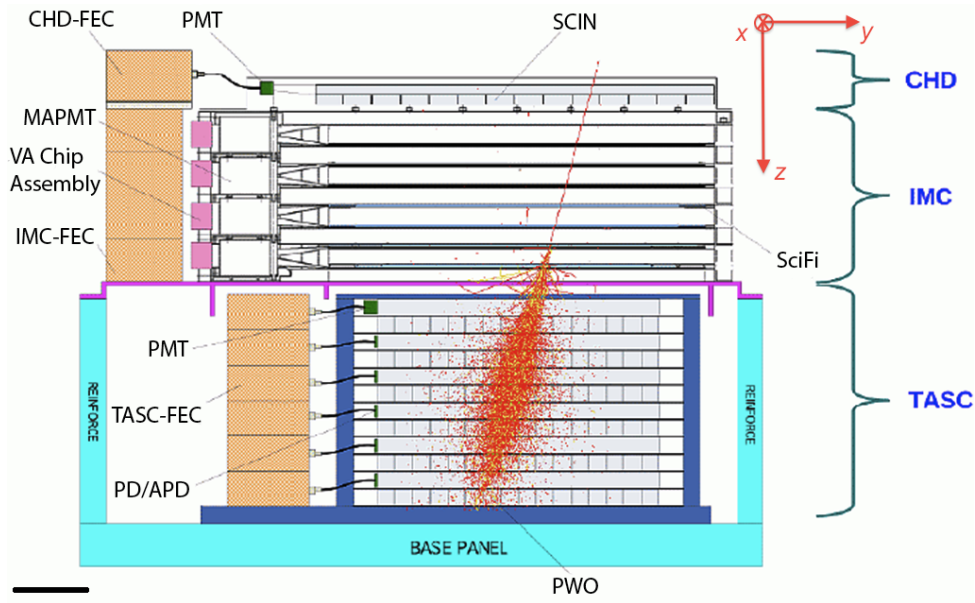


Figure 2.3: Schematic view of the CALET main instrument.

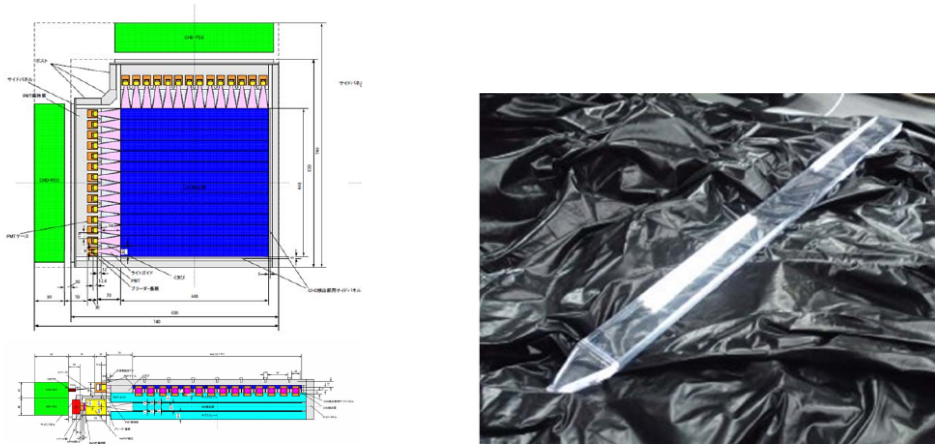
tion. Thanks to its scintillating fibers, readout individually, it can also provide a redundant measurement of charge, useful for a better discrimination of the elemental composition of the cosmic-ray flux. The last part of the telescope is a Total Absorption Calorimeter (TASC), a thick calorimeter (about $27 X_0$) of Lead Tungstate (PWO) crystals, designed to measure the total energy of the incident particle and to discriminate electrons and gamma-rays from hadrons.

Calibrations and tests of the instrument were carried out with extracted beams of the SPS accelerator with beams of electrons, protons and relativistic ions, at the CERN North Area facility, during three different campaigns: in 2012, 2013 and 2015.

2.2.1 Charge detector

This part of the CALET instrument is designed to provide incident particle identification over a large dynamic range for charges from $Z = 1$ to $Z = 40$, with sufficient charge resolution to resolve individual elements.

It consists of two layers of EJ204 plastic scintillators, each segmented into 14 paddles. Each paddle is 32 mm wide x 450 mm long x 10 mm thick. The paddle of the first (top) and of the second (bottom) layer are aligned along the y and x



(a) Schematic layout of the CHD structure. (b) Picture of a EJ204 scintillator paddle with the acrylic light guide.

Figure 2.4: Schematic view of CHD structure and image of a scintillator paddle [45].

directions, respectively. One side of each scintillators is coupled via a light guide to a photomultiplier tube (PMT) Hamamatsu R11823. The $x - y$ segmentation is needed to reduce the background contamination of energy deposits generated by back-scattered radiation from the calorimeters.

In figure 2.4 the structure of the CHD is shown (a) together with the picture of one paddle and its acrylic light guide (b). The paddles are wrapped with reflective Vikuiti ESR films (3M) in order to increase the light collection, and the PMT readout is made with Front End Custom (FEC) electronics, that amplifies, shapes and digitizes the signal. More details on the FEC are given in section 2.2.3, as the CHD and TASC front-end electronics scheme is similar. The CHD paddles have a single channel mono-range readout, while a double channel dual-range readout is employed by the TASC.

Light saturation in a plastic scintillator

When a large energy deposit occurs in a plastic scintillator, effects of light saturation are to be taken into account. This happens when the local density of ionization becomes too large, and the luminescence centres start to “quench”.

For relativistic ions two regions with different energy density can be found along the track: a “core” region, close to the particle trajectory, in which the density is

larger; and an “halo” region, located farther away from the track, where the density is lower and related to energetic δ -rays. In the halo region, the ionization density is compatible with a linear response in Z^2 for the scintillation light yield, while the higher density of the core leads to light saturation effects. The specific scintillation light yield can be parametrized in the scheme of the “Halo model” [46] as:

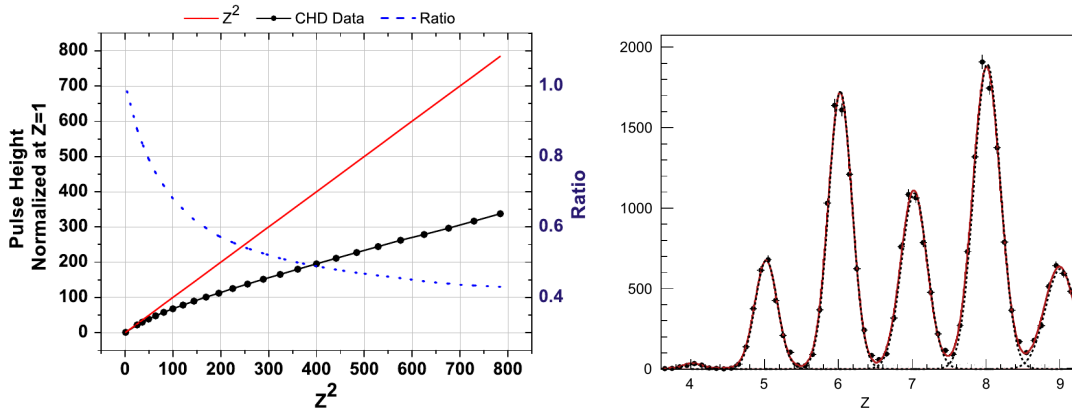
$$\frac{dL}{dx} = \frac{A(1 - f_h)\alpha Z^2}{1 + B_s(1 - f_h)\alpha Z^2} + Af_h\alpha Z^2 \quad (2.1)$$

where the two terms represent the core and the halo contribution, respectively. The two most important parameters of this expression are B_S (related to the strength of the saturation), and f_h representing the fraction of energy deposited in the halo. A is an overall normalization constant, and $\alpha \approx 2\text{MeV/gcm}^{-2}$ for a plastic scintillator.

Some results on the performance of the CHD scintillator, as obtained in a dedicated beam test [47] when a single CHD paddle was tested, are shown in figure 2.5 (a) and (b). In graph (a) the black line (and dots) represent the scintillator signal versus Z^2 , normalized with respect to the average response for a $Z = 1$ particle. Together are plotted the ideal response curve in case of no saturation (solid red line), that exhibits the pure Z^2 dependence, and the fraction of measured signal respect to the expected one (blue line and dots). The blue line shows as the effective loss approaches 60% in the iron region, while from the the fit of the measured signal response (black) with equation 2.1 it is possible to obtain [47] the following values: $f_h = 0.36 \pm 0.01$, $B_S = (8.0 \pm 0.3) \cdot 10^{-3}\text{gcm}^{-2}\text{MeV}^{-1}$ for the parameters of the Halo model. Figure 2.5 (b) instead shows the charge distributions of element from Be ($Z = 4$) to O ($Z = 8$) as measured at the beam test, superimposed with a multi-Gaussian fit of the data. It is possible to define an approximate estimator of the charge resolution with respect to unit charge e , as:

$$\sigma_Q = \frac{\sigma}{\mu_{z+1} - \mu_z} \quad (2.2)$$

where μ_z and σ are the mean and the sigma value of the Gaussian curve, resulting from a fit of the charge distribution, for an element with charge Z . The charge resolutions for elements from $Z = 5$ to $Z = 26$ (from B to Fe) are reported in figure



(a) Response function of the EJ204 scintillator. (b) Charge distributions from the scintillator for Be, B, C, N, O.

Figure 2.5: Some results for EJ204 scintillator obtained at dedicated beam test at GSI. [47].

2.6. The resolution for B is close to $0.15e$, while it is about $0.25 - 0.28e$ in the region from Mg to S, and $\sim 0.3e$ for iron and sub-iron elements. The charge resolution at boron exceeds the requirement for a 5σ separation from carbon, this is of particular interest for CALET as the measurement of the B/C ratio up to a few TeV/n is one of the science goals of the experiment.

Unfortunately, light saturation is not the only issue that can lead to a degradation of the charge measurement with the CHD. There are at least two other important issues: the fragmentation of the incident nucleus inside the detector itself, and the background signal arising from back-scattered particles from the calorimeter. All these issues can lead to a fake charge identification, for this reason a redundant measurement of charge (from the IMC detector) is of great importance for the experiment, and it is one of the main topics of this thesis.

An accurate study of the CHD detector performances and related issues can be found in [48].

2.2.2 Imaging calorimeter

The IMC is a sampling calorimeter positioned immediately below the CHD, that acts as a pre-shower and has imaging capabilities. This detector is crucial for this thesis work, since most of the efforts made during my Ph.D. thesis preparation have

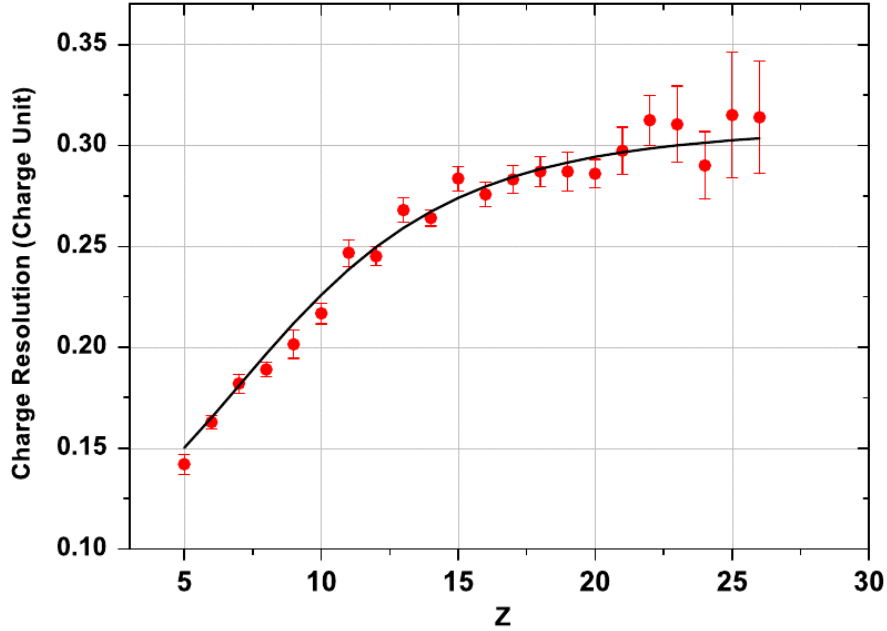
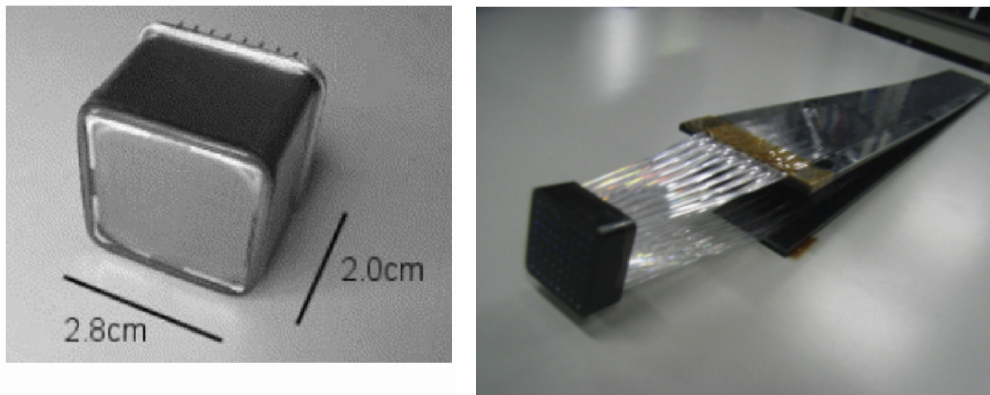


Figure 2.6: Charge resolution for individual elements (from boron to iron) from data taken at GSI with a single CHD paddle [47].

been focused in exploiting its capabilities for tracking and charge detection having as goal a measurement of cosmic-ray proton and helium spectra.

The calorimeter layout is visible in figure 2.3. It is composed of 16 active planes of scintillating polystyrene fibers (SciFi), and of 7 layers of tungsten which acts as absorber. The scintillating fibers have a 1 mm^2 square cross section and are 448 mm long. Each plane is composed of 448 fibres oriented all along the y or the x direction. The 16 planes are then coupled in 8 pairs spaced out by 7 layers of tungsten, and each pair consists of an x and an y plane glued together, to produce a two dimensional information on the position. Two consecutive $x-y$ pairs are spaced 2 cm apart by a honeycomb support structure, while the tungsten plates are placed directly on top of the SciFi pairs. All of the tungsten plates have a squared shape, but differ in dimensions: the first 3 layers, starting from the CHD, have sides of 448 mm (the same as the SciFi planes) and thickness 0.7 mm; the following 2 plates have the same thickness but sides of 384 mm; while the last 2 layers have sides of 320 mm and a thickness of 3.5 mm. The sizes of the absorber plates are such that the last planes can match the TASC dimensions. The thickness of the tungsten, instead, has been chosen to have a fine sampling at the beginning of the calorimeter without a



(a) MA-PMT Hamamatsu R7600-M64. (b) Fiber belts and coupling system.

Figure 2.7: The MA-PMT Hamamatsu R7600-M64 used for the IMC SciFi readout (a), and two 8 fiber belts with the system for the coupling with the MA-PMT (b).

loss in the total thickness. In fact, since the the radiation length X_0 of tungsten is 3.5 mm, the first five pairs of absorber and SciFi provide a sampling every $0.2 X_0$, while the last two level provide a $1.0 X_0$ sampling, for a total thickness of $3 X_0$. This is equivalent to a total depth of about 0.11 times the proton interaction length λ_H .

Each fiber is read out by an Hamamatsu R7600-M64 Multi-Anode Photomultiplier Tube (MA-PMT), shown in figure 2.7, together with two 8-fibers belts with their light guides and support system for the coupling with the PMT. The design of this photomultiplier was customized for the CALET requirements, reducing the number of dynodes from 12 to 8 stages, to extend the dynamic range. The 8 dynodes version showed significantly better linearity performances at the same gain with respect to the standard R5900 [49]. A total of 14 MA-PMT are needed for the read-out of each pair of IMC planes (adjacent along z in the same view).

The front-end electronics for the PMT read-out is based on a dedicated 32 channel Viking VA32-HDR14.3 high density ASIC [50]. This chip has a large dynamic range (up to 15 pC), low power consumption and low noise, and has been developed by a joint effort among Japan, INFN (Italy) and Gamma-Medica Ideas (Norway) [51]. In figure 2.8 it is shown a picture of the IMC at the beam test performed at CERN North Area facility during the 2012 campaign. The SciFi planes are visible, as well as the front-end electronics with their support structure. In the 2012 beam test

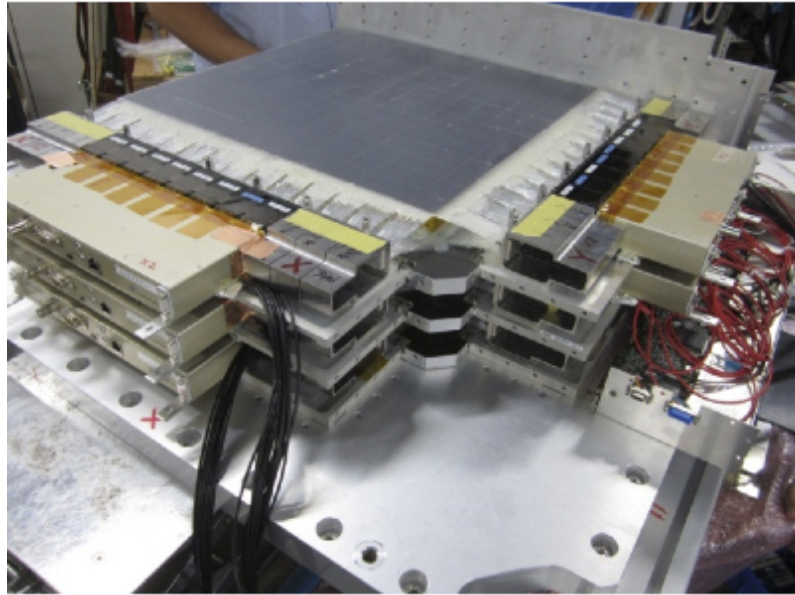


Figure 2.8: Picture of IMC planes and front-end electronics at CERN beam test in 2012.

configuration, the IMC planes was not fully equipped, and only 256 fibers per layer were read out by the electronics. Therefore only 8 MA-PMT for each pair of layers were needed for the SciFi read-out.

To identify easily each layer of the IMC detector a numeration scheme, from 0 to 15, has been adopted, where 0 is the layer nearest to the CHD (top of the CALET instrument) and the planes are numbered in increasing order till 15, which is the layer nearest to the TASC. Thus, following the conventional reference system decided for the CALET detector, as shown in figure 2.3, the planes with an even number, plus zero, provide the measurement of the x coordinate, while the odd planes of the y one. The $x = 0$ and $y = 0$ position corresponds to the center of the active detector layer in the $x - z$ or $y - z$ view, respectively. The origin of the z axis is defined at the top surface of the aluminium cover plate on the top of the CHD, and the positive direction is toward the TASC detector. This means that all layers hold positive values in the z coordinate and layer 0 is at a lower value of z with respect to layer 15.

The IMC is designed to act as a pre-shower, as electrons and γ -rays are likely to interact in the tungsten layers, generating an electromagnetic shower, while only a few protons and nuclei undergo an hadronic interaction, as the IMC depth is equivalent to only $0.11 \lambda_H$. Moreover, the fine granularity of the SciFi allows to determine

the starting point of the electromagnetic shower, which is of great importance both to separate electrons and positrons against the γ background, and for a more precise measurement of the hadronic particles energy.

The IMC is then essential to reconstruct the particle incidence direction and to distinguish between the incident cosmic rays (downward direction) and the backscattered particles (upward direction). Furthermore, this detector should provide a redundant measurement of the particle charge, useful for a better identification of the different nuclear species.

2.2.3 The total absorption calorimeter

The TASC is a homogeneous calorimeter that instruments the last part of the CALET telescope, its total area covers about 1063 cm^2 , and it is composed of 12 layers of lead-tungstate (PWO) logs for a total thickness of $27 X_0$, that corresponds to about $1.23 \lambda_I$ (at normal incidence). Each layer is composed of 16 crystal logs with dimensions $19 \text{ mm} \times 20 \text{ mm} \times 326 \text{ mm}$ length, and it is arranged with the logs oriented along the x or the y direction alternatively. This provide a 3D reconstruction of the showers, with 6 layers imaging the XZ view and 6 the YZ view.

The PWO logs of the upper layer (nearest to the IMC), read out by PMTs, are used to generate a trigger signal, while for the logs of the other layers an hybrid package of silicon Avalanche PhotoDiode (APD) and silicon PhotoDiode (PD) is used to collect light. The dual APD/PD package is shown in figure 2.9 (left), together with the picture of one of the lead-tungstate logs of the TASC (right). This dual sensor is glued at one end of the log and provides a wide dynamic range, together with the read-out system based on Charge Sensitive Amplifier (CSA) with dual gain.

In fact, the main goal of the CALET project is the measurement of the electrons spectrum up to few TeV. This requires a linear energy response from GeV up to the TeV region, an excellent resolution, and a high rejection power of the background protons. In particular, the proton rejection power must be better than 10^5 to observe electrons up to 10 TeV. To match the above requirements, the TASC read-out system needs to span over 6 orders of magnitude, to measure in each bar signals from the threshold of 0.5 MIP up to 10^6 MIPs, i.e. the signal expected from a 1000

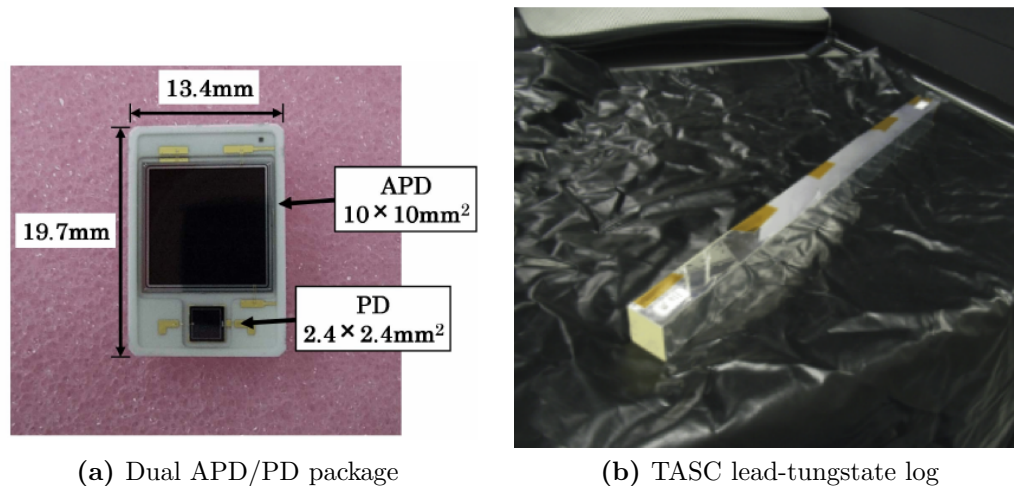


Figure 2.9: (a) APD Hamamatsu S8664-1010, active area of 10 mm × 10 mm, and PD S1227-33BR of 2.4 mm × 2.4 mm [52]. (b) A picture of one of the lead-tungstate logs of the TASC.

TeV shower [52].

The Front-End Circuit, that together with the 2-in-1 package of APD and PD, ensures the required dynamic range is represented by the block diagram in figure 2.10 where it is possible to observe that the outputs of the APD/PD are directly connected to two different CSA, that amplify the signals from each photo-diode. Then, two shaping amplifier circuits, with different gains, are implemented for signal processing from each CSA. Each shaping amplifier has two sections for each input channel with a gain ratio of 30:1, each one is then digitized by a 16-bit Analog to Digital Converter (ADC). With this configuration, the expected dynamic range of the dual APD-PD sensors is from about 0.2 MIP to about 10^7 MIPs.

2.3 The CALET trigger

To take data efficiently under different conditions, three main trigger modes have been defined for the CALET orbital operations on the ISS [53], depending on the target, the incident particles, and the energy.

The CALET trigger is generated by the coincidence of the discriminated analog signals from different detector components, with specific threshold settings (see table 2.1) for the three primary trigger modes:

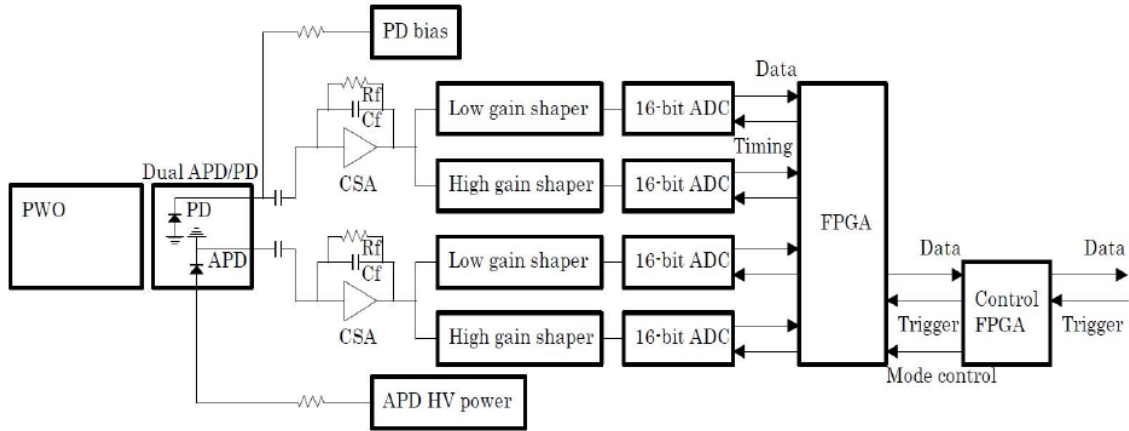


Figure 2.10: Block diagram representation of the Front-End Circuit for the TASC read-out [52].

- High Energy Shower Trigger (HET):** this is the main trigger mode for the CALET mission, as it targets high energy electrons from 10 GeV to about 20 TeV, high energy gamma-rays from 10 GeV to ~ 10 TeV, and protons and nuclei from a few 10 GeV to about 1000 TeV. It is based on the signals from the top layer of the TASC and the sum of signals from the 7th and 8th layers of SciFi belts, and requires a large energy deposit in the middle of the detector. This allows to maximize the exposure to the target events, both suppressing low energy particles and achieving a large solid angle acceptance.
- Low Energy Shower Trigger (LET):** this is the trigger used for low energy electrons from 1 GeV to about 10 GeV (to study solar activity), and GRB gamma rays of energy ≥ 1 GeV. It will be used only at high latitude, where the geomagnetic rigidity cut-off is lower than 2 GV and does not reject incoming lower energy particles. The energy deposit required in the middle of the detector is much lower than in the case of the HET (but significantly higher than for a MIP) and additional signals are required from the CHD and IMC upper layers to restrict the incident angle of the particles.
- Single Trigger (ST):** this mode allows to select minimum ionizing particles (MIPs) essential for the detector in-flight calibrations. All trigger sources are used and each threshold is set to a suitable value to detect one MIP signal.

2.4 The CALET acceptances and geometrical factors

Since the CALET telescope triggers on particles with very different incident angles, the only topological requirements for HET are to cross the 4th pair of layers of the IMC plane and the TASC top layer, an event pre-selection and classification seems mandatory for the data analysis. In particular it is required that the particle “shower path-length” inside the TASC is longer than $27 X_0$. Four acceptance categories are defined to distinguish the interesting events, as follows:

- **type 1 acceptance:** the incident particle direction crosses the top CHD layers, the top and bottom TASC layers, and is well contained within a fiducial volume in the TASC (defined by excluding in each layer the calorimeter crystals logs at the TASC edges);
- **type 2 acceptance:** the incident particle direction crosses the top CHD layers, the top and bottom TASC layers, but it is outside the TASC fiducial volume;
- **type 3 acceptance:** the incident particle direction crosses the 4th IMC pair of layers, the top and bottom TASC layers;
- **type 4 acceptance:** the incident particle direction crosses the 4th IMC pair of layers, the top layer and one lateral side of the TASC.

For a better understanding of how this classification distinguishes between the different triggered events, a schematic representation of the four acceptance is shown in figure 2.12. The preliminary $27 X_0$ path length requirements is mandatory in the acceptance type 4, because a too short path in the TASC would preclude a precise energy determination.

The geometrical factor $S\Omega$ can then be calculated [54] for each acceptance category according with equation 2.3, using the MC simulation of the telescope based

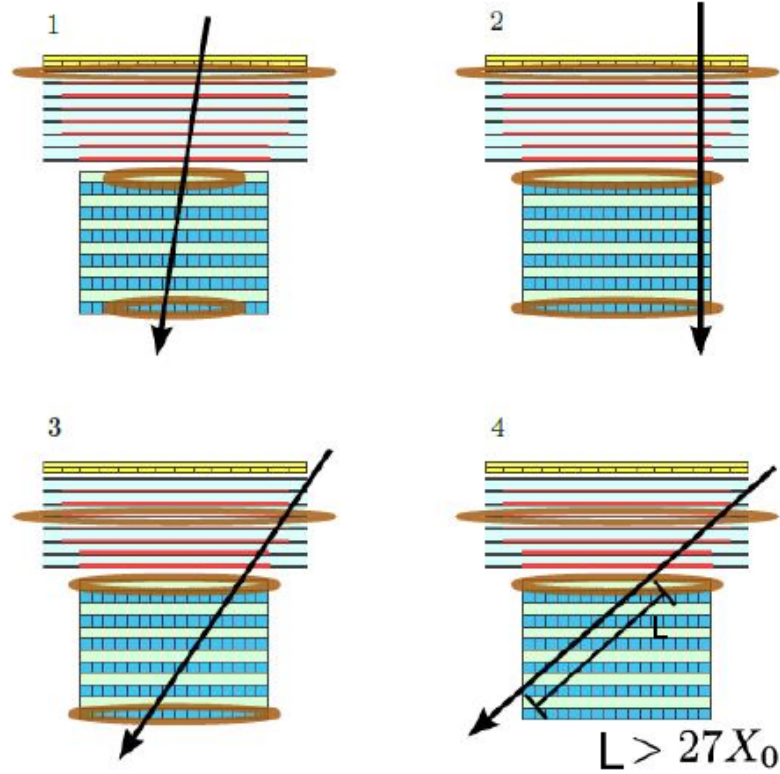


Figure 2.12: Scheme of the event classification into the four acceptance categories.

on the CAD model.

$$S\Omega = \frac{N_{sel}}{N_0} \cdot S_0\Omega_0 \quad (2.3)$$

Where N_0 is the total number of generated events, N_{sel} is the number of events inside the acceptance, and $S_0\Omega_0$ is the geometrical factor of the generation surface for the simulation, with S_0 the area of the generation surface and Ω_0 the solid angle. The obtained geometrical factors are respectively $0.042 \text{ m}^2\text{sr}$ for type 1 acceptance, $0.015 \text{ m}^2\text{sr}$ for type 2, $0.019 \text{ m}^2\text{sr}$ for type 3 and $0.035 \text{ m}^2\text{sr}$ for type 4. In this way the total geometrical factor for CALET instrument amounts to about $0.112 \text{ m}^2\text{sr}$.

2.5 Monte Carlo simulation of the CALET telescope

An accurate simulation of the detector response to the passage of charged cosmic rays is clearly an essential tool for all the analysis purpose.

In the CALET collaboration, three independent simulations of the telescope have been developed to reproduce the telescope geometry and performances. They are based on the Monte Carlo packages EPICS/COSMOS [55, 56], FLUKA [57] and Geant4 [58], and have been validated, in the accelerator energy range, against experimental data collected during various tests at CERN.

For energies not available at the beam tests, the comparison of the three different MC tools is fundamental for the reliability evaluation of all the information needed in order to correct CALET data, and thus estimate particle fluxes.

In this section, a brief description is given of the telescope simulation by means of the FLUKA package, as it is the MC tool used in this thesis work.

FLUKA is a general purpose Monte Carlo for calculations of particle transport and interaction. The code has been developed since 1988 mostly by INFN and CERN researchers, and it is widely used to simulate transport and interaction of about 60 different particles in any target material over a large energy range. This makes it useful both for fundamental research and for applications, including: the study of proton and electron accelerator shielding, target design, calorimetry, dosimetry, detector design, cosmic rays and neutrino physics, radiotherapy etc.

FLUKA handles the ionization energy loss via the Bethe model parametrized with average ionization potentials, density and shell corrections. The delta rays are produced explicitly only above a user-defined threshold, while below it a continuous energy loss with statistical fluctuations is assumed. The multiple Coulomb scattering is described according to Molière's theory, and a detailed algorithm has been developed to simulate the path curvature effects. Hadron inelastic nuclear interactions, if particle momentum is below 5 GeV/c, are simulated by the isobar model, through resonance production and decay, and by taking into account elastic charge exchange. On the other hand, if momentum is above 5 GeV/c, the interactions are described on the basis of the Dual Parton Model (DPM) [59]. Nuclear ions interactions, instead, are treated through interfaces to external event generators. In particular DPMJET-II or DPMJET-III [60] are used for energies above 5 GeV/n, and modified RQMD (Relativistic Quantum Molecular Dynamics) [61] between 0.1 and 5 GeV per nucleon.

The detector geometry can be implemented in FLUKA via the dedicated geometry package, derived from the Combinatorial Geometry (CG) from MORSE [62] where new bodies have been introduced, and a completely new fast tracking strategy has been developed, with special attention to charged particle transport.

The Monte Carlo code simulates the precise CAD model of the CALET telescope, with sensitive volumes, absorbers and structural materials. The sensitive detector subsystems are implemented as object-oriented entities, that are capable to evaluate tracking information as, for example, the energy and momentum of particles, the momentum direction and the energy depositions in the traversed material, that are then used to simulate the observed distribution of hits. In fact, the response of each detector is given by the deposited energy inside its volume. Digitization and electronic noise are not simulated in this analysis. However, the impact of both has been studied experimentally on test beam data of detector prototypes.

The MC simulation starts with the random generation of a given particle momentum and trajectory, according with the selected spatial distribution and energy spectrum. Then the cosmic ray is propagated through the detector and the energy deposits in the different sensitive volumes are extracted and saved in a conveniently formatted output file, together with the original MC information (i.e. particle trajectory, interaction point, etc.). This file is the input stage for the following reconstruction step, where suitable energy thresholds are applied to the different active volumes and the desired analyses are performed (e.g. hit clustering, tracking, acceptance calculation, etc.).

The Monte Carlo data samples used in this work are generated starting from electron, proton, helium and carbon nuclei, isotropically distributed over the full detector, in different energy ranges spanning from few 10 GeV to 100 TeV, and obeying to a power-law energy spectrum with spectral index $\alpha = -1$. The latter parameter has been chosen in order to have enough statistics in the higher energy bins at the time of generation. In the following steps of the analysis, the generated spectrum can be modulated to any other different spectral shape by re-weighting the events with no need to repeat the time-consuming step of event generation.

Chapter 3

CALET expected performances and main physics goals

This chapter contains a brief description of the expected performances of the CALET telescope and of its major scientific objectives, including the search for nearby cosmic-ray acceleration sources and possible dark matter signatures, that will be pursued with precise measurements of the electron and gamma-ray spectra. These goals are made possible by the expected excellent discrimination power of the instrument, that allows to identify electrons in a large background of hadrons and to separate gamma-rays from charged particles. Thanks to its deep calorimeter preceded by a high granularity pre-shower with imaging capabilities, CALET will be able to provide unparalleled energy resolution and broad sky coverage to probe the high-energy Universe.

3.1 Main anticipated performances of the CALET telescope

To evaluate the expected CALET performances, dedicated studies have been performed on Monte Carlo simulated data. These data are mainly generated with the COSMOS/EPICS code, but also the FLUKA package has been used, as well as Geant4. In the following, a brief excursus is made, on the most important Monte

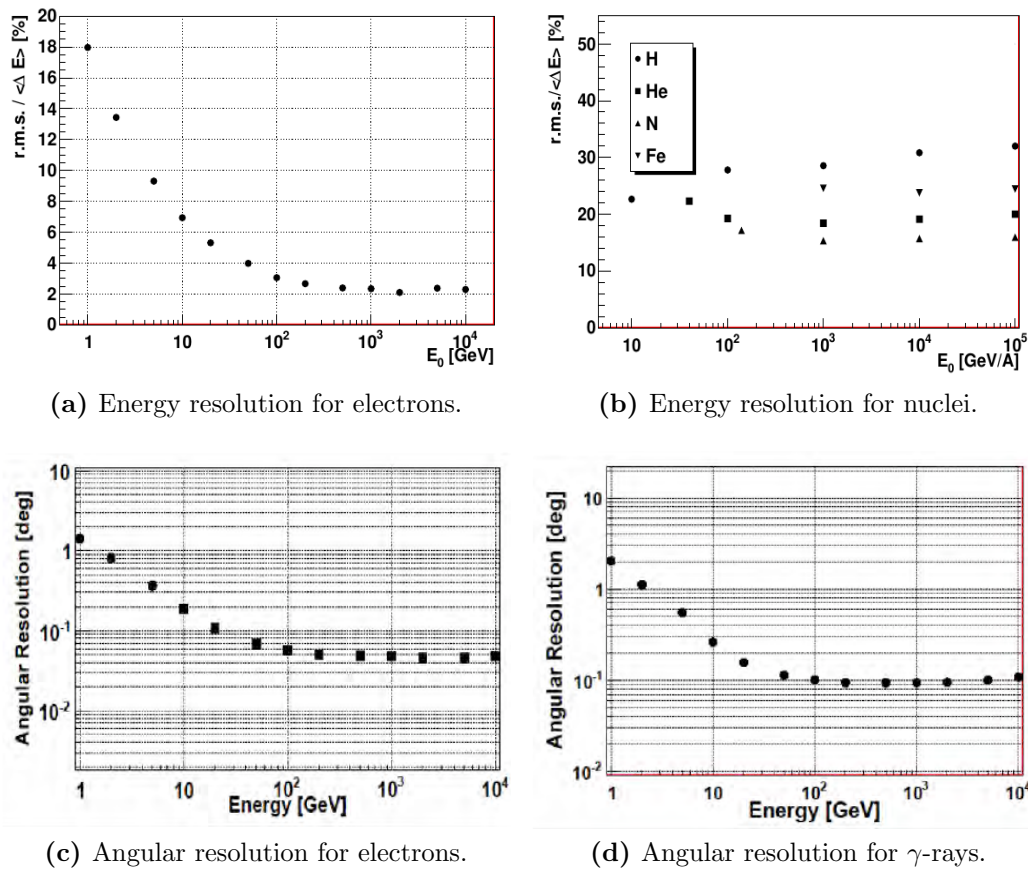


Figure 3.1: Expected CALET energy and angular resolution for electrons, γ -rays and nuclei.

Carlo expected results.

3.1.1 Energy and angular resolution

A good energy and angular resolution is of crucial importance for CALET to accomplish its physics program. The energy of the incident particle is measured using the combination of IMC and TASC detectors, by summing the energy deposited in both of them. The expected resolution is shown in figure 3.1 (a) and (b) for electrons and nuclei, respectively, as a function of the energy. Figure 3.1 (c) and (d) shows the angular resolution dependence on particle energy, as resulting from simulations with electrons and γ -rays respectively.

From the plots in the sub-panel (a) it is possible to notice that for electrons above 100 GeV the resolution assumes a constant value around 2%. This value will clearly

depend on the imperfections during the calorimeter construction, and in the accuracy of the calibrations, anyway, an energy resolution of order 2%-3% it is expected for electrons up to 10 TeV. For what concerns, instead, the energy resolution for ions (plot (b) in figure) it is assumed to be about 30% for protons, and it becomes better moving to heavier nuclei, like Helium, Nitrogen and Iron. The energy dependence is very mild for all the considered nuclear species.

On the other hand, plots (c) and (d) show that on the estimate of the particle direction (reconstruction of the shower axis), the angular resolution is less than 1 mr for electrons at 100 GeV, and about 1.7 mr ($\sim 0.1^\circ$) for γ -rays of the same energy.

3.1.2 Electron-proton discrimination

Besides a good energy resolution, an efficient identification of electrons (positrons) is another essential requirement for CALET, to perform precision measurements of the cosmic-ray electron spectrum in the energy range from ~ 1 GeV to ~ 10 TeV. In fact the background for this measurement is dominated by the flux of cosmic protons, which is 3-4 orders of magnitude higher, according to the energy, than the signal.

Since CALET does not have a magnet, topological cuts are used to separate the showers induced by electrons and γ -rays from those generated by protons. The two main cuts take into account the shower starting point and the lateral size dependence with shower depth. The first cut is based on the fact that an induced shower by an incident proton starts deeper than the one generated by an electron, and is less contained in the TASC. The second cut, instead, takes into account that the hadronic showers have an average lateral size that becomes progressively larger as the depth in the calorimeter increases, whereas the lateral width of e.m. showers is governed by the Molière radius.

Operatively, a variable is built, that provides a quantitative description of the different longitudinal shower development in the TASC between electrons and protons. This topological variable f_E is the energy ($E_{\text{layer}}^{\text{exit}}$) deposited in the “exit layer”, where the shower starts leaking off the TASC, weighted by the total TASC energy

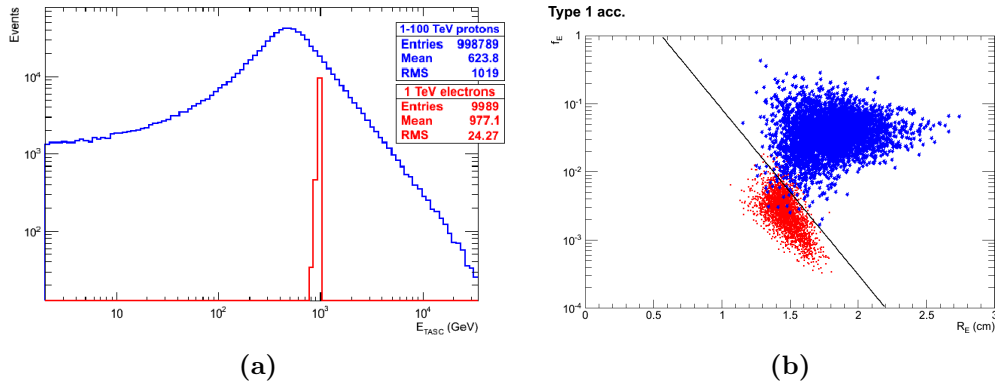


Figure 3.2: (a): total TASC energy deposit for protons (blue) and 1 TeV electrons (red) from EPICS MC; (b) Correlation plot of f_E versus R_E for electrons (red points) and protons (blue star points) [63].

deposit E_{TASC} :

$$f_E = \frac{E_{\text{layer}}^{\text{exit}}}{E_{\text{TASC}}}. \quad (3.1)$$

In this analysis [63] the exit layer has been used, instead of the bottom layer of the calorimeter, because for very inclined proton events, the exit point of the shower may be located upstream (i.e. from layer 6 to layer 11). The energy fraction f_E usually is lower for an electron than for a proton, since the former interact, on average, earlier than the latter inside the instrument, and thus the e.m. shower is more likely to be completely contained in the TASC.

The correlation of f_E with another topological variable, known as the energy weighted spread R_E , provides a powerful tool for the electron-proton separation. R_E is an estimator of the lateral width of the shower in the TASC. For electrons, it is comparable with 1 Molière radius (of the order of the crystal lateral dimension), while for protons the lateral hadronic shower development has a typical scale of about 1 interaction length. The energy weighted spread is defined by equation 3.2 as:

$$R_E = \sqrt{\frac{\sum_i (\sum_j \Delta E_{i,j} \times R_i^2)}{\sum_j \Delta E_{i,j}}}, \quad (3.2)$$

where $\Delta E_{i,j}$ is the energy deposited in the j -th PWO crystal of the i -th layer, and

the root mean square spread R_i at the i -th layer (with $0 \leq i \leq 11$) is given by:

$$R_i = \sqrt{\frac{\sum_j (\Delta E_{i,j} \times (x_{i,j} - x_{i,c})^2)}{\sum_j \Delta E_{i,j}}}. \quad (3.3)$$

where $x_{i,c}$ is the coordinate of the intercept of the shower axis with the i -th layer, and $x_{i,j}$ is the coordinate of the center of the j -th PWO crystal in the i -th layer.

The correlation of f_E and R_E is shown in figure 3.2 (b), where is easy to notice that it allows for a good separation between electron and protons. While from the plot (a), where the total TASC energy deposit is displayed both for protons and 1 TeV electrons, it follows that – thanks to the high energy resolution for electrons of the TASC ($\sim 2\%$ for 1 TeV electrons) – the proton contamination can be studied in the energy bin $912 \text{ GeV} \leq E_{\text{TASC}} \leq 1000 \text{ GeV}$. Then in order to choose the most suitable selection cut, among different ones, the rejection power $R = \varepsilon_e/\varepsilon_p$ has been studied. It is defined as the ratio of the electron reconstruction efficiency (ε_e) with respect to the proton background contamination (ε_p). Finally, a linear cut in log-log scale is chosen to maximize the electron selection efficiency, while minimizing the proton contamination.

To discard the proton events surviving the f_E versus R_E cut, two additional selection cuts are applied. The first one is based on the ratio between the energy deposited in the last IMC layer within 1 Molière radius from the shower axis, and the total energy deposited in the IMC. The second one uses the total energy E_{CHD} deposited in the CHD paddles.

After this additional selection, the final number of protons surviving all the criteria is 7 out of the initial $\sim 10^6$ events generated. These events include an irreducible hadronic background due to protons that produce at least one high-energy neutral pion in the upper part of the detector. Neutral pions may induce “electron-like” showers in the TASC that are indistinguishable from electron-induced showers.

The result of this analysis, performed for different energy bins, is shown in figure 3.3, where the electron efficiency (top) and the proton contamination (bottom), as evaluated from three different Monte Carlo simulations, have been compared.

It is possible to observe that the electron efficiency remains over the 75% level, while

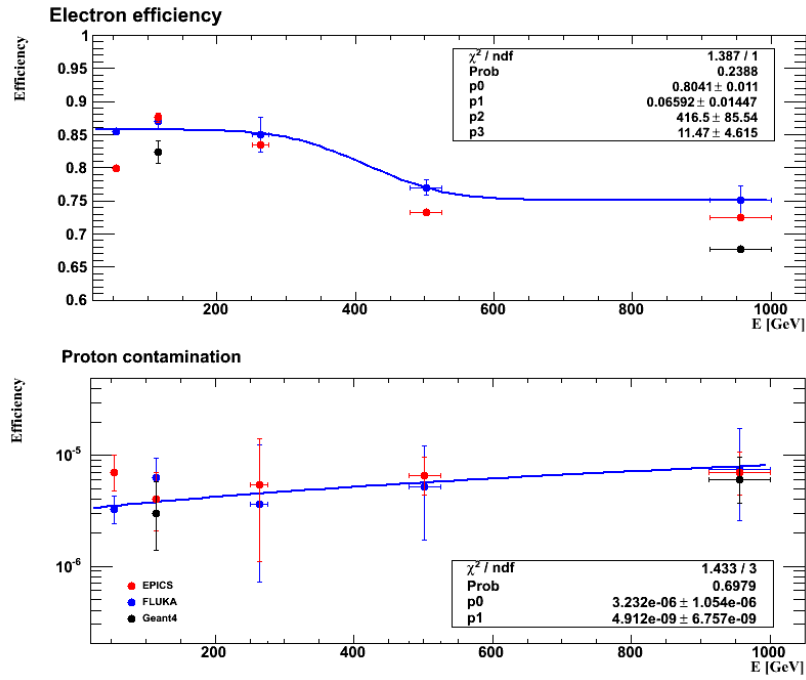


Figure 3.3: The electron efficiency dependence on energy is shown (top) together with the proton contamination (bottom) [63].

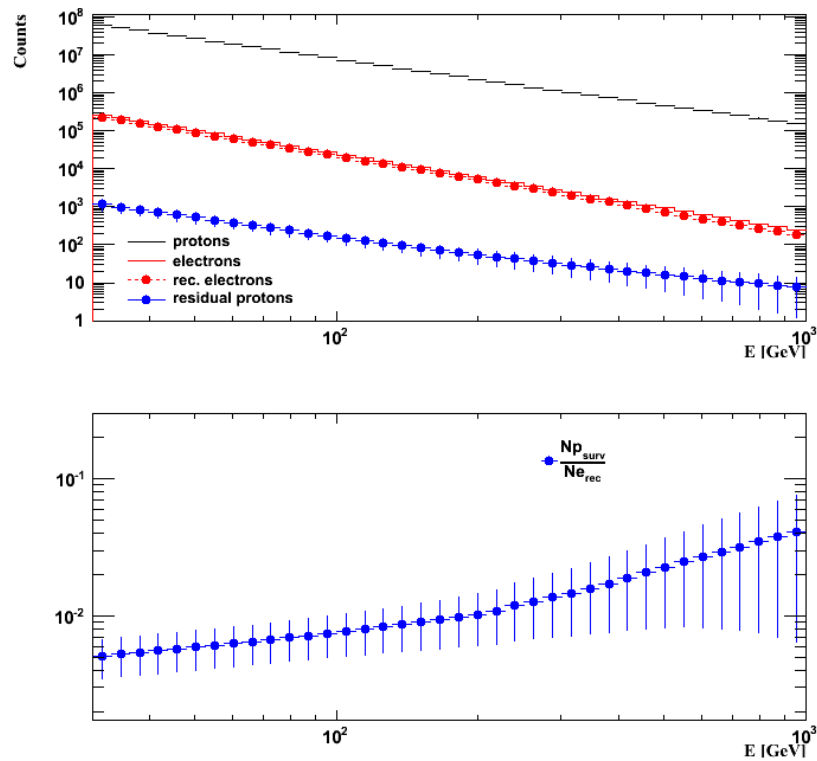


Figure 3.4: Expected number of proton and electrons in 5 years of data taking for the CALET experiment (top), together with the resulting contamination (bottom) [63].

the proton contamination is lower than 10^{-5} for the considered bins.

Finally, the top plot of figure 3.4 shows an estimate of the number of electrons (red filled circles) reconstructed by CALET in five years of data taking, compared with the expected electron signal (red line). The estimated proton signal (black line) and the expected residual background (blue filled circles), after applying the described selection cuts, are shown as well. In the bottom side plot the residual proton background is defined as the ratio between hadronic background and reconstructed electron counts, it is shown as a function of energy. For an energy $E \simeq 1$ TeV the background-to-signal ratio was found to be close to 4% with an upper limit of $\sim 7.5\%$, obtained by propagating the uncertainty on the proton contamination.

3.2 The CALET physics program

The main CALET scientific objective is a precise measurement of the inclusive electrons and positrons spectrum in the energy range from few GeV to about 20 TeV, in order to unveil the presence of possible nearby sources of cosmic rays situated in our Galaxy (within approximately 1 kpc from the solar system).

An hint that the electron energy spectrum above 1 TeV may reveal the presence of nearby sources is given by recent data collected by H.E.S.S. [64], where a signature of a cut-off in this region seems to emerge from the data. For this reason, a direct measurement, performed in space, of the electronic spectrum above 1 TeV is of particular interest. In fact, direct measurements are not affected, as it is the case of indirect ground measurements, by significant systematic errors due to the uncertainty on the primary electron identification with respect to the diffuse gamma-ray and hadronic background, and could give the first evidence of a signature from nearby astrophysical sources, casting light on the origin and propagation of CRs. Moreover, CALET will also be able to perform accurate anisotropy measurements thanks to an expected observation time of 5 years and high duty cycle.

High resolution measurements of the inclusive electronic spectrum may also contribute to provide new experimental input to the open questions on Dark Matter observation. In fact, according to model predictions DM particles (Kaluza-Klein

particles from extra-dimension theories or neutralinos by super-symmetric theories) may have masses in the hundreds of GeV to TeV range. CALET has the capability to search for a possible signature of the annihilation/decay of such particles, in both the electron and γ -ray spectra by exploring the trans-TeV energy range.

Another major physics objective is to extend and improve the presently available direct measurements of the charged cosmic rays spectra. In particular, CALET is expected to extend the present measurements of the ratio of fluxes of secondary to primary elements (e.g. boron/carbon and *sub*-Fe/Fe) by an order of magnitude in energy, providing important information about the energy dependence of cosmic-ray propagation in the galaxy.

Furthermore, as the recent measurement from AMS-02 [65] seems to confirm the presence of a spectral break in the proton and helium fluxes in the 200–300 GeV region (as already reported by PAMELA and CREAM), CALET will be able to perform an accurate scan in this energy range, and measure the curvature of the spectrum and the position of the spectral break point, extending the present measurement to the multi-TeV region. This kind of measurement is the main subject of chapter 6 and one of the main topics of this thesis work.

CALET will be also measure Ultra Heavy nuclei in CRs, up to $Z = 40$, monitor gamma ray transients with a dedicated Gamma-ray Burst Monitor (CGBM) and study solar modulation.

In the following, a brief description of the expected scientific goals from CALET is presented.

3.2.1 Search for electron nearby sources

Electrons, due to their low mass and leptonic nature, are an ideal probe to clarify the origins of cosmic rays and their propagation mechanism inside the Galaxy.

In fact, high-energy electrons lose energy mainly via synchrotron and inverse Compton processes during their propagation in the ISM. This, in addition with the absence of hadronic interactions, simplify models of electron propagation with respect to other cosmic ray components.

Evidence of non-thermal X-ray emission and TeV γ -rays from supernova remnants

suggest that high energy cosmic ray electrons (and/or protons) are presumably accelerated in SNRs. Moreover, since the energy loss rate is almost proportional to the square of the energy, TeV electrons lose most of their energy on a time scale of about 10^5 yr and their propagation distances are therefore limited to ~ 1 kpc. Thus, only a few cosmic ray sources can contribute to the observed flux, and fluctuations are expected in the local electron energy spectrum [66].

It is then possible to take advantage of the known information on the ages and distances of the observed SNRs (in the neighbourhood of the Solar System), to determine theoretically which sources could contribute to electrons most efficiently in a given energy range, and thus correlate individual sources with observable spectral features in the electron flux.

In the case of one of the calculations by Kobayashi et al. [67], that uses a diffusion coefficient of $D_0 = 2 \times 10^{29} \text{ cm}^2/\text{s}$ at 1 TeV, a cut-off energy of $E_c = 20$ TeV for the electron source spectrum, and a burst-like release at $\tau = 5 \times 10^3$ yr after the supernova explosion. It is suggested that nearby SNRs such as Vela, Cygnus Loop, or Monogem, could leave unique signatures, in the form of identifiable structures in the energy spectrum of TeV electrons, and measurable footprints in the dipolar asymmetry. The expected electronic spectrum is represented in figure 3.5 by the blue dotted line.

In the same figure, the anticipated CALET measurements [68] are shown by the red points. The energy spectrum expected to be observed by CALET is simulated for 5 years of data taking, following the already mentioned model. A comparison between different electron spectrum measurements [69–73] is shown as well.

From inspection of the figure, it results evident that CALET has an unique capability to identify signatures in the energy spectrum, with high statistical precision, in particular the prominent that is expected from Vela. This might give the first experimental evidence for the presence of a nearby source of electron acceleration at very high energies: one of the main goals of CALET.

Another consequence of the much higher rate of energy loss of electrons with respect to nuclei (due to radiation), it is that the degree of anisotropy of high-energy cosmic electrons is expected to be higher than that of the nuclear component [67]. Therefore

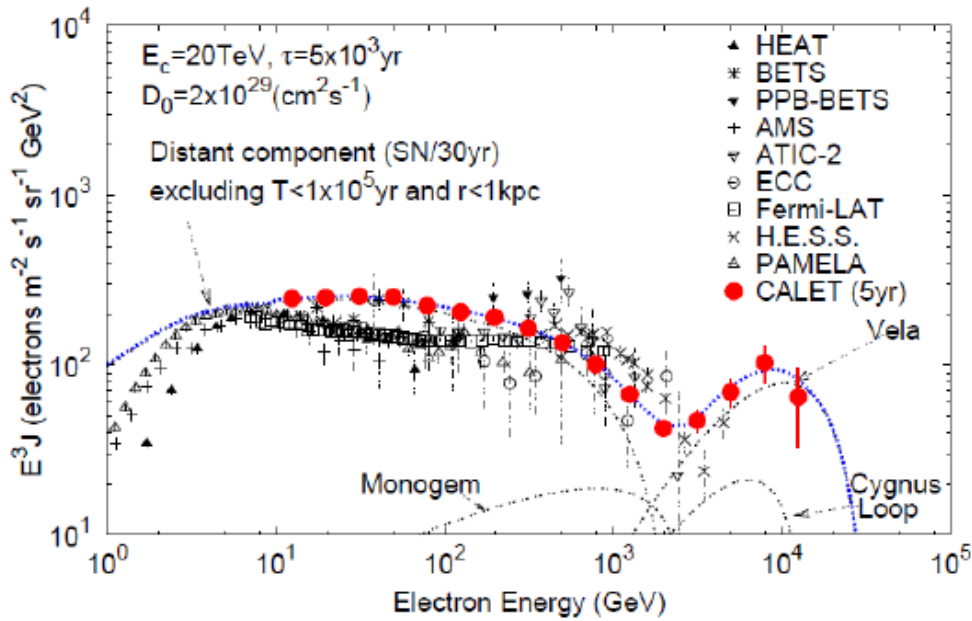


Figure 3.5: Electron (and positron) spectra predicted for 5 years of data taking with CALET (red data points) [68], superimposed to a theoretical model [67] (blue dotted line) and compared to previous measurements.

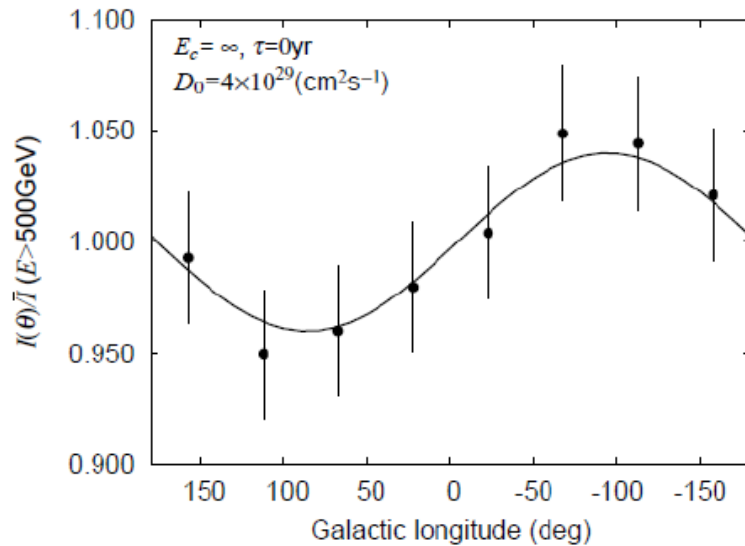


Figure 3.6: The expected results for Vela anisotropy measurement in the TeV region, and for a 5 year observation period with CALET [68].

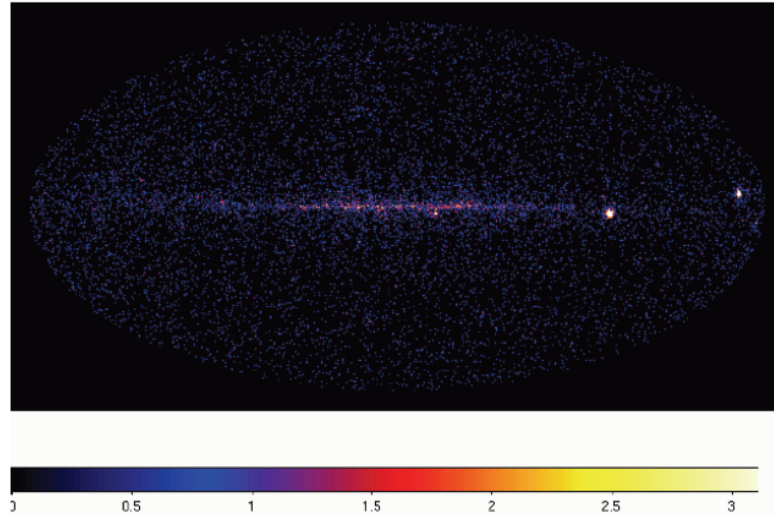


Figure 3.7: Simulated sky map of gamma rays above 10 GeV with CALET for 3 years of data taking [68].

CALET is expected to have the capability to observe a possible anisotropy in the direction of a nearby SNR. As it is shown in figure 3.6, where the electron intensity distribution is plotted as a function of the galactic longitude, in the case of a diffusion coefficient $D_0 = 4 \times 10^{29} \text{cm}^2/\text{s}$ at 1 TeV and a cut-off energy $E_c = \infty$, for the prompt release after the explosion ($\tau = 0$) [68]. The maximum intensity is in the direction of Vela.

3.2.2 All-sky gamma ray survey

Thanks to the ISS orbit, with 51.6° inclination, changing longitudes of ascending node at the rate of -5.0° per day by the precession, CALET can survey most of the sky in a wide field of view of 2 sr almost uniformly, without attitude control of the instrument.

The line of sight of the CALET detector is in the opposite direction with respect to the Earth. This provides an unique opportunity to observe gamma-ray sources with an exposure of several 10 days per year for point source. The survey of the variable γ -ray sky with CALET will allow to study the universe up to highest gamma-ray energies and with a better energy resolution than Fermi-LAT above 10 GeV [74]. In figure 3.7 it is shown a simulation of the simplified sky map for gamma rays above 10 GeV with CALET for 3 years observations [68].

Even if the observation of sources will not be a primary objective of the mission, CALET can perform complementary observations of γ -ray point sources with Fermi and ground-based telescopes. Figure 3.8 shows the expected point source sensitivity of CALET in comparison with a number of present and future experiments. For air Cherenkov telescopes observations at ground level, the sensitivities are calculated for a 50 hour exposure on a single source. For CALET, EGRET, GLAST, and MILAGRO, the sensitivities are shown for 1 year of all-sky survey. For individual point sources, Cherenkov telescopes exhibit an excellent sensitivity over 100 GeV. However, ground based telescopes have limitations, i.e. a low duty cycles (10 %), a small field of view (< 5 deg), and low rejection of background electrons.

CALET has a better sensitivity for observations of diffuse gamma-rays such as the Galactic and extra-galactic diffuse emission. The expected sensitivities for 3 years are 1×10^{-10} ($\text{cm}^{-2}\text{s}^{-1}\text{sr}^{-1}$) for the Galactic diffuse emission of the inner Galaxy region ($300^\circ < l < 60^\circ$, $|b| < 10$) that enables CALET to observe up to a few TeV, and 1×10^{11} ($\text{cm}^{-2}\text{s}^{-1}\text{sr}^{-1}$) for the extra-galactic diffuse emission allowing observations up to 10 TeV.

Moreover, if one or more sources have a major outburst, CALET can measure its variability and energy spectrum as a function of time. CALET will also complement Fermi measurements of the high energy cut-off of AGN spectra, as a function of redshift, due to attenuation by the diffuse extragalactic background (EBL).

Due to the wide field of view, CALET has also an excellent capability to detect Gamma-Ray Bursts. GRBs with a flux above 10.5 erg/cm^2 are detectable by CALET at an expected rate of ~ 10 events a year. The expected number of photon events in one burst is about 300 photons above 100 MeV and ~ 30 photons above 1 GeV [76]. CALET will extend the GRB studies being performed by other experiments (e.g. Swift and Fermi) and will provide added exposure when other detectors are not available or are pointing to other directions.

3.2.3 Search for Dark Matter candidates

A number of astrophysical and cosmological observations lead to a strong evidence for the existence of a non-baryonic, non visible matter, the Dark Matter (DM). The

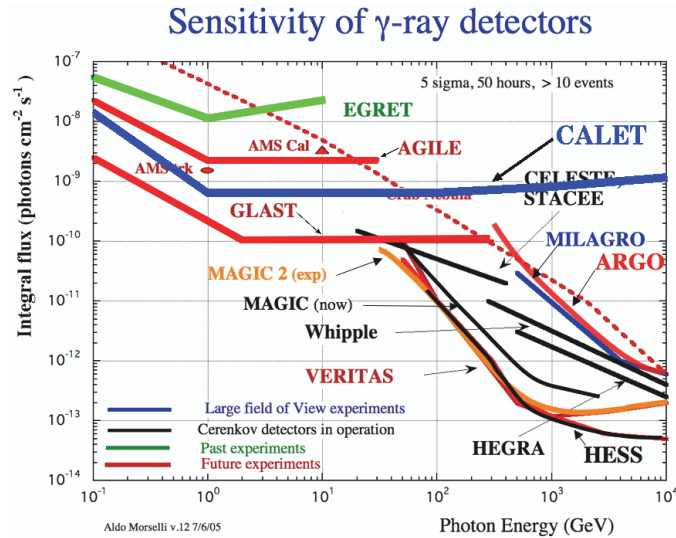


Figure 3.8: Gamma-ray point source sensitivity of CALET with respect to other experiments [75].

first one dates back to 1933 when Zwicky observed the large velocity dispersion of the members of the Coma galaxy cluster [77].

At the galactic scale, the most convincing and direct evidence of dark matter comes from the observations of the rotation curves of the galaxies, indicating that the stars rotation is too fast to be bound by Newtonian gravity, if all matter is visible.

From the Big Bang model, the measurements of light nuclei produced in primordial nucleosynthesis, and the study of the cosmic microwave background (CMB) radiation, it is estimated that the density of ordinary baryonic matter cannot be more than 4% in a flat Universe. Also, 73% of what exists in the cosmos is supposed to be made up of an invisible and homogeneous substance called “dark energy”, and the remaining 23% would be accounted for by dark matter. The latter is supposed to be constituted by particles whose nature is still unknown. They do not aggregate in celestial bodies and emit no electromagnetic radiation, therefore being not directly visible.

The existence of dark matter does not find an explanation in the framework of the Standard Model (SM) of particle physics. For this reason a wide variety of SM extensions have been hypothesized, leading to a proliferation of DM candidates.

The favourite ones are electrically neutral Weakly Interacting Massive Particles (WIMPs), with a mass in the range between tents of GeV to TeV [78–80]. Their

presence is predicted in several classes of extension of the SM, and would naturally appear as one of the thermal relics from the early Universe. An example could be the neutralino, the lightest stable particle hypothesized in R-parity conserving super-symmetric models, which annihilate and produce gamma-rays and positrons as a signature.

An alternative candidate, suggested in theories with universal extra dimensions, is the lightest Kaluza-Klein particle (LKP), which might be a stable dark matter candidate [81].

CALET will conduct a sensitive search for signatures of these DM candidates, in both the electron and γ -ray spectra. The predicted signatures are dependent on models with many parameters, and even a non-observation by CALET can put a constraint on these parameters or eliminate some models.

Both neutralinos and KK particles can annihilate and produce an excess of positrons and electrons observable at Earth. However, direct annihilation into e , μ and τ is chirality suppressed for neutralinos and not for KK particles, this results into an enhanced electron signal for LKP with respect to that from neutralinos. Moreover, since this is a direct annihilation, it results in the appearance of mono-energetic electrons and positrons which would create a specific and well detectable spectral feature. That is a sharp edge in the cosmic e^+e^- spectrum at an energy equal to the particle mass, (typically several 100 GeV to 1 TeV).

This is shown in figure 3.9, where it is plotted the simulated inclusive energy spectrum of electrons and positrons, in case of Kaluza-Klein dark matter annihilation with a 620 GeV mass and a boost factor of 40, for 2 years observations with CALET [68]. The simulated spectrum is superimposed on the galactic background spectrum (dashed line), and it is possible to notice that, even if the CALET telescope cannot separate electrons from positrons, it has the potential to detect the distinctive features from DM annihilation in the inclusive energy spectrum.

In some alternative and well-motivated scenarios of dark matter annihilation, the DM particles are supposed to be unstable and with a decay lifetime much longer than the age of the Universe.

These alternative scenarios in some cases could provide an explanation for the

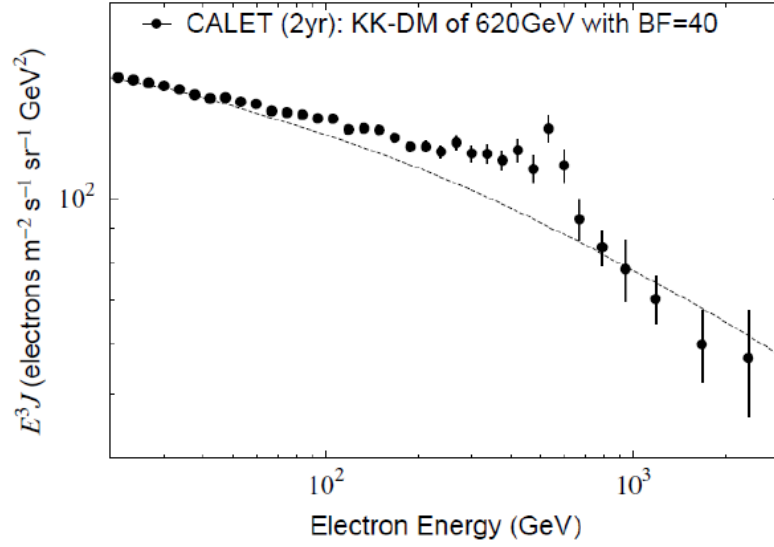


Figure 3.9: Expected electron-positron inclusive energy spectrum from Kaluza-Klein dark matter annihilation, simulated with a mass of 620 GeV and a boost factor of 40, for 2 years of data taking with CALET [68].

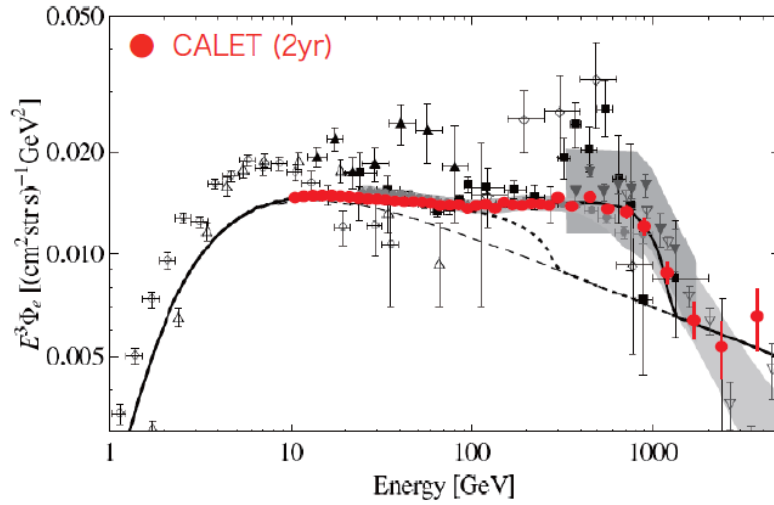


Figure 3.10: Simulation of the inclusive e^+e^- energy spectrum [68] as results from a dark matter decay $DM \rightarrow l^+l^-\nu$ for a DM mass of 2.5 TeV, and a decay time of 2.1×10^{26} s [82]. A period of 2 years observations is supposed and the simulated spectrum is superimposed on the galactic background (dashed line).

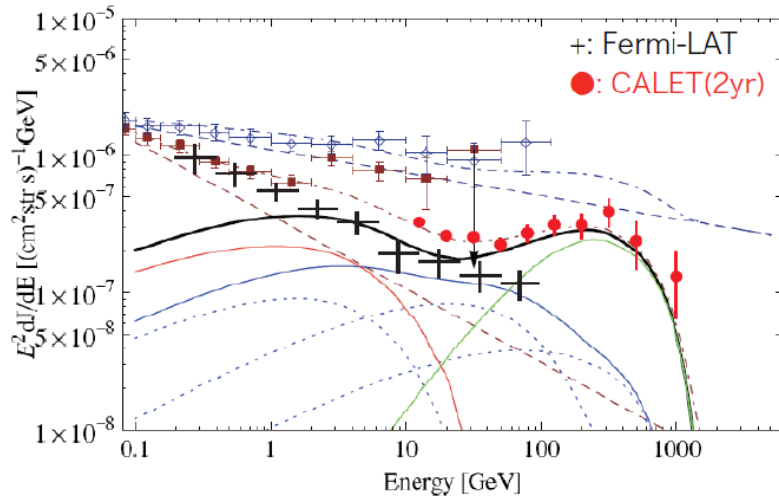


Figure 3.11: The simulated energy spectrum of the extragalactic diffuse γ -rays from decaying DM, for 2 years observations with CALET [68], including inverse Compton scattering γ -ray spectra and an isotropic extragalactic background. The DM decay scenario is the same described in figure 3.10.

anomalies observed in the positron fraction and in the total electron and positron flux by the PAMELA and the Fermi-LAT collaborations, respectively [82], being at the same time consistent with present measurements of the antiproton flux and the diffuse extragalactic γ -ray flux. In particular the observed excesses in electron and positron spectra can be explained if leptons are produced from decaying DM particles with a lifetime around 10^{26} s [82].

Figure 3.10 illustrates this scenario, showing the expected electron and positron inclusive energy spectrum for 2 years of simulated data taking with CALET, in case of a dark matter decay $DM \rightarrow l^+ l^- \nu$ with a DM mass of 2.5 TeV, and a decay time of 2.1×10^{26} s [68].

In this scenario the decaying DM could be observed also in the energy spectrum of the extragalactic diffuse gamma rays, due to the inverse Compton scattering of e^+ and e^- from dark matter with interstellar and intergalactic photons. In figure 3.11 [68] it is shown the expected extragalactic γ -ray spectrum from decaying dark matter [82], for a period of 2 years of observation with CALET. The inverse Compton scattering gamma-rays (lower energy components) and an isotropic extragalactic background (a power-law spectrum) are included as well. The DM decay channel and parameters are the same already mentioned for the electron-positron spectrum

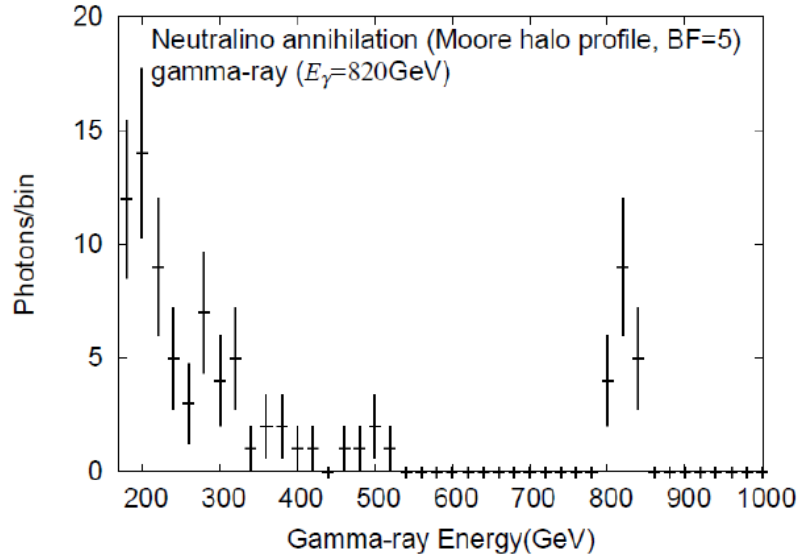


Figure 3.12: Expected energy spectrum of a γ -ray line at 820 GeV from neutralino annihilation, for 2 years observations with CALET, including the galactic diffuse background, and assuming a Moore halo profile with a boost factor of 5 [68].

of figure 3.10.

On the other hand, in case neutralinos would be the dark matter particles, they could be seen as a spectral line in the high energy gamma-ray spectrum. For a supposed neutralinos mass below several hundreds GeV also FERMI-LAT could perform this observation, with a better significance in terms of detected photons. Nevertheless, the superior energy resolution of CALET (above 10 GeV) will enable a better line-shape analysis of the detected feature. Finally, CALET will provide the best possibility of detection, for dark matter candidates with masses above several hundred GeV [83].

An example of the simulated γ -ray energy spectrum, for a supposed 820 GeV monochromatic γ from neutralino annihilation, assuming a Moore halo profile with a boost factor of 5, it is shown in figure 3.12, as expected for a period of 2 years of data taking with CALET.

3.2.4 Study of the nuclear component of cosmic rays

In addition to electron and γ -ray measurements, the CALET instrument has been designed also to identify CR nuclei with individual element resolution, and to mea-

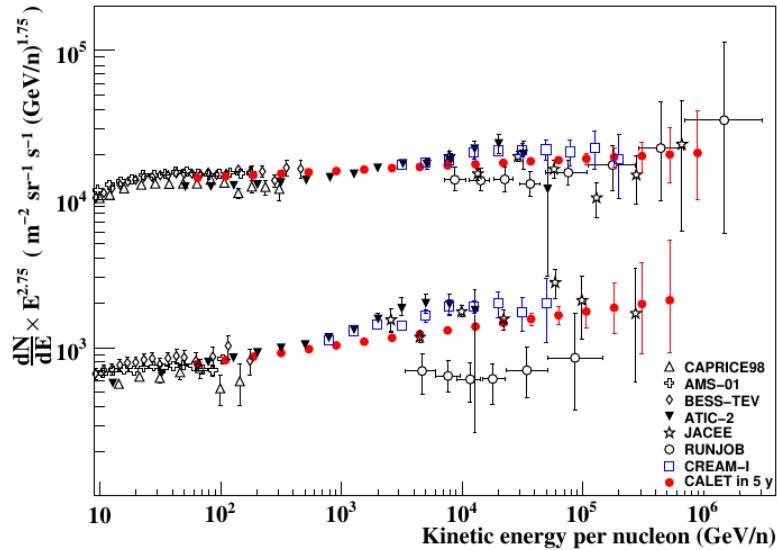


Figure 3.13: The anticipated H and He flux in 5 years of data taking with the CALET telescope, in comparison with a partial compilation of recent experimental results [84].

sure their energies in the range from a few tens of GeV to the PeV scale. This will allow to extend to higher energies the range of direct measurements of cosmic ray composition and secondary-over-primary ratios, and to verify the findings of present experiments on balloons (e.g.: ATIC, CREAM, TRACER) and in space (e.g.: AMS, PAMELA).

In 5 years of data taking on the ISS, CALET is expected to measure the proton energy spectrum up to about 900 TeV, and the helium spectrum up to ~ 400 TeV/n, as shown in figure 3.13, where the anticipated proton and helium energy spectra for CALET are shown in comparison with recent experimental results.

The extension of direct measurement of CR nuclei spectra to unprecedented energies is of fundamental importance in order to investigate the presence of possible charge dependent spectral cut-offs at high energies, that are hypothesized to explain the CR “knee” [30], while a spectral hardening can be related to non linear acceleration mechanisms [85].

The CALET telescope, with its charge resolution, will allow to measure with sufficient statistical precision the energy spectra of the most abundant heavy primary nuclei: C, O, Ne, Mg, Si and Fe, up to about 20 TeV/n, as it is illustrated in figure 3.14. This will allow to investigate potential spectral features, like a hardening

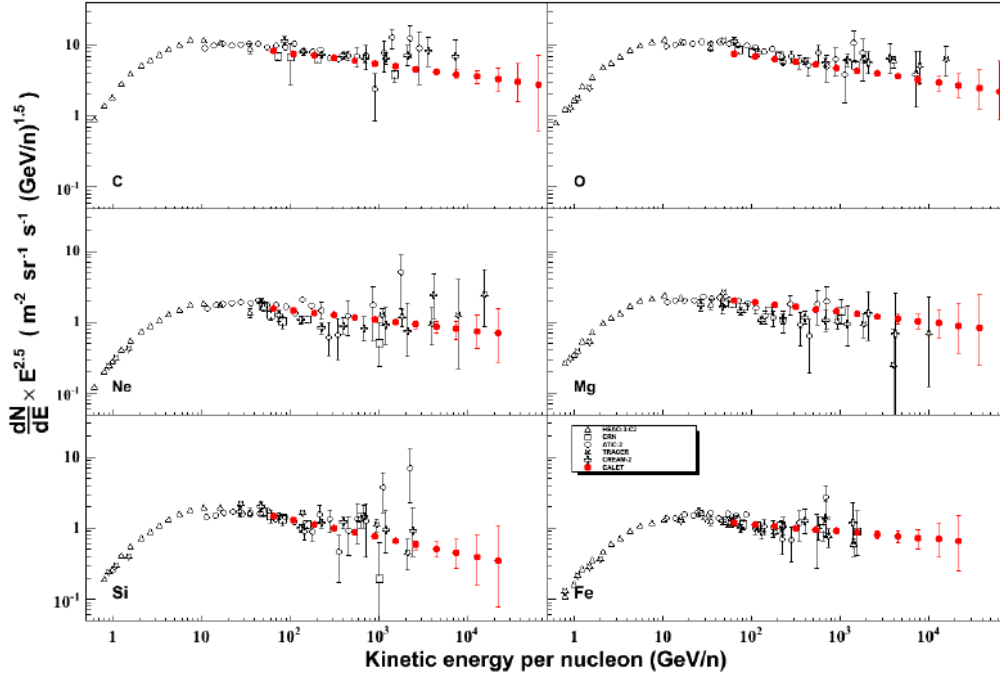


Figure 3.14: The expected measurement of the energy spectra of the most abundant heavy primary nuclei with CALET in 5 years of data taking, compared with a partial compilation of previous experiments [84].

above 200 GeV/n or a deviation from a single power-law, indicating the presence of a curvature in the spectrum.

Furthermore, a direct measurement of the secondary-to-primary flux ratios can provide additional information on the CR propagation mechanisms, as explained in section 1.4. In particular, cosmic rays of primary origin such as carbon and oxygen interact with the interstellar medium to produce secondary fragments, such as lithium, beryllium and boron. The direct measurement of the flux ratios of secondary-to-primary elements and their energy dependence can allow to discriminate among different propagation models, and provide important constraints on the composition and homogeneity of the interstellar medium itself.

The B over C ratio (B/C) is one of the most sensitive quantity to test models, as B is purely secondary and its main progenitors C and O are primaries. The energy dependence of this ratio is seriously modified by changes in the propagation coefficients, and being the ratio of two nuclei with similar charge, it is less sensitive to systematic errors and to solar modulation than single fluxes or other ratios of nuclei

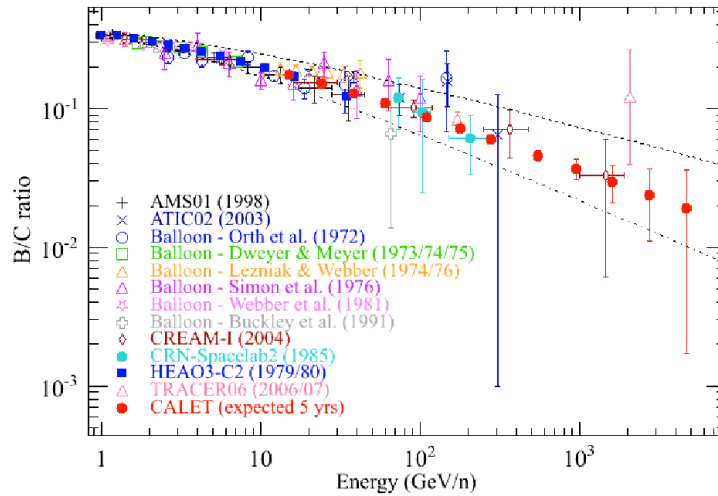


Figure 3.15: The expected measurement of B/C after 5 years of data taking with CALET, in comparison with some results from previous experiments [86].

with more distant charge values.

Balloon experiments have an effective limit on the highest energy points of the B/C measurements due to the residual systematic uncertainty on the subtraction of the irreducible background originated by the atmospheric overburden at flight altitude. On the contrary, space experiments like CALET are free from this limitation, and can extend the measurement above 1 TeV/n, providing fundamental information to discriminate among different propagation models, and to infer the slope of acceleration spectra at the source.

It is expected that CALET can improve the accuracy of the present measurements of the B/C above 100 GeV/n, and extend them beyond 1 TeV/n. In figure 3.15 a compilation of B/C data from direct measurements is shown, together with the anticipated data points from CALET in 5 years, that are represented by the red filled circles, and span over a wide energy range from 15 GeV/n to about 8 TeV/n.

3.2.5 The detection of ultra-heavy nuclei

CALET can also make significant measurements of the relative abundances of the Ultra-Heavy (UH, $Z \geq 30$) nuclear component of the cosmic radiation, whose composition is important to study the source and acceleration mechanism of the Galactic Cosmic Rays (GCR).

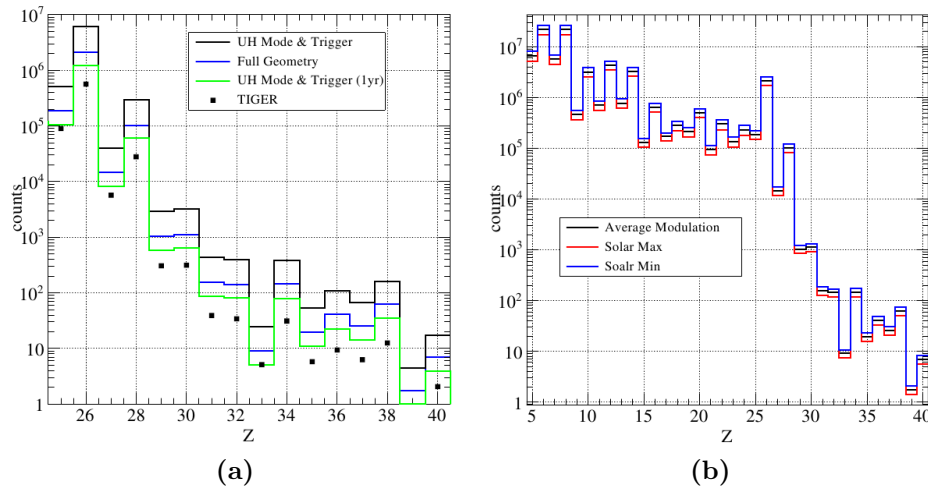


Figure 3.16: Expected number of Heavy and Ultra-Heavy cosmic rays observed by CALET in 5 years of data taking [87]. Different trigger type and comparison with the TIGER data are shown in (a), while in (b) the results for the “full geometry” mode, for different solar modulation hypotheses, are illustrated.

The CALET charge detector has the required charge resolution [47] and dynamic range to measure GCR nuclei up to charge $Z \sim 40$. However, for the more abundant nuclei with $Z \leq 28$, CALET will be able to measure the energy spectra, taking advantage of the track and energy reconstruction from the IMC and TASC. For rarer ultra-heavy nuclei ($30 \leq Z \leq 40$) the statistics collected requiring the passage through the “full geometry” of the detector will be limited. For this reason, UH measurements will be made with the looser requirement of their passage through the CHD and the top 4 IMC layers as above ~ 600 MeV/n the incident particle’s charge can be determined without an energy correction [87] (that would otherwise require the presence of the TASC). An energy threshold can be provided taking advantage of the Earth’s magnetic field. This results into a large increase of the geometric acceptance factor from ~ 0.07 m²sr to about 0.44 m²sr in the “UH mode”. In figure 3.16 are illustrated the predicted number of nuclei that CALET is expected to measure in 5 years of data taking [87]. Plot (a) in figure shows the anticipated number of ultra-heavy GCRs detected in the UH measurement mode (black line) and in the full geometry (blue line), in comparison with the TIGER experimental measurements at balloon altitudes (black marker) [88]. The expected collected events for 1 year of data taking in the UH mode are shown (green line) as well. Plot

(b) shows the expected number of events for heavy and ultra-heavy nuclei ($5 \leq Z \leq 40$), in the full geometry (standard acceptance modes) for intermediate (black), maximum (red) and minimum (blue) solar modulation cases.

In conclusion, it is expected that the CALET telescope will record ~ 10 times the UH statistics of TIGER, in the ultra-heavy mode, and about 4 times in the full geometry mode. It will complement the higher statistics of the balloon-borne Super-TIGER measurements in the $5 \leq Z \leq 40$ range without being affected by the systematic effects introduced by the corrections needed to take into account the CRs propagation in the residual atmosphere at balloon altitude.

Chapter 4

Tracking with the IMC detector

The fine granularity of the IMC can be exploited not only to image the early development of showers but also to reconstruct the trajectory of an incident particle until it undergoes an interaction. The implementation and validation of a suitable algorithm to exploit its tracking capabilities – one of the main topics of this thesis work – are described in this chapter.

Track identification and reconstruction is of the utmost importance for CALET, not only to detect the incidence direction of the incoming particle, but also to improve the data analysis in a number of cases. As an example, charge identification requires a backward extrapolation of the track to the CHD planes (see section 2.2.1) to determine which paddles have been hit. Also, the readout of individual fibers in the IMC provides imaging capabilities that are used by the standard proton rejection algorithm [63], which relies on topological calorimetric variables as, for instance, the lateral width of the shower with respect to the particle trajectory. Furthermore, the measurement of multiple $\frac{dE}{dx}$ samples in the IMC fibres improves the overall charge reconstruction (see chapter 5) providing an adequate identification of the primary particle.

Track (and vertex) reconstruction is traditionally an important step in the analysis of high-energy experiments data. It can become quite challenging in the presence of a large number of secondary particles traversing the detector and generating many “hits” in position-sensitive detectors. One example is the case of hadronic interactions taking place inside the CALET calorimeters. These hits have to be

first grouped into track candidates and subsequently fitted with a track model to find track parameters. After extensive testing, a suitable choice for particle tracking inside the IMC was established with the implementation of a Kalman filter [89] algorithm.

4.1 The combinatorial Kalman filter

The linear Kalman filter is a hybrid technique for simultaneous track finding and fitting. In its combinatorial formulation [90] it provides robust track identification which can deal with spurious hits and “holes” along the track due to inefficiencies. The general concepts behind the Kalman filter technique can be briefly summarized as follows, with a simple example.

Let’s focus on a discrete linear system, whose evolution is described by an N -dimensional state vector x_k at point k , where k is a generic discrete time variable which serves as an independent variable of the evolution equation. For example, it is possible to describe in this way a particle moving along a linear trajectory in a two-dimensional space and traversing detector planes at various positions. In this case k is the index of the detector layer, and x_k is a two dimensional vector consisting of the impact angle on the k -th detector layer and the coordinate of the impact point. In this scheme it is possible to obtain the predicted state at point $k + 1$ by multiplying x_k with the evolution matrix F_k from point k to point $k + 1$, plus an eventual random contribution w_k (due for example to multiple scattering). The predicted state at $k + 1$ involves only information (i.e. measurements) at point k , then the measurement at point $k + 1$ can be combined with the predicted state to produce a “filtered” estimate of the status vector and of the covariance matrix at $k + 1$. The residual of the filtered estimate of the measurement with respect to the true one can then be computed and the χ^2 value of the “fitted” track can be updated. This procedure is then iterated to point $k + 2$ and so on. It is worth to note that, at each step of the procedure, the status vector is estimated using only the information propagated up to that point, so the estimates for first points are quite inaccurate. For this reason, after the last point has been reached, a procedure

known as “smoothing” can be applied, in order to back-propagate the information provided by the full measurements set to all the previous points. In our example, the smoothed state of the first point will give the best estimate of the impact angle and position on the first detector layer for the incoming particle.

The core of the track finding algorithm is the use of the predicted state vector and of the covariance matrix at point $k + 1$ to identify the measured coordinate to be assigned to the track at that point, via a suitable criterion. A possibility is to associate the measurement nearest to the predicted one, but this simple choice doesn’t provide a robust algorithm, immune to wrong initial assumptions. In fact, if there is a high track multiplicity or if the initial estimate is miscalculated, then a wrong measurement might be associated to the predicted state, as for example a noise cluster or an ill-measured coordinate belonging to another track. To deal with this problem it is possible to formulate the Kalman filter in its combinatorial form. This means that a new track candidate is created for each measurement at $k + 1$ point which lies sufficiently near to the predicted one. In this way the predicted original track is “branched” into many candidates, and each of them can be evolved separately. Then the real physical track(s) can be selected at the end, with a dedicated criterion, based on the track parameters and topological constraints (e.g.: geometry, acceptance, etc.). To account for possible detector inefficiencies, a new branch with a missing hit on $k + 1$ can always be created: the predicted status vector thus coincides with the filtered one (since there is no information to be used to improve the prediction).

The combinatorial filter is robust since it finds and evolves separately all the “reasonable” track candidates, and only at the end, when all the information is available, it discards the spurious ones. Obviously, this can produce a very large number of track candidates which can considerably slow down the computation. To solve, at least partially, this issue within a reasonable computing time, there are substantially two options. The first one is the implementation of additional criteria for “in-line candidate suppression”. This permit to reduce the number of the tracks to be propagated and thus the computation time. For example, a candidate track may be discarded if, at any point of its evolution, it has a χ^2 greater than a predefined value or if the

number of its missing points (consecutive or not) exceeds a predefined threshold. The second possibility is not strictly related to the algorithm implementation but can be quite effective. It consists in restricting the domain in which the algorithm performs its track finding, using some external criteria, as in the case when it is known a priori that a given physical region of the detector is not usable for tracking. In the case of the IMC detector of CALET, a combinatorial implementation of the Kalman filter, in its weighted mean filtering formulation [89], is chosen. Its implementation is described in the next section.

4.2 Implementation of a Kalman filter tracking algorithm for the IMC

The track finding problem in CALET can be decomposed in two independent two-dimensional problems, in the $x - z$ and $y - z$ views respectively. The information on each local point is two-dimensional since the single detector layer is segmented in either the x or y direction, and placed at a different z coordinate. The developed algorithm is thus a generic 2D Kalman filter, for planar 1D detectors arranged transversally along the longitudinal z axis. The transversal axis is referred to as x (or y) according with the coordinates system defined in section 2.2.2. The Kalman filter then runs separately on the x and y views to find the projections of the full 3D track, which is then reconstructed in a subsequent step from the respective projections. This two-dimensional formulation has the advantage to simplify the handling of the matrix equations and the computation of inverse matrices.

Once that the algorithm is fed with the spatial coordinates (z positions of the sensors plus the coordinates x_i (or y_i) and associated errors σ_i) of each interesting hit on the detector, the tracking algorithm starts from the upper layer along the longitudinal axis z . A candidate track is created for each hit in that plane. The initial requirement for these candidates is to pass through an hit point, while the impact angle is set by default to 0 degrees with a very large associated error. Moreover a candidate with a “missing-hit” is also created: its impact point is initially set to 0 with a very

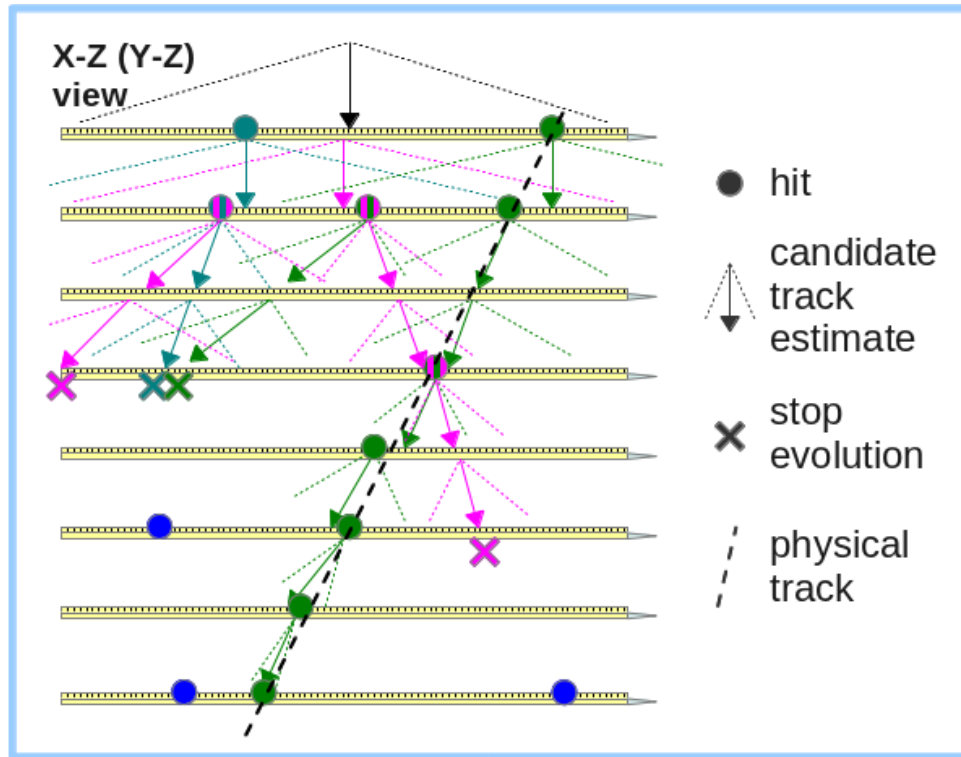


Figure 4.1: Graphical example of track finding via a combinatorial 2D Kalman filter algorithm.

large error. In this way, for every candidate, the predicted estimate of the impact point on the second layer will have a large σ . As a consequence every measurement on the second layer will be associated to the candidate producing a new possible track. This means that all the possible combinations of measurements (hits) on the first two layers will produce a track candidate. In addition also candidates with missing hits are created. Then, the track candidates are evolved separately, layer by layer. The track evolution is stopped if the χ^2/ndf or the number of missing hits exceeds some user-defined values: in particular the actual implementation of the algorithm requires $\chi^2/ndf < 50$ and a number of missing hits ≤ 2 . The track candidates that can be propagated up to the last layer are then saved into a stack of “found candidates”, while the others are eliminated.

An example of how the track finding works is shown in figure 4.1, with a simple graphical representation.

If two track candidates are composed of the same set of hits, except for the layers with missing measurements, they are defined as equivalent tracks. Once no

more track candidates are left for further propagation, all the found candidates are smoothed, or in other word the information by the full track hits sample is used to provide the best track estimate, and equivalent tracks are discarded. Different criteria are tested in order to select among these tracks the most significant ones. In particular, a simple choice of the lower χ^2/ndf is not enough because in this way the track with less points would be favoured with respect to the others. While at least in principle the track with the maximum number of points should to be preferred, anyway the presence of out-layers (spurious hits to be excluded) must be taken into account. For these reasons, at the moment two different criteria are implemented, and there is the possibility to choose among them depending on the situation. The first one simply selects the track with the largest number of points, the second one instead chooses the track with the largest number of points only if it has a χ^2/ndf not too large with respect to the other candidates. By too large we mean greater than 150% as optimized after some trials.

Among non-equivalent tracks, “physical” tracks are identified by means of another χ^2/ndf cut with a user-defined threshold ($\chi^2/ndf < 10.0$ in this implementation), and among the physical tracks the primary track is selected using a user-defined criterion. This criterion is based on the energy deposit in the TASC calorimeter, associated to the track: the IMC reconstructed track that has the largest energy deposit in the TASC is chosen as the primary one. Effectively all the IMC tracks are extrapolated to the TASC plane positions and if compatible clusters are found, the energy deposit corresponding to the nearest is associated to the track. While, in case there are less than three plane per view with at least one cluster in TASC, this criterion is not used, but it is replaced by a simple one, and the physical track with the lowest χ^2 is presented as the possible primary. For the Beam Test 2012 data (TB2012), due to the incomplete instrumentation of the TASC detector (only 3 PWO crystal per plane), this criterion had to be modified and a simpler one is used instead: the primary track is identified as the one with the largest energy deposit in the IMC.

The current implementation does not account for multiple scattering. A dedicated study (analytical or based on MC simulations) is necessary to estimate the noise

vector w_k to be added to the evolution equation, and it has been postponed for future developments. Because, as the interest is on primary cosmic rays, with energies > 10 GeV, and taking into account the IMC granularity, multiple scattering (that is inversely proportional to particle momentum [91]) seems not to be an issue for tracking with the IMC detector.

In a first implementation of the algorithm the tracking was performed on the whole detector volume, but due to the large hit multiplicity the reconstruction of all the possible tracks requires a lot of computation time. For this reason, taking into account that the main focus of the IMC is to reconstruct the “primary” track (belonging to the incident particle), the algorithm is improved adding the possibility to limit the track searching volume to a small “road-of-interest” (ROI) inside the detector. This road is defined as a cylinder around the axis of the shower and with a radius of 5 cm. To find the shower’s axis, a track reconstruction algorithm similar to the one described above is performed on the TASC detector (see section 2.2.3). In this case, given the relatively low number of hits per event due to the coarse granularity of the TASC, the track finding is not so computationally expensive. After a detailed comparison, it has been proved that the ROI choice does not affect the tracking performances (described in detail in the next sections), that remains almost the same, except for the reconstruction of low energetic protons that is slightly less efficient. On the other hand, the computation time is greatly reduced.

An important pre-requisite for tracking is a proper definition of “hit”. Conceptually, a hit is defined as the point in which the incoming particle has crossed the detector. In reality, the IMC is a collection of planes of scintillating fibers that return a signal proportional to the energy deposited by the particle in the crossed fibers, and also from neighboring one (due to the presence of delta rays). For this reason, all the fibers with a signal above a threshold, significantly higher than the electronic noise are clustered to form one single hit for the track finding. The coordinates of this candidate hit are defined along z by the nominal position of the plane to which it belongs, while along the x (or y) direction they are calculated as a truncated mean weighted on the deposited energy from the nominal positions of the fibers belonging to the cluster. In this context, we refer to the mean computed

data	type	energy (TeV/n)	spectrum	events	note
MC	electrons	[0.02, 2]	E^{-1}	224000	–
MC	protons	[0.01, 100]	E^{-1}	619300	–
MC	helium nuclei	[0.01, 25]	E^{-1}	629100	–
MC	carbon nuclei	[0.03, 3]	E^{-1}	144000	–
TB2012	muons	0.150	–	40959	–
TB2012	electrons	0.250	–	17416	–
TB2012	protons	0.030	–	46336	–
TB2012	protons	0.100	–	74251	–
TB2012	protons	0.400	–	24223	$\sim 20^\circ$ tilt

Table 4.1: Main features of the data samples used for tracking algorithm tests and validation.

choosing only the fibers of the cluster within 2.5 mm (on each side) from the most energetic one. The uncertainty σ on the x (or y) position corresponds to the square root of the variance of the weighted mean.

4.3 IMC tracking performances

In this section we present the results of an extensive study performed on the tracking algorithm described above. This work was mandatory in order to discover possible issues or features related to the track reconstruction, and also to know the performances of the detector itself in the identification of the primary particle direction.

The tracking performance of the IMC depends clearly on the incident particle species and energy. For this reason the implemented algorithm was tested on different kind of Monte Carlo programs and beam test data samples, in particular: Monte Carlo interaction of electrons, protons and ions (helium and carbon nuclei) simulated with FLUKA; protons, electrons and muon events recorded during a dedicated beam test in 2012 (TB2012) at CERN North area facility in Preveessin (SPS extracted beams). The data samples used for this analysis are summarized in the table 4.1.

The simulated events, were generated isotropically in direction and according to a power law spectrum. For beam test data instead, the analysed samples were taken with a collimated beam at normal incidence with respect to the detector planes,

with the exception of the 400 GeV protons sample that have an incidence angle of about 20° .

4.3.1 Fluka simulated data

The first checks during the implementation of the track reconstruction algorithm have been performed with Fluka MC data samples. These tests have permitted to evolve the algorithm according to the detector requirements and capabilities. Once that the algorithm stability was reached, other and more refined tests were made to evaluate the tracking performances. The results of this study are presented in the following.

First of all, MC data samples allow to estimate the tracking efficiency by comparing the number of events for which a primary track is reconstructed with respect to the total number of simulated events in which a particle crosses the detector. The efficiency is calculated taking into account only the particle inside one of the four acceptance criteria defined for the CALET telescope, (see section 2.4). The resulting estimates, show an overall efficiency of about the 90-95% for protons, helium nuclei, electrons and of $\sim 98-99\%$ for carbon ions.

Other important parameters that can be estimated from the simulation are the angular and spatial resolutions. In particular the angular θ resolution is evaluated separately for the two views, taking into account θ_x and θ_y angles between the projection of the 3D track and the axis of the detector in the $x - z$ and $y - z$ plane, respectively. The spatial resolution is evaluated at the particle incidence point on the top of the CHD ($z = 0$), because the reconstruction of this point is of particular interest, as it allows to identify the CHD paddles that has been crossed by the particle and that are used for charge reconstruction.

As per the angular resolution, first the residuals between MC truth and reconstructed information are computed (i.e. $\Delta\theta_x = \theta_x^{MC} - \theta_x^{reco}$ and $\Delta\theta_y = \theta_y^{MC} - \theta_y^{reco}$). Then, a Point Spread Function (PSF) is calculated from the residual distributions, as the half-width of the interval centred on the mean value and containing 68.3% of the events. In a similar way, the residuals for the x and y coordinates are calculated as the distance between the true position (x_{MC}, y_{MC}) of the incident particle at $z = 0$

and the one extrapolated from the reconstructed track (x_{reco}, y_{reco}) . The residuals are $\Delta x = x_{MC} - x_{reco}$ and $\Delta y = y_{MC} - y_{reco}$, for the x and y view, respectively. Moreover, to quote a σ value for the resolution, a 68.3% interval around the mean is defined, in analogy with the PSF.

The θ_x and x residuals for the electron sample are displayed in figure 4.2 (a) and

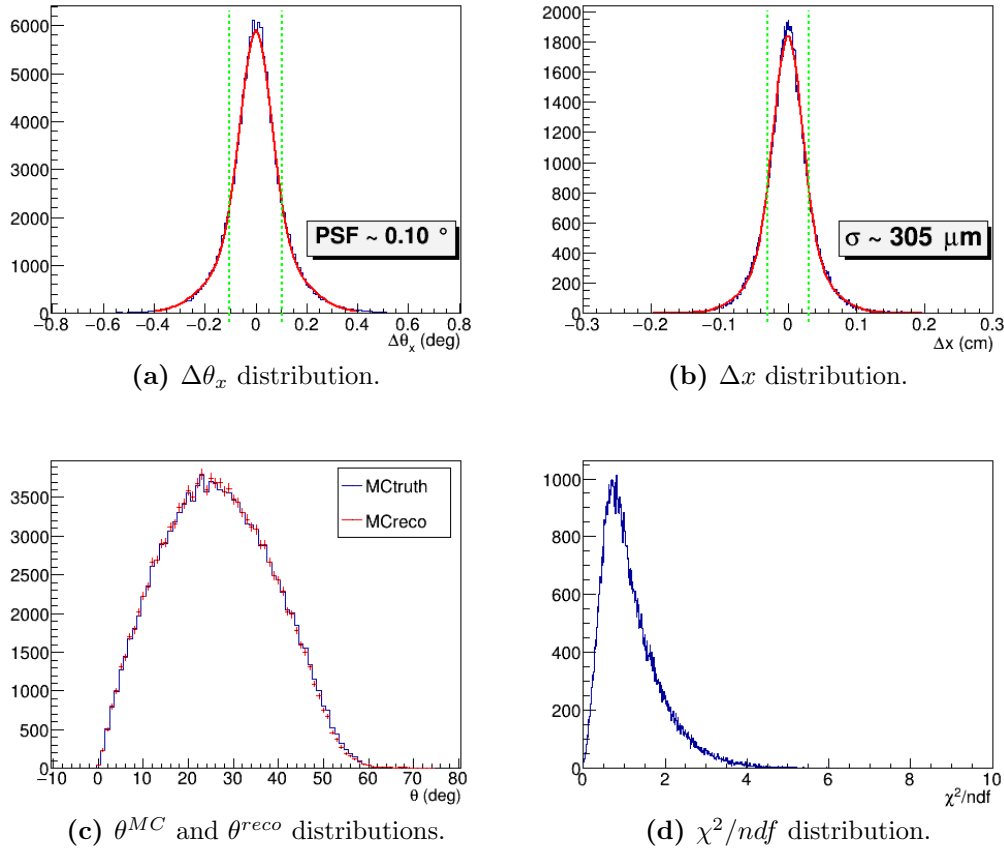


Figure 4.2: A selection of plots showing the tracker performances for the MC electron sample, for different parameters: (a) residuals $\Delta\theta_x = \theta_x^{MC} - \theta_x^{reco}$ distribution; (b) x coordinate residuals $\Delta x = x_{MC} - x_{reco}$ measured on the CHD surface; (c) zenith angle of incident particle from MC (blue line) compared with reconstructed one (red marker); (d) χ^2 distribution for the reconstructed track.

(b), while the equivalent plots for θ_y and y are not shown, for brevity, but they have a similar behaviour. These distributions look considerably narrow, with the PSF for θ_x being about 0.1° and $\sigma_x \approx 305 \mu\text{m}$, with a shape that can be approximated well by a sum of two Gaussians, with the same mean and different variance. A fit to this function is performed and it is shown as the red continuous line. In the same figure 4.2 plots (c) and (d) show respectively: the reconstructed zenith

angle θ (red marker) superimposed to the corresponding true MC parameter (blue line), and the distribution of χ^2/ndf for primary tracks. From these histograms it seems evident that for electrons the θ distribution is well reproduced, and the χ^2 distribution is well-behaved: with the Most Probable Value (MPV) around 1.0 and the characteristic long right tail.

For what concerns the study of the tracking performances with simulated protons and carbon ions, a distinction is made between non interacting particles (i.e. MIPs events, at our energies) and interacting ones. In particular, for CALET, MIPs are important for calibration, while hadronic particles, that undergo to a process capable to generate an High Energy Trigger (HET) in the calorimeters, are important for ions physics. HET is the main trigger mode for CALET: it requires a large energy deposit in the middle of the calorimetric section of the detector, and it targets protons and nuclei of a few 10 GeV to 1000 TeV (see section 2.3). For these reasons the analysis described in this section is focussed only on these type of events. Results for particles not generating an HET event are not reported. On the other hand MIP and HET events are studied in detail. The most significant plots are displayed in the figures 4.3 and 4.4, while all results are summarized in table 4.2.

Figure 4.3 refers to the Fluka simulated protons and shows the distributions of $\Delta\theta_x$ and Δx (histograms (a) and (b), respectively), both for HET events and for non interacting minimum ionizing particles (plots (c) and (d)). From these histograms, after comparison with those of figure 4.2, it seems evident that for minimum ionizing protons the tracking algorithm has the same performances that for electrons. On the contrary, for interacting events the situation is a bit worse. While the residuals have a similar shape, the distributions are wider by about a factor 3. However this is to be expected because track finding and also primary track identification is more difficult in the case of hadronic interacting particles. In fact these events are characterised by a higher track and cluster multiplicity in the detector, that make both the tracking and the primary selection more complicated. Anyway, also if in case of HET events the performance of the tracking algorithm though worse than in the case of MIPs or electrons, it remains within the required specifications for our detector. For brevity, as in the case of electrons, the histograms of the residuals

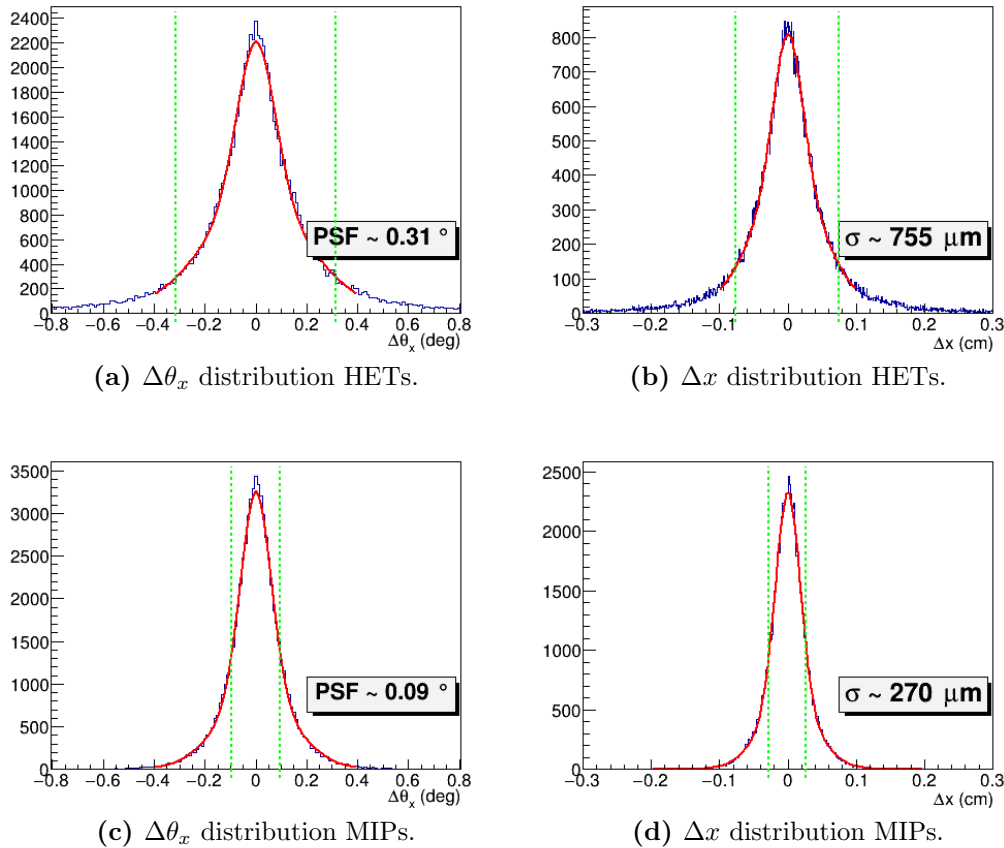


Figure 4.3: A selection of plots showing different tracking parameters, for the MC protons sample; (a) and (b) are respectively the $\Delta\theta_x$ and Δx distributions made for HET events, while (c) and (d) represent the same quantities for non interacting (MIP) particles.

related to the y coordinates are not shown as they have a very similar behaviour as in the other view.

Regarding the algorithm performances with ions, in figure 4.4 are shown the residuals of θ_x and x (at $Z = 0$) with respect to the true MC parameters, both for helium (plots (a) and (b)) and for carbon nuclei ((c) and (d) in figure). All the displayed histograms refer to interacting events, as they are the most interesting ones from these data samples. Anyway, for MIP events, there are not remarkable differences of performances between the different particle species analysed. From the first two plots of figure 4.4 it is possible to notice that the track reconstruction works for helium in a complete similar way as for protons, and that there are no significant differences in performances between events from two species. On the other hand, for carbon nuclei the tracking algorithm seems to work better, in comparison to

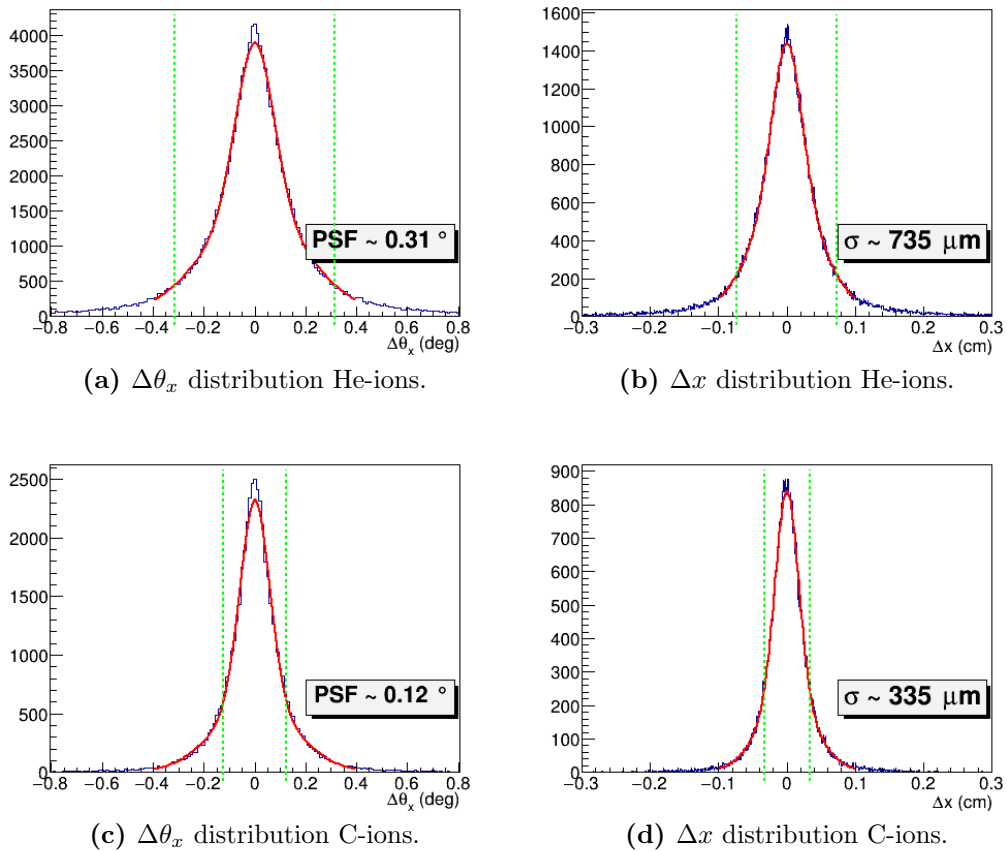


Figure 4.4: Tracking performances for helium and carbon ions MC data samples. Shown are the residuals distributions for θ_x and the x coordinate of the incidence point, only for interacting particle generating an HET event: (a) and (b) plots refer respectively to $\Delta\theta_x$ and Δx for the helium sample, while (c) and (d) show the same quantities for carbon ions.

proton or helium HET events, as both $\Delta\theta_x$ and Δx distributions are narrower. This can be in part related to use of TASC energy deposit information for the primary track selection, as it is observed to work better for heavier ions than for protons or helium. Moreover heavier elements produce, on average, a lower number of clusters (but wider in width) near the primary track with respect to lighter elements, and this can ease the track reconstruction.

In conclusion the Kalman filter algorithm implemented for tracking as described above allows to achieve a high tracking efficiency together with a good resolution, both in spatial and in angular coordinates. The performances for all the analysed samples with MC simulated data are summarized in table 4.2. As expected, the performances are worse for HET events, than in the case of MIPs or electrons,

particle type	energy range (TeV/n)	efficiency	$PSF_{\theta_x-\theta_y}$	σ_{x-y} (μm)
electrons	[0.02, 2]	0.95	0.10°	300
protons (MIP)	[0.01, 100]	0.94	0.10°	260
protons (HET)	[0.01, 100]	0.91	0.31°	750
helium nuclei (MIP)	[0.01, 25]	0.95	0.09°	260
helium nuclei (HET)	[0.01, 25]	0.93	0.32°	740
carbon nuclei (MIP)	[0.03, 3]	0.97	0.09°	210
carbon nuclei (HET)	[0.03, 3]	0.98	0.12°	330

Table 4.2: Performance of tracking algorithm tested on different MC data samples.

because track finding and also primary track identification are complicated by the much higher track and cluster multiplicity in the detector. Nevertheless they turn out to meet the requirements of the CALET instrument. In the next section, the analysis performed on a selection of beam test data sets is presented in order to complete the review on the tracking capability of the IMC with data for the real detector.

4.3.2 Beam test data

In the following, a brief study is presented on the validation of the track reconstruction in the case of test beam particles.

Before starting with the description of the actual work a few points have to be mentioned. First of all, as already discussed in section 4.2, for the beam test analysis the primary track selection criterion is modified with respect to MC data. In this case the primary track is identified as the one with the largest energy deposit in the IMC, instead of the one that has associated the largest energy deposit in TASC.

For that reason the results from this analysis are not directly comparable with the MC ones, yet they are useful to understand how the algorithm behaves with real data.

For beam test data samples, a preliminary alignment and calibration of the IMC fibers is mandatory, as plane misalignment and a non uniform fiber response can bias the tracking, leading to a degradation of the tracking performance.

Moreover, for this study an event selection is needed in order to reduce analysis biases due for example to events out of acceptance and not hitting the IMC (e.g.:

particles from the beam halo, etc.). For this purpose it is used a secondary detector with tracking capability, called Beam Tracker (BT).

This detector consists of a telescope with 4 planes of silicon strips (with $700\ \mu\text{m}$ pitch), plus 4 silicon matrix with 64 pixels of $1 \times 1\ \text{cm}^2$ area for charge identification.

In particular a cut on the BT track parameters it is performed, to select only the events with a single track pointing to the IMC detector.

Calibration and alignment

A preliminary alignment and calibration of the scintillation fibers (SciFi) is needed. In particular, the TB2012 data samples that were analysed were taken with a non uniform High Voltage configuration (except during muon runs). This means that not all the PMTs collecting the signal of the IMC scintillating fibres were set at the same potential. Instead, two out of the four HV channels were set to 800 V, one at 700 V and the other to 600 V for the purpose of collecting data with different gains. As each channel supply the HV to four consecutive planes, this implies that the last 8 planes of the IMC were working at a lower HV respect to the first 8. Here, with “first” we mean the plane nearest to the beam extraction point. This introduces a dependence of the detector response on the plane crossed by the incident particle. For that reason, calibrations of data are of particular importance, especially in the case of MIPs. Gain calibration is performed to equalize the response of the detector, otherwise the recorded energy deposits of a crossing particle would be higher in some planes (with higher HV) and lower in others.

The detector calibration is made by using a sample of minimum ionizing particles (muons at 150 GeV), and measuring the Most Probable Value (MPV) of the particle energy deposit in each fiber. Then, the MPV values are used to translate the deposit of each fiber from ADC count units to “number of MIPs” units. In this way, for each fiber, the energy deposit is equalized to a value that is related only to a fundamental quantity (the unitary charge), and not any more dependent on the fiber itself or on the PMT characteristics. After this step, in order to reject electronic noise a threshold of 0.2 MIP (identical to the one chosen for the MC data analysis), is

applied to each fiber.

The MPVs are measured from muons data samples, filling an histogram for each fiber with the energy deposited by the crossing particle. Then, these histograms are fitted with a probability density function(PDF) which is the convolution of a Landau with a Gaussian distribution. The MPV value is computed from the fit result. An example of the energy deposit distribution in a fiber is shown in figure 4.5 (a), together with the relative Landau*Gaussian fit. To have an idea of the effect

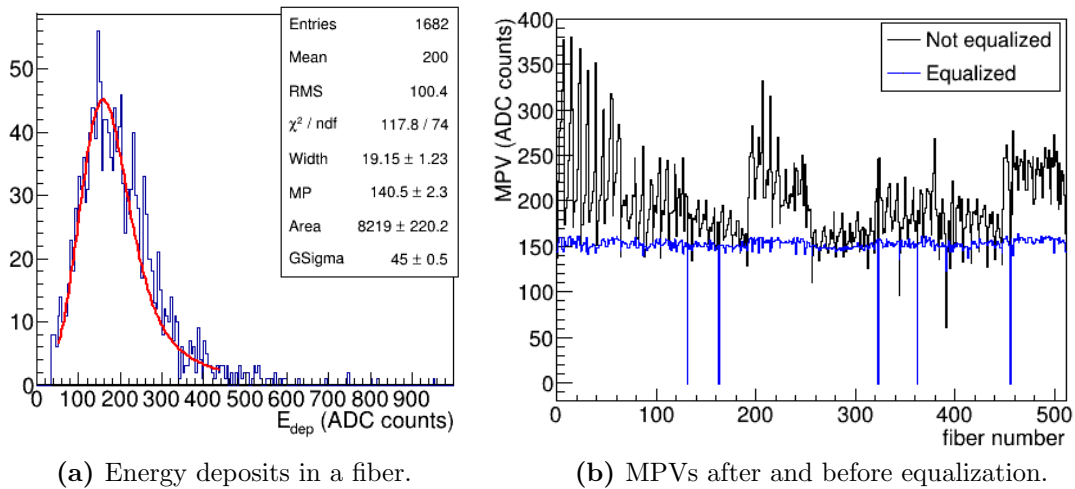


Figure 4.5: In (a) histogram of the energy deposited (in ADC counts) in a fiber crossed by muons; (b) MPVs of these distributions versus the fiber number.

of fiber equalization, in figure 4.5 (b) the histogram is shown of the MPV (in ADC counts) vs. the fiber number, both for uncalibrated (black line) and calibrated data (blue line). This plot refers to the fibers of two consecutive IMC layers (512 fibers) of the same view (y), arranged according to a numeration scheme that groups together all the 64 fibers connected to the channels of a single MAPMT (see section 2.2.2). In fact, the 512 SciFi of 2 planes are read out by 8 MAPMTs with 64 channels each, whereby each MAPMT has a slightly different response. Moreover inside each MAPMT, single channels are arranged in a 8×8 matrix, and a dependence between the matrix column and the channel gain has been reported [49]. All these features can be observed in the histogram of MPVs before equalization, represented by the black line in figure 4.5 (b). In fact, a coarse structure is visible, that affects groups of 64 channels (from 0 to 63, from 64 to 127, etc.), and is related to the different

MAPMTs. A finer structure is also visible, involving groups of 8 channels (with an enhancement every 8 fibers), due to the different gain of the channels inside the MAPMT itself. The blue line of figure 4.5 (b), instead, shows how all these features are corrected by applying the calibration. Application of the equalization parameters to the data results into a sizeable improvement in the MIP identification. However, there is still room for improvement as the available data statistic for muons taken with the same voltage setup as for protons and electron runs is too low to allow a very accurate calibration. Moreover the HV on the last 4 plane (600 V) is at the limit to allow the MIPs identification, and probably for some events some hits in these planes may have fallen under threshold.

For what concerns the fiber alignment, this is achieved using a χ^2 minimization method, which is performed on a muon data sample, separately for the two views. Operatively, once the fibers are equalized, the Kalman filter algorithm is applied for a first pass to reconstruct tracks. Then a minimization procedure is applied to χ^2 of eq. 4.1 and 8 S^j shift parameters are extracted. The S^j corrections are then applied to the relevant j planes, and the procedure is repeated iteratively, until the shift parameters become sufficiently small.

$$\chi^2 = \sum_{i=1}^{N_t} \sum_{j=1}^{N_l} \left(\frac{x_{SciFi}^{ij} + S^j - (p_0^i + p_1^i z^j)}{\sigma_x^{ij}} \right)^2 \quad (4.1)$$

In equation 4.1: N_t represents the number of tracks reconstructed; N_l is the number of detector layers (8 per views in the IMC case); p_0^i and p_1^i are the parameters of the i -th track; z^j is the z position of the j -th plane; x_{SciFi}^{ij} and σ_x^{ij} are the nominal position and uncertainty of the fiber hit by the i -th track on the j -th plane; S^j are the already mentioned free shift parameters.

Performances after alignment and calibration

After application of the preliminary calibration and alignment procedure briefly described above, track reconstruction is performed in the case of beam test data.

First, as already mentioned, an external tagging of the events is applied using the information from the Beam Tracker (BT) to select events with one track pointing

to the IMC. This allows to estimate a tracking efficiency, as the fraction of events with a reconstructed track in the IMC among the ones that pass the BT selection. In particular, it is found that for 250 GeV electrons the algorithm is fully efficient, while for 150 GeV muons, and protons (of 30, 100 and 400 GeV) the efficiency is about 95-96%. Efficiency and others tracking parameters are summarized in table 4.3.

The cuts on BT parameters are made both on the incidence point of the track on the detector upper layers, and on the track reconstructed polar angle θ . In particular, a core region inside the beam spot is selected as shown in figure 4.6 (b), where the BT reconstructed particles impact points in the $x - y$ coordinates are drawn, together with the cut region delimited by red lines. Then the track angle θ is required to lie in the interval $[0, 0.2]$ degrees.

To have a first visual check of the IMC behaviour, it is possible to compare figure 4.6 (b) with 4.6 (a), where the 250 GeV electrons $x - y$ beam profile is shown as reconstructed by the IMC (obviously before the BT selection). As it is expected, the IMC reconstructs a very similar profile to that measured by the BT, but not identical as it is taken at a more downstream position.

Going a little bit into the details of the reconstructed tracks parameters, the χ^2/ndf and θ_y distributions are shown respectively in fig. 4.6 (c) and (d). The χ^2/ndf distribution looks well behaved, without anomalous features or unreasonable too high or too low values. The θ_y distribution instead reflects the beam divergence in the y projection as measured by the IMC. Thus, the quoted value of 0.25° for the PSF originates both from the tracking angular resolution and from the beam intrinsic divergence, and the two contributions cannot be separated. In fact, in the case of real data and differently from the MC, the true track parameters are unknown and residuals cannot be calculated. Anyway the θ_y distribution is considerably narrow, as expected from a “parallel” well tuned beam, and, at least for electrons, without strange features that could stem from possible tracking artefacts. The θ_x distribution (not shown for brevity) is quite similar, though a bit narrower.

Along the same line of checking for possible tracking issues, the θ_x , θ_y and χ^2/ndf distributions are computed also for the other beam test samples. In particular, in

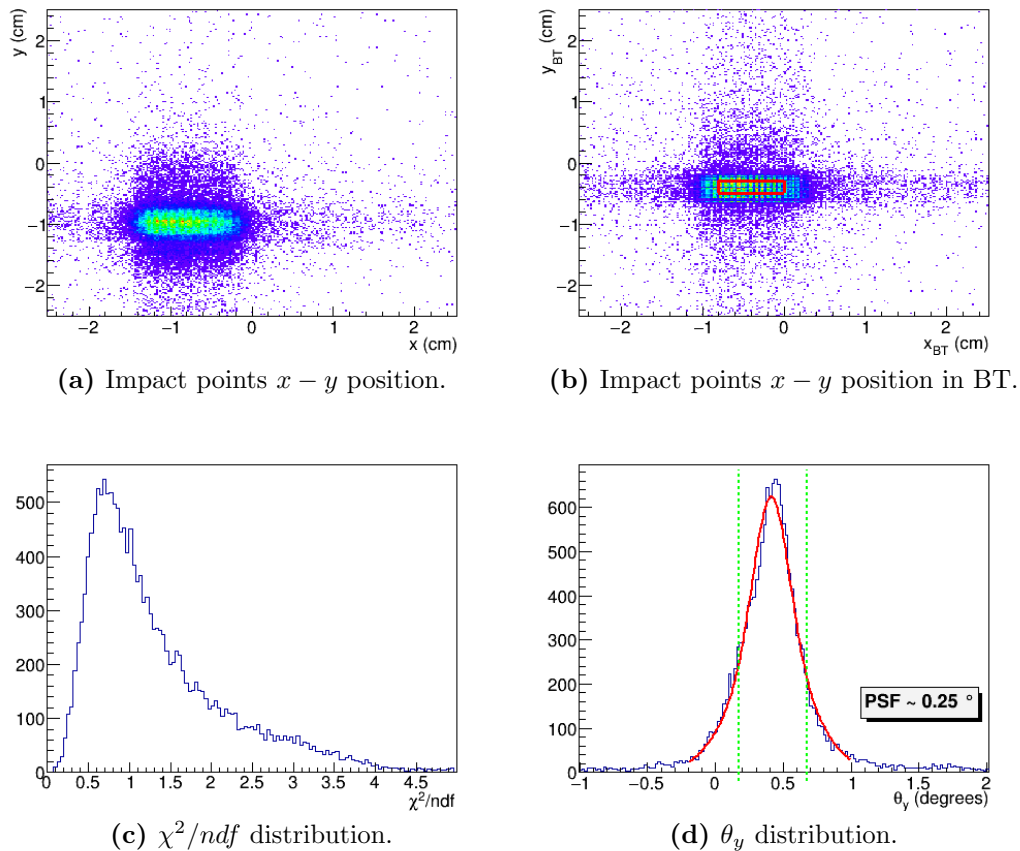


Figure 4.6: Beam profile in the $x - y$ coordinates for a sample of 250 GeV electrons, as reconstructed by the IMC (a) and the BT (b) detectors. χ^2/ndf (c) and θ_y (d) distributions of the IMC reconstructed track, after the BT selection, for the same data sample.

figure 4.7 the histograms of χ^2/ndf and θ_y distributions are shown for 400 GeV protons and 150 GeV muons. For brevity, the corresponding plots for 30 and 100 GeV protons are not displayed. They behave in a very similar way and their distribution parameters are written in table 4.3, together with the tracking efficiency.

From inspection of the figure 4.7 we can conclude that also in case of muon (MIPs) and protons the χ^2/ndf distribution shape does not exhibit any anomalous features, and the parameter values are reasonable. The same considerations hold also for the θ_y distributions, that have a less smooth shape if compared with that of electrons, but a comparable width. Moreover, for the 400 GeV proton sample, we notice that the θ_y distribution, in figure 4.7 (d), shows a $\sim 20^\circ$ tilt (with respect to beam axis). This is expected, because it reproduces the geometrical layout of the beam test run in which this data sample was acquired with the detector tilted by a similar amount.

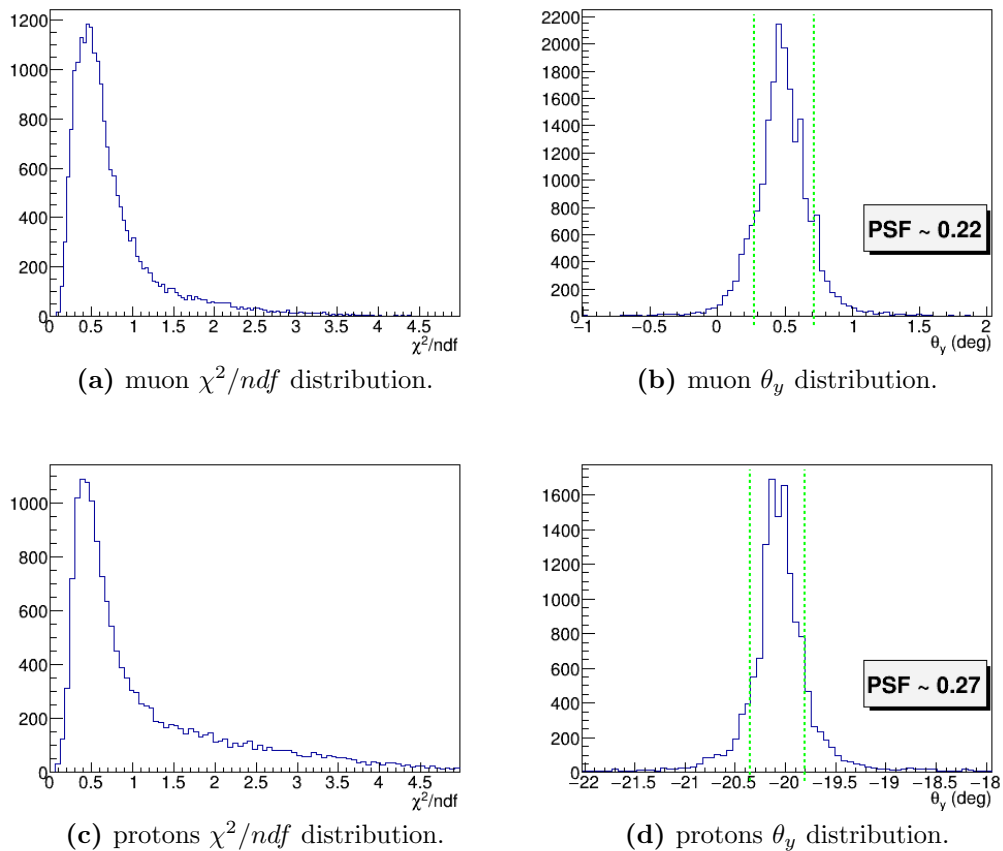


Figure 4.7: Distributions of χ^2/ndf and θ_y for the 150 GeV muon sample (a) and (b) respectively, and for the 400 GeV protons sample (c) and (d).

In conclusion, the tracking algorithm seems to work well also in case of real data, behaving as expected. The tracking efficiency is sufficiently high, more than 95% for all the beam test data samples analysed, and the different checks performed have not found any relevant issue.

particle type	energy range (TeV)	efficiency	PSF $_{\theta_x}$	PSF $_{\theta_y}$
electrons	0.250	1.00	0.17°	0.25°
muons	0.150	0.95	0.26°	0.22°
protons	0.030	0.96	0.22°	0.22°
protons	0.100	0.96	0.22°	0.22°
protons	0.400	0.96	0.21°	0.27°

Table 4.3: Summary of tracking performances with beam test data.

Chapter 5

Charge measurement with the IMC

The measurement of the electric charge of the incoming particle is essential to separate different elemental species among the fully stripped nuclei that are present in the cosmic ray flux. For this reason, although CALET has a dedicated CHarge Detector (CHD) on top of the instrument, a redundant measurement of charge is of great importance especially at high energies, where charge tagging in the CHD becomes more challenging, due to the albedo of backscattered particles emerging as secondaries from the interactions in the calorimeter.

The IMC characteristics are suitable for this task, as its fine granularity helps reducing the contamination from backscattering. Moreover the 16 SciFi layers allow to collect a good sample of specific ionization measurements from which one can infer the value of the charge Z . On the one hand, multiple dE/dx measurements can recover the potential problem of the low photostatistics from a single scintillating fiber, due to the IMC fibers thickness of 1 mm to be compared with the 1 cm thick plastic scintillators (paddles) of the CHD. On the other hand, the interaction probability inside the IMC (especially in the tungsten plates) is not negligible and this makes charge identification more difficult.

The basic idea behind this measurement is to use the well known proportionality of the energy loss by ionization with Z^2 , in order to infer the charge from the energy deposits of the incoming particle in the IMC traversed fibers. This task can be

performed in four consecutive steps. First of all, the track of the primary cosmic ray must be reconstructed. Then, the interaction point (IP) of the particle inside the detector has to be identified. The average $\frac{dE}{dx}$ is then estimated, and finally the value of the charge is assessed. The first step is needed to obtain the energy deposits associated to the incoming CR, and it is accomplished by the tracking algorithm, described in chapter 4. To carry out the remaining steps, different methods have been studied and tested. The work done in order to develop these algorithms is described in the present chapter together with the expected overall performances of the charge identification of helium and proton cosmic nuclei, both from simulations and from real beam test data.

These two specific analysis tools have been developed in view of a measurement of cosmic ray proton and helium spectra with CALET flight data.

5.1 Reconstruction of the interaction point

For this analysis it is mandatory to reconstruct the particle interaction point (IP), because, after the interaction, the particle can no longer be considered as a MIP. Therefore only the energy deposits in fibers ahead of the interaction point can be used to get a measurement of the energy loss by ionization.

To identify the IP, two different ad-hoc algorithms, called *A* and *B*, have been implemented. The idea behind both algorithms is similar. Basically it is assumed that, as the particle undergoes an interaction, the energy deposits along the primary track will change considerably. Therefore the goal is to identify a “discontinuity” along the track in the energy deposit values.

Method *A* is conceptually more simple, and proceeds in three steps. In the first step all the IMC layers are considered, and for each plane the average $\frac{dE}{dx}$ is calculated using all the available samples, from the top of the IMC to the layer under study. The variance is computed as well. Then, a test is performed plane by plane, starting from the top of the detector and moving to the bottom. It is checked whether the difference between the mean $\frac{dE}{dx}$ on the previous plane and the actual one is larger than 2 times the variance (computed from the previous plane). In this case, the layer

is “tagged” as a possible plane in which the interaction occurred. Finally, in order to avoid that a simple fluctuation in the energy loss could lead to a misidentification of the IP, a second scan is performed on all the layers to verify the existence of a point starting from which all the following planes are “tagged”. In this case, it is identified as the interaction point.

In method *B*, instead, for each layer the probability that a certain energy deposit belongs to a specific ion of charge Z it is computed. Then the algorithm loops over all planes, from the top to the bottom of the detector, searching for a plane in which the probability becomes too small (below a given threshold). If such a plane is found, and the probability to be a m.i.p. particle of charge Z remains under threshold also for two more consecutive planes, the z coordinate of plane is associated to the IP. Clearly the incoming particle identity is not known a priori (for real data), unless the CHD is used for a preliminary tagging, but this is not in the aim of the present study. For this reason the procedure described above is applied concurrently for all the Z charges in a range of interest, and then the right interaction point is chosen “a posteriori” together with the most probable charge.

To compute the probability that a certain energy loss is associated to a given Z , the energy deposit distributions are extracted layer per layer, for all the charges in the given range. Then all these histograms are normalized to 1 (template distributions), and given a certain nuclear species X , and a specific plane L , the probability that the X particle have deposited an energy ΔE crossing L is represented by the value of the corresponding normalized histogram in ΔE . To be more rigorous, for each layer a normalized energy deposit straggling function f_p should be computed, for each particle p , fitting the histograms, and then the probability density function should be evaluated as $f_p(\Delta E)$. Anyway performing these fits is not always simple, and after some trials it was decided to discard this rigorous approach, as it appears to not bring any significant improvement, despite a higher difficulty of implementation.

Both methods have been tested and shown to work well, for a wide range of incoming particle energies, and have different strengths and weaknesses. In particular the algorithm *A* seems a little more robust, because doesn’t need any a priori information, and it works in the same way for all the particles. On the contrary,

method B , that turns out to be a bit more accurate, needs to know the straggling functions (or the equivalent template distributions) for each type of particle under investigation. This information must be extracted preliminarily, from MC simulations or from the data itself, and can introduce additional systematics. As the straggling functions vary slightly with the energy, this must be taken into account to achieve a better performance.

Tests on these IP reconstruction algorithms have been made mainly with FLUKA simulated data. Two main data samples have been used, one of protons and the other one of helium nuclei, both generated isotropically, in a wide energy range from 100 GeV to 100 TeV, and with energy spectra parametrized with a single power law with spectral index -1. Some preliminary cuts were made on the FLUKA data, in order to make an event selection and to evaluate the performances of the methods only for interesting events. This selection consists of two cuts on the event topology, plus an additional one on the quality of the reconstructed track. That is mandatory, since clearly the interaction point can only be found when the incoming particle has been tracked properly. For this reason the angular separation between the true MC track and the reconstructed one (computed by the scalar product) it is required to be less than 0.8 degrees. The first topology cut is on the acceptance type, only events of type “1” are used, which means that the particle has to cross the whole detector (from the top of CHD to the bottom of TASC). The second cut is related to the trigger: only cosmic rays generating an High Energy Trigger (see section 2.3) are taken into account, rejecting low energy events that are not interesting for the spectral measurements above approximately 10 GeV. Moreover for method B , each data sample has been split into two sub-samples: one for the “training” of the algorithm, that is the extraction of the normalized histograms, and the other one for the actual test. To take into account the dependence of the straggling functions with the energy, the training sample has been divided into 12 logarithmic bins, and a set of histograms has been calculated, on a bin basis.

To evaluate the accuracy of the developed methods, in figures 5.1 and 5.2 it is shown the difference, in the z coordinate, between the true IP and the reconstructed one, that is $\Delta z_{int} = z_{int}^{MC} - z_{int}^{reco}$. In more detail, figure 5.1 shows the residuals

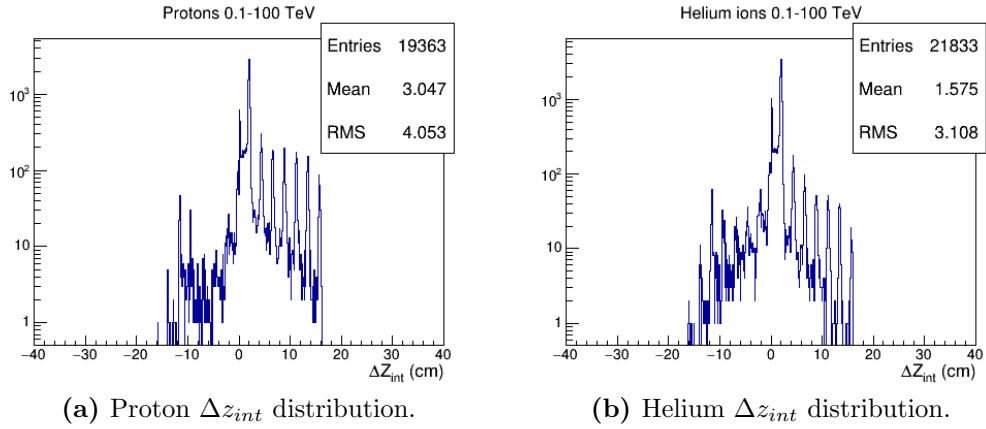


Figure 5.1: Distributions of residuals, between the true interaction point z coordinate (from MC simulation) and the reconstruct one (from method A). These distributions are made both for a protons sample (a) and for a helium ions sample (b) of FLUKA simulated data, in the energy range from 100 GeV to 100 TeV.

distributions computed using the method A , both in the case of the proton data sample (a), and for helium ions (b). In figure 5.2 the same kind of histograms are shown, but the analysis has been performed with the other method.

In both cases it is possible to observe that the algorithms work well and with a really good accuracy for both particle types. In fact, in most cases the IP is reconstructed correctly within plus or minus one plane, that is a distance of about 4 cm. In a small number of cases (notice the logarithmic y scale) the reconstruction fails. There are not significant differences in the behaviour between the two different methods, nor between the two kind of particles under test.

There are few other points to notice. First of all the histograms shown a sort of “quantized” behaviour, with some peaks equally spaced apart. This is expected, because z_{int}^{reco} can only take discrete values, corresponding to the z coordinates of the different IMC layers. Moreover the IMC is not a homogeneous calorimeter, and the interactions are more likely to occur in the tungsten plates rather than inside the SciFi layers or in the honeycomb support structures. A consequence of this is also that the displayed distributions have not their maximum in zero, but approximately around 2 cm. In fact, when the reconstruction works well, z_{int}^{reco} is the z coordinate of the last plane before interaction, while in the most cases the z_{int}^{MC} is that of the following tungsten layers, that is about 2 cm downstream.

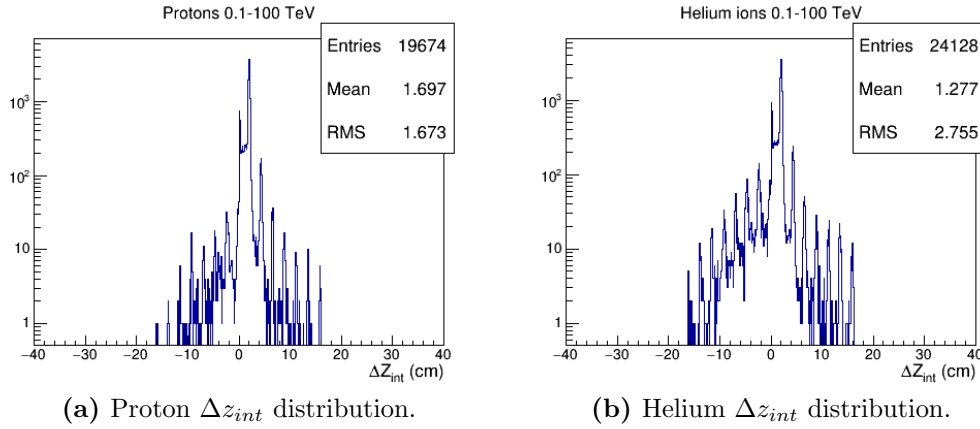


Figure 5.2: Distributions of residuals, between the true interaction point z coordinate (from MC simulation) and the reconstructed one (from method B). These distributions are generated both for a protons sample (a) and for a helium ions sample (b) of FLUKA simulated data, in the energy range from 100 GeV to 100 TeV.

Another important thing to point out is that, clearly, it is not possible to extract any information on the interaction if that occurs outside the IMC detector, i.e. in the CHD or in the TASC. For this reason all the plots shown refer only to events where the particle interacts inside the IMC. In this case it is possible to compute a proper IP reconstruction efficiency. Anyway it is also interesting to check if an interaction occurring inside the CHD or the TASC generates a reconstructed IP in the IMC or not.

For events with an interaction inside the IMC, the reconstruction efficiency with method A is about 98% for protons and 89% for helium ions. When the IP occurs in the TASC the probability that it is reconstructed anyway inside the IMC is of $\sim 40\%$ for protons and $\sim 12\%$ for helium. This however is not so dramatic for charge identification, but it only means that, for this kind of events, the whole data sample available to estimate the charge with the IMC will be used only in 60% of the cases for protons and in 88% for helium. In the other cases the IP is reconstructed upstream with respect to the real position, and only a limited number out of the 16 theoretically available energy deposits will be used for the measurement.

Using method B , the IP detection efficiency is about 98% for protons and 96% for helium nuclei. Moreover the probability that an IP is reconstructed (in the IMC) also for events interacting in the TASC drops to $\sim 22\%$ for protons and to $\sim 24\%$

for helium.

A separate discussion should be made for events interacting in the CHD. This kind of events are the most problematic for the measurement of charge, and there is no possibility to infer any information on them using the IMC alone.

The only possibility to deal with this problem is to apply some cuts to remove these events from the analysed sample. In this scenario, method B produces a sort of “automatic” rejection of this kind of contamination. In fact, by applying a threshold on the probability that a certain energy deposit belongs to a specific particle, then, if the deposits are under threshold from the beginning for all the particle types under investigation, it follows that the event has to be discarded.

This embedded cut, without any additional one, provides (for the actual implementation of the algorithm) a rejection larger than 60% for events interacting in the CHD, both for protons and for helium. Clearly this can lead also to the unwanted rejection of particles that interact in one of the calorimeters. As a matter of fact, for interactions in the TASC it is found that less than 0.1% of the events are discarded, and for the IMC the rejected particles are about 1% of protons and 2% of helium nuclei. This is not completely unexpected, as for events interacting in the first layers of the IMC the same considerations previously made for the CHD hold.

To conclude, inspecting figure 5.1 and 5.2, it is possible to note that for protons the residual distributions made with method B are more symmetric, and narrower with respect to that computed with the other algorithm, which instead have a greater RMS and a sort of “tail” on the right hand side, suggesting an attitude to underestimate the position of the interaction point z .

Instead, looking at the residuals for the helium ions sample, the performances of the two methods seem more similar, and two distributions have only slight differences, with algorithm B producing a little more tighter residuals, despite a trace of a tail on the left.

Anyway, the performances of both methods seems really promising, at least for the data samples of interest, and the IP it is identified correctly and with sufficient precision in the majority of cases.

5.2 Particle identification

Once the interaction point has been identified, it is possible to extract a sample of energy deposits (dE/dx) generated by the ionization of the primary particle, (taking into account all the deposits upstream of the IP). Then the particle charge can be inferred from these sets of measurements, and the cosmic ray elemental species can be identified.

To separate between charges that differ by one or few units, two different methods have been studied and implemented. The first one uses the truncated mean of the energy losses to select the charge via some suitable cuts on this parameter. The other one is instead a natural extension of the method “B” for the IP measurement, and uses the probability that a certain dE/dx belongs to a specific charge to assess what kind of particle it is most likely that has crossed the detector planes. However, both of them can be applied irrespective of which algorithm is used for the IP reconstruction.

The data used for these studies are the same proton and helium samples already described, with the same event selection and limited to the interval from 100 GeV to 100 TeV. Furthermore, to have a better characterization of the detector performances, the data samples are divided into 12 (approximately) equally populated logarithmic bins in energy, and the analysis is carried out bin per bin.

5.2.1 The truncated mean method

The idea behind this method is to compute a proper average energy loss in order to deal with the fluctuations of a single dE/dx measurement. In fact it is known that energy losses follow a Landau distribution convoluted with a Gaussian, and this function is really asymmetric, especially for small charges, where the Landau contribution with its characteristic long right tail dominates.

For this reason, once the dE/dx sample is obtained, taking into account all the deposits ahead of the interaction point, an average energy loss is estimated computing a “truncated” mean. This means that the average is not computed over the whole sample of energy deposits, but only on a given percentage of the lower ones. This

percentage is known as truncation level. After a dedicated study, it was found to be optimal for the IMC detector to require a minimum sample of 4 points for the analysis, and to set the truncation level at 30%. This allows to reduce the Landau tail of the dE/dx distribution, without decreasing too much the efficiency for particle identification.

The effect of the 30% truncation on the mean can be seen in figure 5.3, where plot (a) shows the distribution of the mean energy deposit both for protons (red line) and for helium ions (blue line), while plot (b) is made from the same data sets, but using the truncated mean method. To ease the comparison, all the distributions are normalized to 1, and, as an example, both plots refer to a single energy bin in the range from 3.16 to 5.62 TeV. A similar behaviour is observed for the other bins.

It is clear that the truncated mean distributions are narrower and better separated

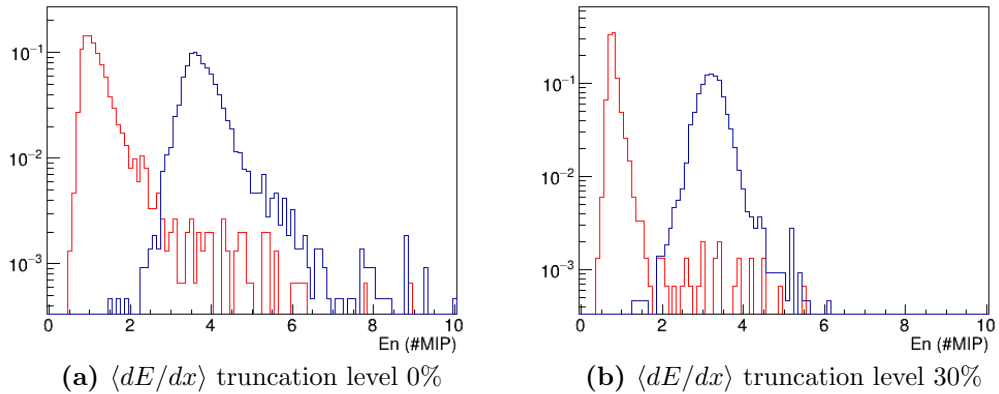


Figure 5.3: Distributions of the mean energy deposit without truncation (a) and with a truncation level of 30% (b), for protons (red line) and for helium nuclei (blue line).

with respect to the non truncated samples.

Once the truncated mean has been computed, the charge value is determined by cutting on the $\langle dE/dx \rangle$ distribution in a suitable way.

In figure 5.4 (a) and (c), the truncated mean distributions for protons (red line) and for helium ions (blue cross) are superimposed and properly normalized with respect to the expected relative abundances in CRs [92]. Both plots refer to the first energy bin from 100 to ~ 180 GeV, but the distributions in (a) are computed employing the method *A* for the IP reconstruction, while that in (c) are calculated

using the B method.

The particles charge is tagged starting from these distributions. In fact the events

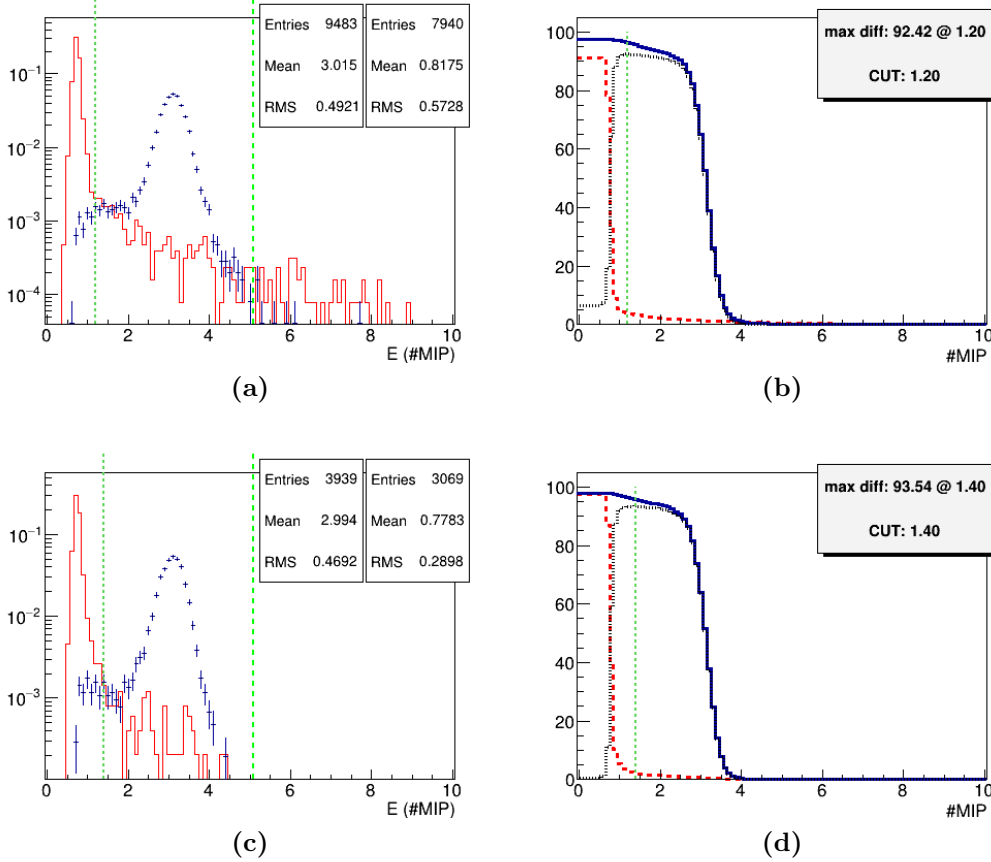


Figure 5.4: (a): $\langle dE/dx \rangle$ distribution both for protons (red line) and helium (blue cross), normalized with respect their relative CR abundances, and obtained starting from the IP reconstruction method A . (b): Helium efficiency (blue continuous line), proton contamination (red dashed line) and their difference (black dotted line) depending on the selection cut value, evaluated using the distributions of plot (a) not normalized. (c): The same distributions of plot (a) obtained using the IP reconstructed by method B . (d): Analogous to plot (b) but calculated on the distributions of plot (c) not normalized.

with a mean energy loss included between the lower energy threshold (0.2 MIP), and the first cut value (green dotted line in figure) are selected as protons, while if the $\langle dE/dx \rangle$ lies between that first and the second cut value (green dashed line) the particles are tagged as helium.

The first cut value corresponds to the chosen separation point between proton and helium distributions, while the second value represents the end point of the helium distribution. The end point is estimated by fitting the helium energy loss with a

convolution function of a Landau and a Gaussian, and taking the value for which the integral from 0 to the end point is 99% of the total. The separation cut instead is more difficult to estimate. To do this, we consider the helium events as signal and the proton ones as contamination, then the optimal separation cut is taken as the value that maximizes the difference between the helium signal and the proton contamination. This recipe seems to make sense, as the relative abundances of helium and protons in CRs are quite similar in bins of total energy, and thus in principle there is no reason to prefer a lower proton contamination going to the expense of the helium efficiency or vice versa.

In figure 5.4 (b) and (d) the helium efficiency is shown (blue continuous line) as a function of the cut value, together with the proton contamination (red dashed line) and the difference between signal and contamination (black dotted line). The difference between plot (b) and (d) is that they are calculated starting from the distributions (not normalized) of histogram (a) and (c), respectively. The blue line represents the percentage of reconstructed helium surviving the cut, calculated over the total number of events triggered and tracked by the detector. Inefficiencies arise both from the cut and the charge reconstruction procedure (e.g. due to early interacting events). The red line, instead, is the percentage of protons surviving the cuts and contaminating the helium signal. The optimal separation cut then corresponds to the maximum of the black line, as it is the difference between the blue and the red lines.

This analysis is performed for all the 12 energy bin in which the data samples are divided, and it is found that while the behaviour is similar for different bins, the optimal cuts vary from one bin to another. Clearly this dependence with energy must be taken into account to achieve the best performances in separating the protons and helium signals.

5.2.2 The probability method

The idea behind this second algorithm is to take advantage of the known energy loss distributions for the different charged particles, and use them to calculate which particle is most likely to have deposited the measured dE/dx ahead of the IP.

Operatively, the template distributions of the energy loss in each plane (already computed during the IP identification step), are used to calculate the probability that each energy deposit ahead of the IP belongs to a certain particle of charge Z . Then the average probability is computed and the procedure is repeated for each particle of interest. Finally the Z with associated the largest average probability is chosen as the charge of the incoming primary cosmic ray. This procedure is analogous to the one used in method B for IP reconstruction to chose the most probable charge, and in this case the particle identification can be considered a by-product of the IP detection. However also in the case where the IP is obtained with method A it is possible to apply this algorithm for charge tagging.

Also in this case, to have a reasonable sample of dE/dx it was decided to put a constraint on the minimum number of points before the IP, and in analogy with the previous algorithm it is chosen to be 4. With this method it is particularly easy to put some additional cut on the minimum of the mean probability to asses a charge tagging, in order to select a particle sample with higher purity. Anyway for the analysis described in this section the only cut applied is on the minimum number of points in the sample.

This charge identification algorithm was tested on the same proton and helium data samples already described above and divided into 12 logarithmic bins as well. The only charges taken into consideration are $Z = 1$ and $Z = 2$.

The algorithm is tested both in case of an IP reconstruction operated with method A and B , and some significant results are shown in figure 5.5 and 5.6 where the mean energy loss is presented together with the reconstructed particle charge for the proton and helium data samples, respectively.

In figure 5.5 (b) it is shown the Z reconstructed for the proton data sample, in an energy bin spanning between 3.16 to 5.62 TeV. This plot is made taking advantage of the IP identification by method A , and the underflow count indicates the events in which no charge is reconstructed, because there are too few points in the data sample (less than 4). From this plot we can infer that in the specified energy range the charge is reconstructed in about 70% of cases with the proton identified correctly about 99% of the times, while only in the $\sim 1\%$ of cases it is misclassified as helium.

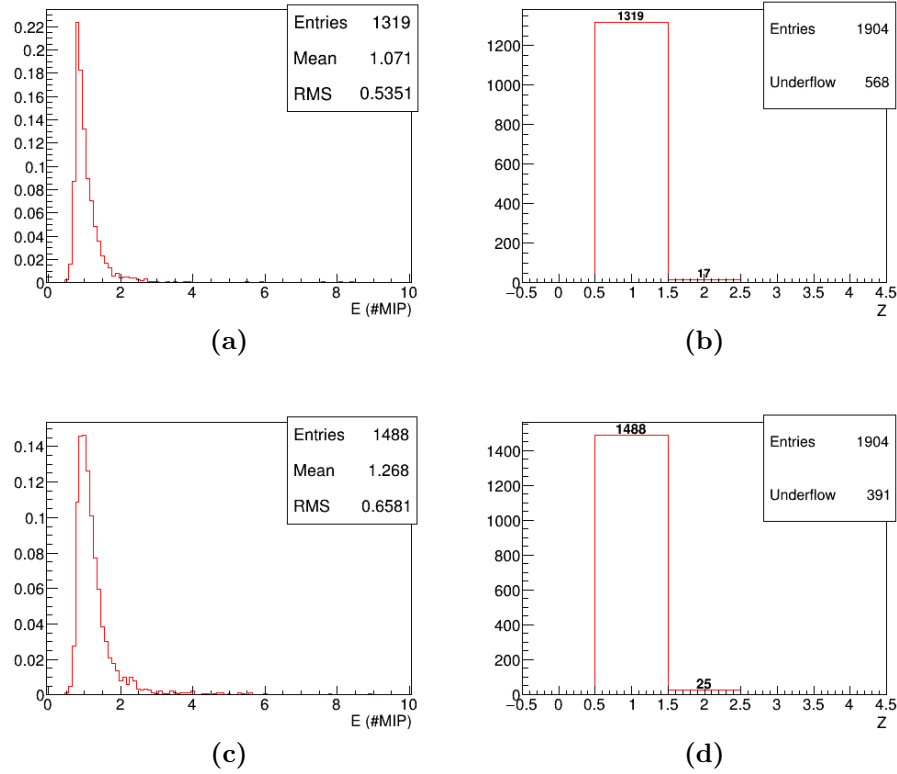


Figure 5.5: Some plots regarding the application of the “probability method” to the proton data sample in the energy bin from 3.16 to 5.62 TeV: (a) mean energy deposited before the interaction of a particle with reconstructed charge $Z = 1$, with the dE/dx sample obtained from method *A*, the distribution is normalized to 1; (b) reconstructed charge Z using the IP identification from method *A*; (c) mean energy deposited before the interaction of a particle with reconstructed charge $Z = 1$, where the dE/dx sample is obtained from method *B* and the distribution is normalized to 1; (d) reconstructed charge Z using the IP identification from method *B*;

In figure 5.5 (d) instead, the reconstructed charge is shown resulting from method *B* for IP detection. In this case it is possible to notice that the algorithm is capable to identify Z in about 79% of cases, and this time the charge tagging results correct in $\sim 98\%$ of events. The normalized mean energy loss distributions resulting from a proton tagging made respectively with the method shown in plot (b) and (d) are displayed in the histograms (a) and (b) of the same figure. The normalization constant is 1.

For the helium data sample, the test results are shown in figure 5.6, where in (b) there is the histogram of charge as reconstructed by the dE/dx sample obtained from method *A*, and in (d) there is the same plot but made using the method *B* to

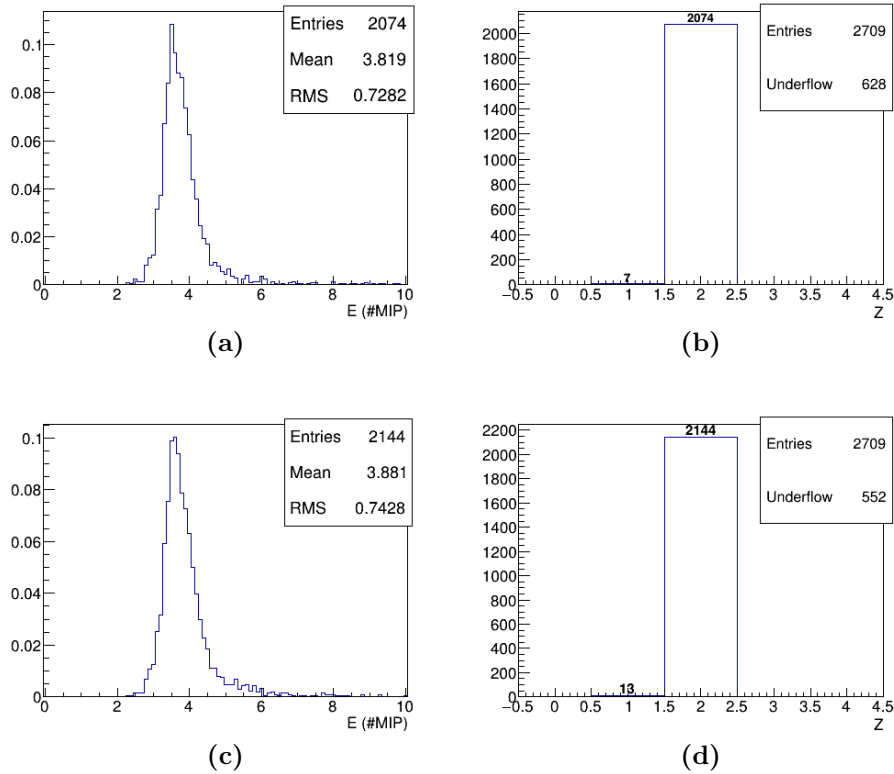


Figure 5.6: Some plots regarding the application of the “probability method” to the helium data sample in the energy bin from 3.16 to 5.62 TeV: (a) mean energy deposited before the interaction of a particle with reconstructed charge $Z = 2$, where the dE/dx sample is obtained from method *A* and the distribution is normalized to 1; (b) reconstructed charge Z made using the IP identification from method *A*; (c) mean energy deposited before the interaction of a particle with reconstructed charge $Z = 2$, where the dE/dx sample is obtained from method *B* and the distribution is normalized to 1; (d) reconstructed charge Z made using the IP identification from method *B*;

determine the IP.

In the first case no charge is tagged in $\sim 23\%$ of events, while for the remaining 77% the tagging works properly reconstructing correctly a $Z = 2$ particle more than 99% of the time, with a misclassification in $Z = 1$ less than the 0.5%. In the second case, instead, the percentage of events for which the charge is reconstructed is a bit better, about 80%, and the number of particles classified correctly as helium remains above the 99%. Also for helium ions, in figure 5.6 (a) and (b) the mean energy loss distributions are shown. These histograms are made using the IP identification methods *A* and *B* respectively, and requiring a reconstructed charge $Z = 2$. Both distributions are normalized to 1.

For brevity, in this section are displayed the results obtained only for one of the 12 energy bins in which the data samples are divided. The analysis has been performed concurrently for all the bins, and the algorithm seems to work reasonably well in the whole energy range, despite a dependence of the performances with the energy. As the charge tagging results more difficult at high energies, mainly due to the reconstruction efficiency, the discrimination capability between one charge and another remains remarkable.

The energy dependence of the algorithm will be addressed in more detail in section 5.3, where the overall performance of the IMC detector in proton-helium identification is discussed.

5.2.3 The log-likelihood ratio method

With greater statistical rigour, a way to use the information of the known energy loss distributions for different charged particles, is to apply a test of hypothesis, using the probability associated to each energy deposit to assess if the null hypothesis of a particle with charge Z is too unlikely to occur. Practically, to discriminate between $Z = 1$ and $Z = 2$ charges, the idea is to apply two separate Neyman-Pearson tests [93], (one on the helium hypothesis and the other on the proton hypothesis) using a Log-Likelihood ratio as statistics.

First, the probability for each energy deposit of the selected dE/dx sample is extracted exactly in the same way as described in the previous section. Then the log-likelihood is computed, summing up the negative logarithm of the probability for each plane, as shown by equation 5.1:

$$L(\underline{x}, Z) = \sum_i -\log P(x_i, Z). \quad (5.1)$$

Where i refers to the layer, x_i is the corresponding energy deposit and $P(x_i, Z)$ is the probability that the deposited energy x_i belongs to the charge Z . Then the log-likelihood ratio $\lambda = L(\underline{x}, Z_1)/L(\underline{x}, Z_0)$ is computed, where Z_0 represent the null hypothesis under test, and Z_1 is the alternative hypothesis. The critical region for the test is given by $0 < \lambda < \lambda_\alpha$ where λ_α depends on the chosen significance α , and

is computed from equation 5.2:

$$\alpha = \int_0^{\lambda_\alpha} g(\lambda, Z_0) d\lambda \quad (5.2)$$

where $g(\lambda, Z_0)$ is the p.d.f. of the log-likelihood ratio λ under the assumption that Z_0 is true, and is computed numerically from the Monte Carlo simulation.

Finally to quantify the evidence against the hypothesis that the incoming particle is a proton, a certain significance α is chosen, for example $\alpha = 0.05$, and a test with $Z_0 = 1$ and $Z_1 = 2$ is made. Instead, in the case where the hypothesis helium is under test, the procedure is repeated by exchanging the roles of Z_0 and Z_1 .

In figure 5.7 for example it is shown the histogram of $g(\lambda, Z_0)$ (left) together with

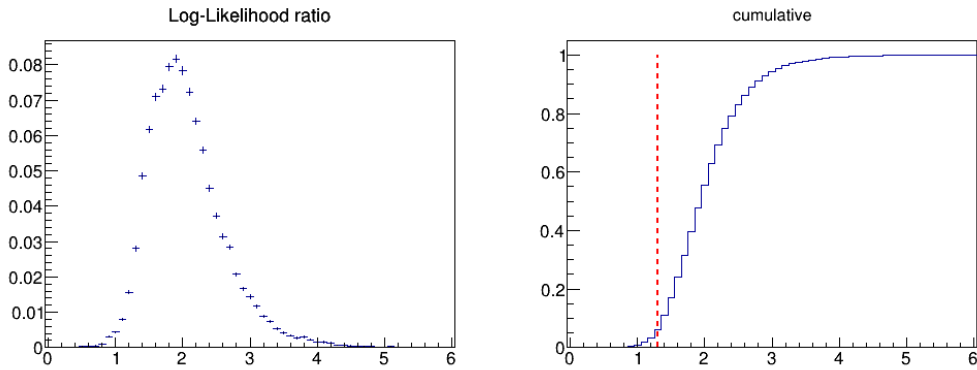


Figure 5.7: On the left it is shown the p.d.f. $g(\lambda, Z_0)$ under the assumption that Z_0 is true, for $Z_0 = 2$. On the right the cumulative distribution of $g(\lambda, Z_0)$ is shown, the red dashed line represents the value λ_α for a confidence level $\alpha = 0.05$.

its cumulative distribution (right), evaluated with the MC helium data sample, as it is needed to test the hypothesis $Z_0 = 2$. The red dashed line in the cumulative plot represents the value of λ_α for a confidence level α set to 0.05.

Despite the difficulty in extracting properly $g(\lambda, Z_0)$, this method has the advantage to make the analyser free of choosing the desired significance. Depending on the situation, even two different values of α can be used to tag proton and helium. Moreover it is possible to extend this approach to the case where more than two possibilities are under test, or in other words the test moves from the case of a simple hypothesis to a composite one. In this case, the likelihood of the alternative hypotheses will be computed as the maximum value over the parameter space, by

performing an actual likelihood-ratio test. However, the very low abundance of lithium ($Z = 3$) in the CR flux, allows – at least as a first approximation – to limit our statistical treatment to the test of a simple hypothesis.

5.3 Performance of helium-proton discrimination

In this section it is presented a summary on the performances of the IMC detector for proton and helium selections with the different algorithms already described.

In particular, for each energy bin the signal detection efficiency, contamination and purity are calculated, considering helium and proton as the only species of interest. For example, if helium is assumed to be the “signal”, the efficiency is represented by the fraction of helium events reconstructed correctly with $Z = 2$ with respect to the total number of signal events under analysis. The contamination is the part of non-signal events misclassified as helium. The signal purity is defined as the number of helium nuclei correctly identified with respect to the sum of He nuclei plus proton contamination (computed taking into account their relative abundances). Clearly this definition of purity is not completely exhaustive, but as far as protons are the main contaminant for helium measurement, it makes sense. Obviously the same definitions hold when the protons are the signal we are looking for in our analysis. In the following we summarize the bin per bin performances of the IMC in helium-proton identification, depending on the algorithm employed for IP identification and charge tagging.

In figure 5.8 the results are shown for the case where the log-likelihood ratio method is used for charge identification, taking advantage of the IP reconstruction made with algorithm *A*. The efficiencies are illustrated as a blue continuous line, while purities are the green dotted lines and contaminations the red dashed ones. The plot on the left refers to the helium signal, while the plot on the right refers to protons. In this case, the hypothesis test is made only on the truncated sample of dE/dX (at 30% as usual), and the significance is set to $\alpha = 0.05$ for both species. Anyway it is possible to choose an higher α for helium in order to have a more tight selection, and a lower significance for protons to obtain a larger efficiency.

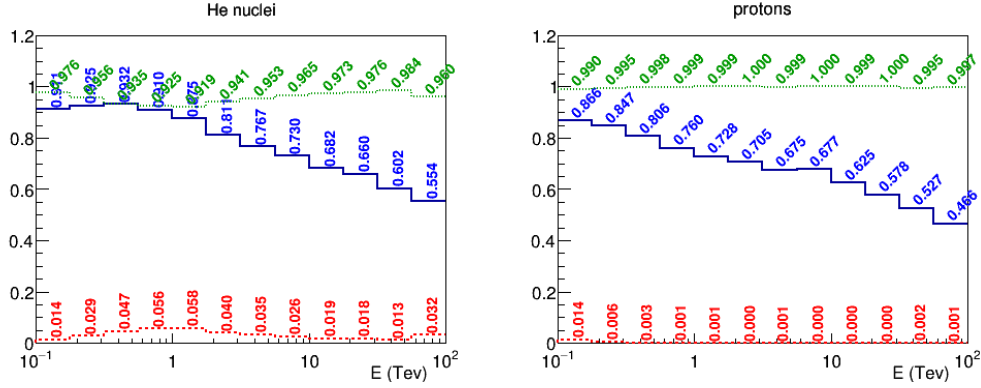


Figure 5.8: Efficiency (blue continuous line), contamination (red dashed line) and purity (green dotted line) of helium (left) and proton signals (right) as a function of energy bin. Algorithm *A* for the IP reconstruction is used, together with the log-likelihood ratio method for charge tagging.

In figure 5.9 the efficiencies, contaminations, and purity are shown both for helium (top left, bottom left), and for proton signal (top right, bottom right). All the four plots are made using the method *A* for the IP detection, but the two histograms on the top show the results when the charge is identified via the *truncated mean* algorithm, while the plots on the bottom refer to the output of the *probability method*. In figure 5.10 instead, the same quantities are shown as obtained with method *B* for IP identification. Once again the plots on the top show the results for the charge tagging of *truncated mean* algorithm and the ones on the bottom for the *probability method*. On the left side there are shown the histograms for helium signal, while on the right the results for protons.

Figure 5.8, 5.9 and 5.10 represent an overview of what is possible to obtain applying the developed algorithms for particle identification in the IMC, without any additional cut.

It can be noticed that the different combinations of algorithms for IP detection and charge tagging, lead to comparable results, except for the configuration shown at the bottom of figure 5.9 that exhibits a larger contamination of the signal both for helium and for proton. In the other cases not only the performances, but also the behaviours of the alternative methods are similar. In particular, the signal efficiency tends to decrease at higher energies both for helium and for proton, while in some cases (with the exception of figure 5.9 bottom) the contamination shows a maxi-

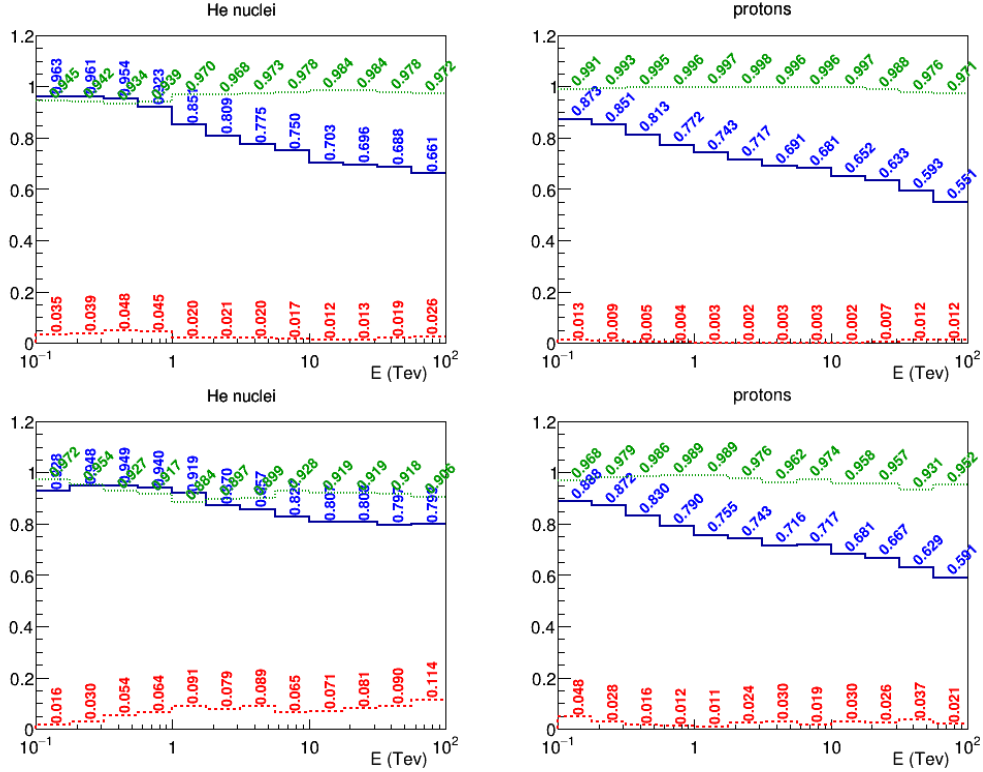


Figure 5.9: Efficiency (blue continuous line), contamination (red dashed line) and purity (green dotted line) of helium (left) and proton signals (right) as a function of energy. Method A for the IP reconstruction is used, together with the *truncated mean* algorithm (top) or the *probability method* (bottom) for charge tagging.

imum (around 400-700 GeV for helium and 100 GeV for protons) and then decreases till about 20–30 TeV before starting to rise again. The maximum contamination is around 5-6%, while the efficiency is in general above 50-60%, and the purity is always above 92%.

These results seem a reasonably good starting point, especially because the IMC was not designed for charge measurements, but mainly for tracking and topological selection purposes. Anyway something must be made to improve the overall performances, especially for what concerns the contamination, which is still quite high. The major source of this contamination has been discovered to originate from the particles interacting in the CHD, and in the first layer of the IMC, since these kind of events can “simulate” the dE/dx of a different nuclear species inside the IMC, deteriorating the measurement.

The importance of this issue can be observed in figure 5.11 where the events interacting above the IMC are excluded from the analysis. The histograms on the

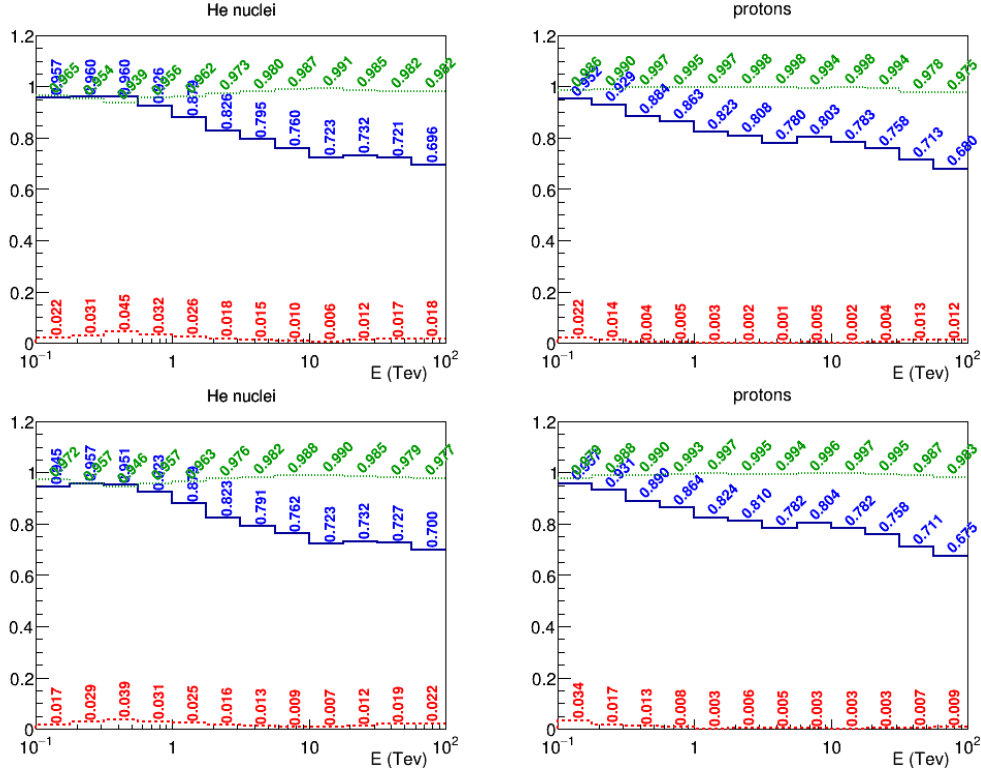


Figure 5.10: Efficiency (blue continuous line), contamination (red dashed line) and purity (green dotted line) of helium (left) and proton signals (right) as a function of the energy. Method *B* for the IP reconstruction is used, together with the *truncated mean* algorithm (top) or the *probability method* (bottom) for charge tagging.

top side reproduce the same condition of the top of figure 5.9, while that on the bottom are analogous to the plot of figure 5.10 (bottom side). It is important to notice that under this assumption the contamination is greatly reduced, at least in the low energy bins. This means that, as expected, this type of error in the charge identification arises from events interacting upstream of the IMC, and thus it is not possible to “recover” this contamination improving the algorithm, but it is only possible to exclude this kind of events from the analysis.

The contamination in the higher energy bins, probably comes from tracking, as the higher track multiplicity for this kind of events makes it difficult to resolve single particle tracks and to recognize correctly the primary one. Really similar results hold also for the other algorithm configurations. They are not shown here.

When the charge assignment is performed using the *probability method* it returns a suitable variable to perform a cut in order to reduce the contamination. In figure 5.12 this additional cut on the mean probability (see previous section) is made, both

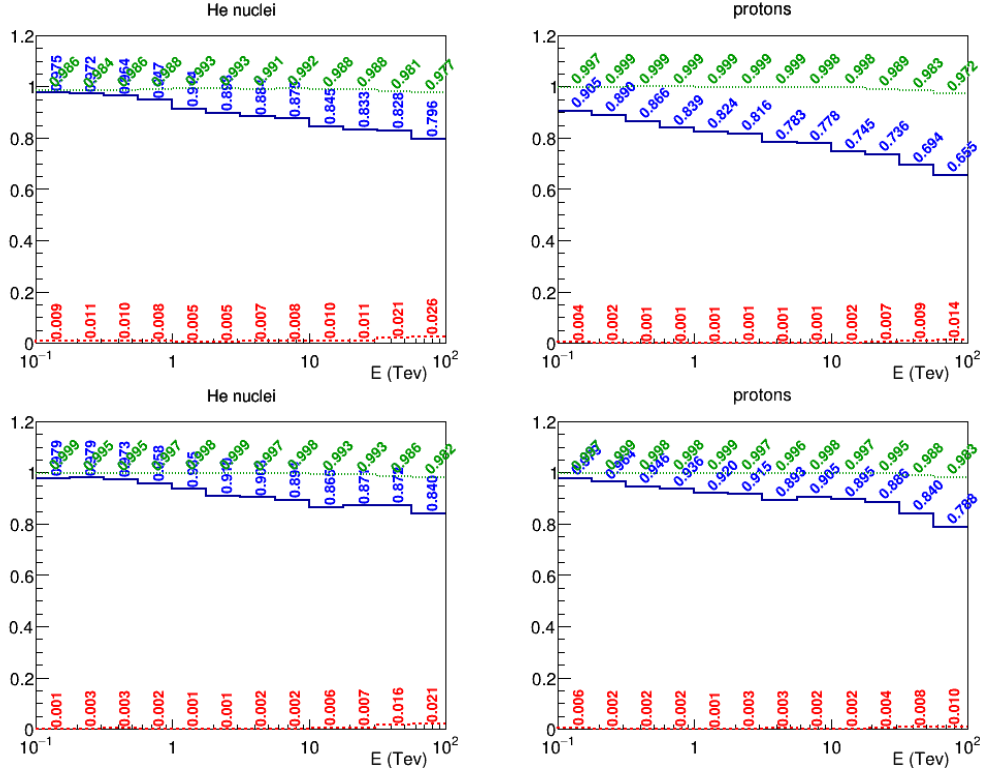


Figure 5.11: Efficiency (blue continuous line), contamination (red dashed line) and purity (green dotted line) of helium (left) and proton signals (right) as a function of energy. On the top, method *A* for the IP reconstruction it is used, together with the *truncated mean* algorithm. On the bottom instead, the method *B* for the IP, and the *probability method* for charge tagging are used. All the events interacting upstream of the IMC are excluded from these plots.

in the case of the IP reconstruction with method *A* (top) and *B* (bottom).

To have an idea of how much this cut can be effective, the top histograms of this figure have to be compared with that at bottom of figure 5.9, that refers the same analysis but without the mean probability cut. From this comparison it seems evident that a remarkable improvement is obtained in that case, as both for helium (left) and for protons (right) the contamination is greatly reduced, with a noticeable enhancement of the signal purity. Furthermore, the performance of this algorithm configuration (method *A* for IP and “probability” for charge tagging), that was by far the worse, are now comparable and even better than that of the other configurations without cuts.

The other two analyses to be compared are those shown at the bottom of figures 5.12 and 5.10, where the differences are again made only by application of the cuts. From

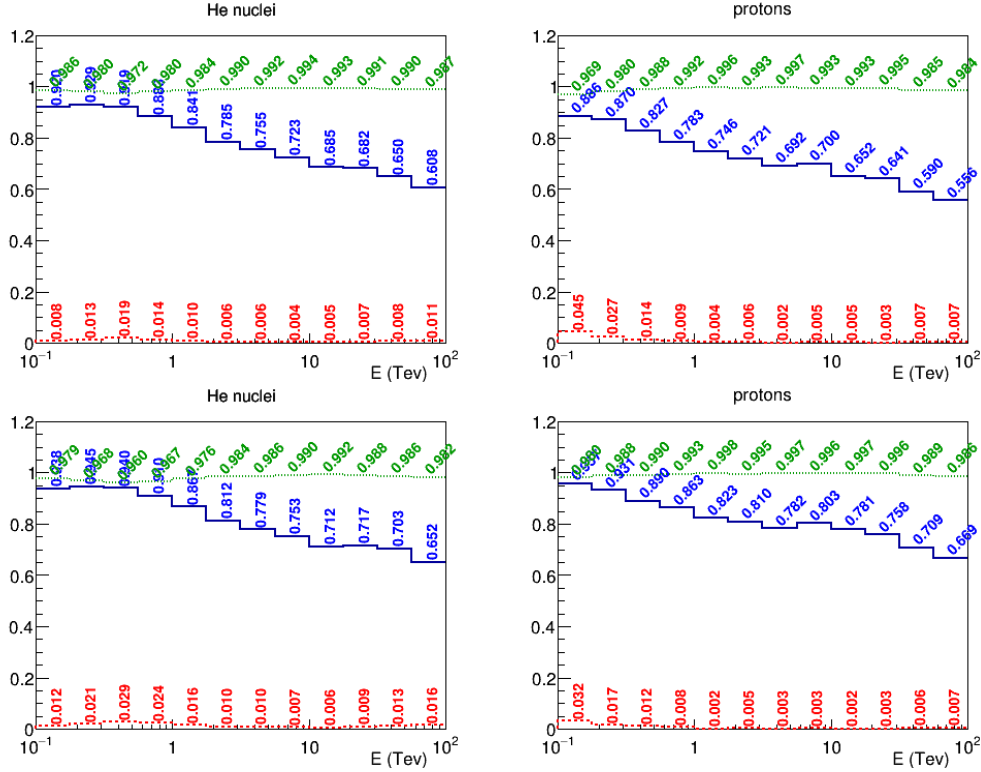


Figure 5.12: Efficiency (blue continuous line), contamination (red dashed line) and purity (green dotted line) of helium (left) and proton signals (right) as a function of energy. The *probability method* is used for charge tagging, together with different methods for the IP reconstruction: *A* (top) and *B* (bottom). A cut on the mean probability is applied in all cases, with the requirement to be greater than 0.015.

this comparison it follows that also in this case the additional cut helps in removing part of the contamination, though less effectively than in the previous case.

These plots are not directly comparable with the ones on the bottom side of figure 5.11, as in this case the events that do not survive the cut are excluded from the analysis (and thus from efficiency and contamination), whereas in figure 5.12 they are treated as non reconstructed, thus affecting efficiency and contamination.

This simple cut on the mean probability does not solve completely the problem of contamination. A possible solution is to made the cut tighter, but at the expense of the efficiency, especially at the highest energies. For this reason a convenient compromise must be found in agreement with the analysis requirements.

Clearly there are other variables that can be used when the charge tagging is made with the *truncated mean* algorithm, or also in addition to the mean probability cut. A preliminary study in this direction has been performed, and some

variables like the energy spread, (defined as the mean energy per fiber in a cluster), or the mean number of fibers per cluster have been found to be effective for this purpose. But none of them is found to be resolute. The effect of a cut on these variables, for a charge identification that uses method *A* together with the *truncated mean*, is comparable to what shown in figure 5.12, and even slightly better for the contamination, but the efficiency results are worse.

In conclusion, all the described methods seems to produce quite good results, given the characteristics of the detector, but none of them is optimal, and all have to handle with the issue of particle interactions upstream the IMC.

This study seems really promising, but they point at a combined use of the IMC detector with the CHD, to perform an accurate measurement of the proton and helium fluxes.

5.4 Helium-proton discrimination combining IMC and CHD information

Since the CALET telescope has a dedicated charge detector, it is really interesting to perform a charge tagging with IMC and CHD together, to find out to what extent a combined measurement can improve the overall performances, and in particular can reduce the signal contamination.

Clearly the two detectors information can be combined in many ways, but three main approaches are possible. The first consists of adding together the CHD and IMC dE/dx samples, applying some sort of “normalization” to link conveniently the different responses of the two detectors. Alternatively, two independent charge taggings can be made separately with the two detectors, requiring in a second stage consistency between the results. Finally, a third possibility it is to use one detector to perform a preliminary charge tagging, and the other one to refine the measurement enhancing the signal purity.

For a first study the third approach has been adopted, as it seems easier to apply, and less risky for the control of the systematics with respect to the first method, and

more effective than the second one. Operatively there is no great difference between the second and the third approach. Both of them require a separate selection of events in the two independent detectors, concurring to the charge identification. Applying a more stringent selection with one detector and using the other one only as a “supplementary check”, allows to achieve a good purity without losing too much efficiency. Of course, requiring stringent selection criteria with both detector leads to a greater reduction of efficiency.

In this analysis, the IMC is used for a preliminary charge tagging, because, due to its fine segmentation, it is less affected by back propagating albedo particles, therefore allowing for a better charge separation at high energies.

To have an idea of the differences between the CHD and the IMC behaviour when

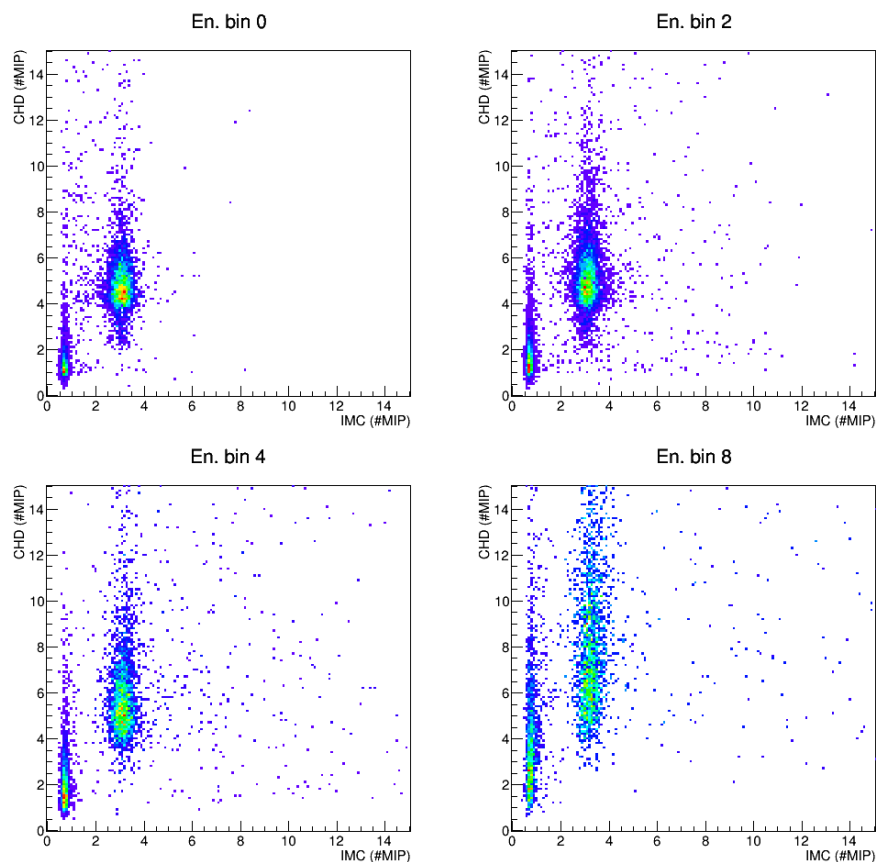


Figure 5.13: Superimposed correlation plots of the mean energy deposited in the CHD versus the IMC truncated mean energy loss for protons and helium nuclei in four different energy bins. The bin energy range is $[100, 178]$ GeV, $[316, 562]$ GeV, $[1, 1.78]$ TeV and $[10, 17.8]$ TeV, for bin 0 (top left), bin 2 (top right), bin 4 (bottom left) and bin 8 (bottom right) respectively.

the energy increases, in figure 5.13 the mean energy deposited in the CHD layers is plotted versus the IMC truncated mean energy loss, both for protons and helium nuclei, for four energy bins. For each bin the proton and helium signal are superimposed in the same plot, showing two separated clusters of events, with the one nearest to the origin representing the proton signal and the other one the helium signal. The four bins of interest are number 0 (top left), 2 (top right), 4 (bottom left) and 8 (bottom right), spanning respectively the energy ranges [100, 178] GeV, [316, 562] GeV, [1, 1.78] TeV and [10, 17.8] TeV. Looking at the less energetic bin (top left in figure 5.13) it is possible to notice that the clusters corresponding to helium and proton energy deposits are well separated, both with the CHD (y axis) and the IMC (x axis), despite the prominent tails for the CHD deposits, that are greatly reduced in the IMC measurement thanks to the truncated mean. Moving toward higher energies, it is evident that the proton and helium clusters remain well separated in the IMC measurements, while stretching more and more along the CHD axis. Already in bin 4 (bottom left) the two clusters start to overlap (in y) and in the last bin (bottom right) they are partially overlapped. This confirms that the CHD alone cannot be used to separate efficiently the two species at the highest energies, but anyway it remains a very important tool to reduce the signal contamination in the charge measurements, as it is shown in the following.

The adopted charge identification algorithm (shown on the upper two plots of figure 5.12), seems a bit more effective (at least for helium) with respect to the others. It consists of method *A* for the IP detection, plus the *probability method* for charge reconstruction with its additional cut on the mean probability value.

Then, on the preliminary proton and helium samples identified by the IMC, a second selection is made in the bi-dimensional scatter plot of the energy loss in the first CHD layer vs. the second one (y versus x). This selection consists in choosing only the events that fall in a certain region of the plane, excluding the others. This region is chosen conveniently bin per bin, depending on which species is tagged by the preliminary IMC measurement.

For protons, only events that satisfy the relation $E_y \leq aE_x + b$ are selected, while for helium the conditions that must be fulfilled simultaneously are $E_x \leq c$ and

$E_y \leq a_1 E_x + b_1$. Where E_x and E_y represent the energy losses in the CHD layers, and a , b , c , a_1 , b_1 are parameters that vary from one energy bin to another (typical values are $a = -3$, $b = [15, 50]$, $c = 3.4$, $a_1 = -2$, $b_1 = [30, 160]$).

This additional CHD selection allows to have a significant improvement in reducing the contamination, as it is shown in figure 5.14, where it is possible to observe the signal efficiency (blue continuous line), purity (green dotted line) and contamination (red dashed line) resulting from this combined analysis.

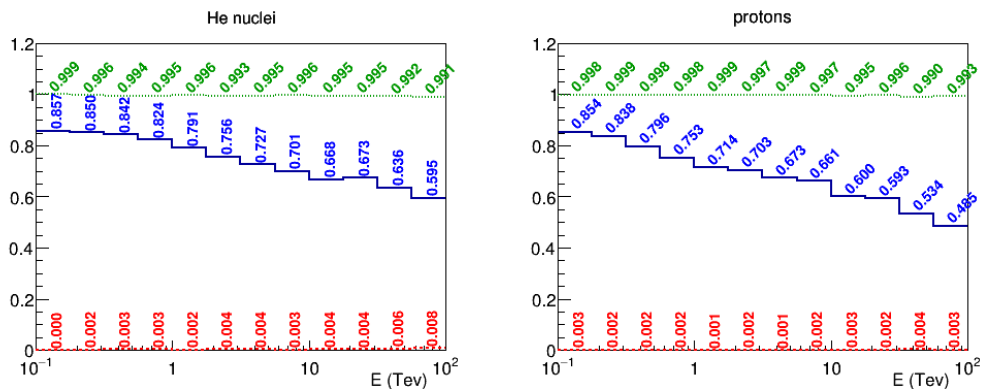


Figure 5.14: Efficiency (blue continuous line), contamination (red dashed line) and purity (green dotted line) of helium (left) and proton signals (right) as a function of energy. The results are obtained exploiting the combined information of the CHD and IMC detectors.

The plot on the left side shows the performances when helium is taken as signal, while the one on the right displays the same information for protons.

The improvement in the signal purity, always above the 99%, is evident if compared with the case in which only the IMC is used for the charge tagging (figure 5.12 top side). The reduction of contamination, now in the order of a few 1‰, is achieved without a significant loose of efficiency. Nevertheless it is clear that a certain amount of efficiency is lost, especially for protons at high energies. The trade-off between purity and efficiency, can be optimized according to the selection needs. For instance, a high purity sample from the CHD (at low efficiency) can be useful to measure the IMC identification with flight data and vice versa.

5.5 Performances of charge tagging with test beam data

As all the previously described studies on charge identification have been made with FLUKA Monte Carlo data. It is of particular interest to “validate” the developed algorithms also in case of real data. For this reason, several different methods available for charge tagging have applied to beam test data, both for protons and helium, and their performances are reported in this section.

The beam test data set consists of two samples, one taken with 400 GeV protons and a second one with argon fragments at 150 GeV/n, that were recorded during two dedicated beam tests at CERN (SPS extracted beams), respectively in 2012 (TB2012) and 2015 (TB2015).

Clearly, before proceed with the analysis, a preliminary alignment and calibration of the TB data is mandatory. For the 400 GeV proton sample the same calibration and alignment parameters described in section 4.3.2 were used, as these data were taken in the same configuration of that used for the tracking validation. For the TB2015 data instead, collected at a different beam test and with a different detector configuration, these preliminary procedures had to be repeated. The alignment is performed using the same χ^2 minimization method described in section 4.3.2, and the channel-by-channel calibration is carried out in a similar way, normalizing each fiber to the MIP. The main difference with respect to the procedures adopted for TB2012 is that during the TB2015 neither muon samples, nor proton samples were available to perform the alignment and calibration. For this reason these procedures were carried out on a selection of non interacting helium ions, extracted from the argon fragments data, via a really tight cut on the energy losses in the CHD and in the last layers of the IMC.

For the 2015 ion beam test data, the energy deposits in the CHD paddles are calibrated in Z , and then a cut on the correlation plot between the x and y hit paddles of the CHD is performed. This plot is shown in figure 5.15, with the relative cut, that is represented by the red dashed square. The events inside this square are selected as the helium ions sample for further analysis.

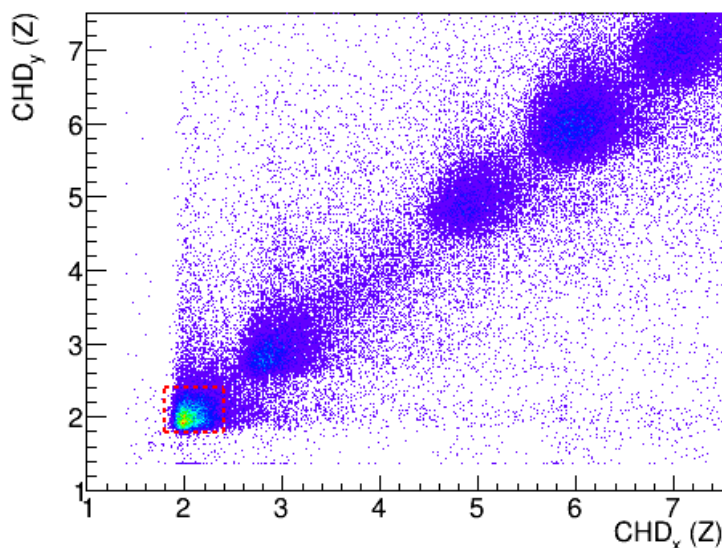


Figure 5.15: Correlation plot of the charge measured, from the ionization energy losses, by the hit paddles of the CHD y and x layers. The events inside the red dashed square are selected as helium ions sample for further analysis.

Once all these preliminary procedures have been accomplished, the charge reconstruction algorithms are applied to both the helium and proton data samples. The algorithm adopted are exactly the same used for MC data and no particular tuning are made for this analysis. Also the approximated straggling function used in some steps are the same. This means that they are extracted from MC data and not directly on TB samples, but even if the MC templates are a bit more tight compared to the TB ones, the charge reconstruction performance remains remarkable, as it is possible to see in figure 5.16. where the distributions of the reconstructed charge by the different algorithms developed for this analysis are shown. Each one of the four plots represents the result of one method, both for the proton (red line) and for the helium sample (blue line), with two superimposed histograms. These histograms have only three allowed values for the reconstructed charge 1, 2 and -1, where the bin centred in -1 represents the condition in which no charge is reconstructed. This means that the analysed event does not survive one of the cuts applied, or, in case of the *truncated mean* method, simply that the $\langle dE/dx \rangle$ is outside the charge selection regions. The bin content is expressed not in counts but in percentage with respect to the total number of analysed events.

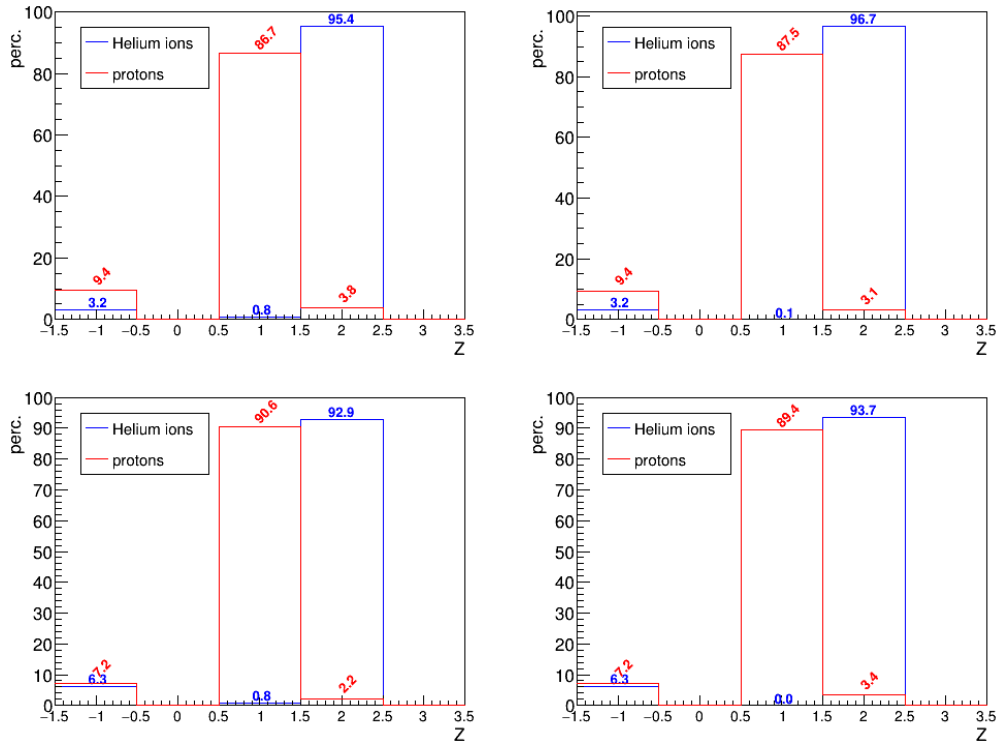


Figure 5.16: Reconstructed charge for the proton (red) and helium (blue) TB samples, as obtained by four different algorithms developed. The bin contents are expressed in percentage with respect to the total number of analysed events, and a reconstructed value of $Z = -1$ indicates that no charge is identified for a certain event. The IP is detected via method *A* in the top side plots, and *B* in the bottom ones, while the plots on the left uses the *truncated mean* for charge tagging instead of the *probability method* adopted for the right side plots.

The plot displacements inside the figure denote the different algorithms used to produce them. In fact, the Interaction Point reconstruction is made with method *A* for the plots on the top side of the figure and method *B* for those on the bottom, while the *truncated mean* is used for charge classification in the plot on the left, and the *probability method* is applied on the right side.

Clearly in this case it is not easy to link together the results of the proton and helium samples, because the data are taken under different detector configurations and different energies. From this follows also that to select the charge with the *truncated mean* method the choice of the separation cut value cannot be optimized in the same way as described in section 5.2.1. It is fixed quite arbitrarily to 2 MIPs, on the basis of a simple comparison of the truncated mean distributions, shown in figure 5.17. On the other hand, the end point of the helium distribution is taken

directly from the MC calculation.

Figure 5.17 shows the distributions of the truncated mean of the energy deposits, both for helium (blue cross) and for proton (red line), for the four different possible cases. Also in this case, the different plots inside the figure refer to different methods used for this study, and their displacements are the same of figure 5.16. For a better comparison, all the distributions are normalized to 1.

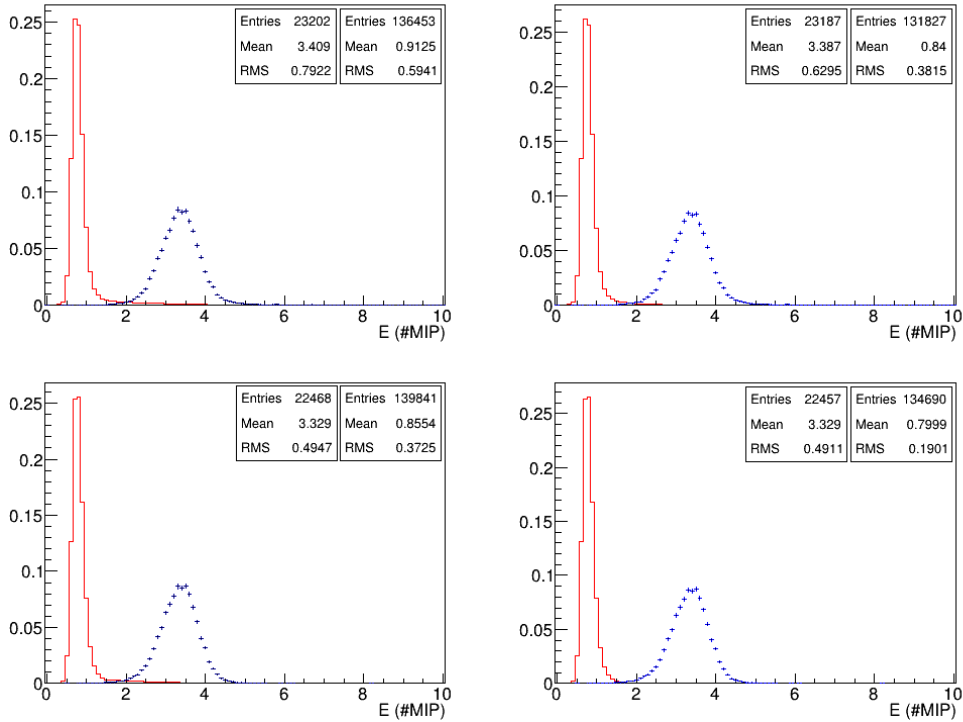


Figure 5.17: Distributions of the truncated mean of the energy deposits, both for protons (red line) and helium ions (blue cross). The truncation level is set to 30%, and all the distribution are normalized to 1. The four plots refers to different algorithms for charge tagging and IP reconstruction.

In conclusion, from figure 5.16 it follows that for test beam data not only the charge tagging performances are very good for all the developed algorithms, but even comparable with those expected from the analysis of MC data.

The different methods have similar performances, with a percentage of charge identified properly for protons varying from about 87% to 91%, and rising to about 93% to 97% for helium. The misidentified events are less than 1% for helium nuclei, and of the order of 2–4% for protons.

Chapter 6

The Proton and Helium fluxes measurement

Protons and helium nuclei are by far the most abundant components of CRs, as they amount, respectively, to $\sim 89\%$ and 10% of the hadronic part of the cosmic radiation. Due to their relatively high abundance they are clearly the easiest nuclei to be observed, and a precise measure of their fluxes can provide important information to understand cosmic rays.

In particular, a search for any significant deviation from a single power law and possible cut-offs (at high energies) in the spectra of individual elements, as predicted by models of diffusive shock acceleration in SuperNovae Remnants (SNRs), would be very significant to clarify the acceleration mechanism. Moreover, at low energies, these data are important to study the CR interactions with the interstellar medium, the heliosphere and the magnetosphere.

This chapter contains a brief excursus on the helium and proton flux measurements. The past and the more recent observations of the spectra are discussed, as well as the perspectives of the CALET experiment to perform new measurements from a few tens of GeV to unprecedented very high energies in the multi TeV region.

6.1 Brief overview of proton and helium spectra

The study of the proton and helium fluxes (and of heavier charged cosmic rays) can give an important hint to the understanding of their acceleration mechanism and propagation in the ISM and possibly a clue to infer the shape of their original spectra at the sources.

For example some theoretical models link the “knee”, observed in the CRs flux at an energy of about 10^{15} eV, to the acceleration process of charged particles. In particular, the theory of diffusive shock acceleration by SNR predicts the existence of a “maximum energy”, above which the acceleration process becomes inefficient. In this scenario, each element would exhibit a spectral cut-off at a characteristic energy, which would depend linearly on the charge (i.e. the atomic number Z). This means that in the inclusive spectrum the knee is the result of the change in CRs composition depending on the energy per nucleon, and in particular of the predicted (according to some models) depletion of light elements in the PeV region. For this reason the measurement of such a cut-off in proton and/or helium spectra could provide important insights into the nature and origin of CRs.

Many experiments, like CREAM, PAMELA and AMS, have not observed yet any cut-off below 100 TeV, as it is shown in figure 1.4. However, the predicted position of the cut-off for the light elements (p, He) varies really much according to different models, spanning over a wide range, from about 100 TeV [30] up to 1000 TeV and above [17, 31].

In this perspective, it is very important to extend the search of this hypothesized cut-off in the CRs nuclei flux at higher energies, taking advantage of CALET capabilities and of other direct experiments planned in the near future, like DAMPE and ISS-CREAM.

Moreover, recently developed non-linear acceleration models have been introduced to solve some difficulties of the SNR shock framework, as it predicts a maximum acceleration value too low with respect to the observations. These new models hypothesize that the structure of the shock front is modified by the accelerated particles, due to the pressure they exert on the plasma, leading to the phenomenon of

amplification of the magnetic field in proximity of the acceleration region [94]. In this scheme, the predicted energy spectra are no longer compatible with a single power law, but exhibit a concavity when plotted against a log energy scale.

Therefore, the identification of a significant deviation from a single power law in the spectra of individual elements, as suggested by CREAM [101] data and measured precisely by experiments like PAMELA [95] and AMS-02 [65,96], is a very significant result.

At the present time, experiments to measure the chemical composition and the spectra of CRs, including the proton and helium fluxes, can be divided in two categories: direct measurements and indirect ones. The former are performed both in space, with satellites or aboard the ISS, and in the upper atmosphere with long duration balloon flight missions. The latter, instead, are carried out with ground based experiments, where the nature of the primary nucleus is inferred indirectly, studying the secondary products of its interaction with the atmosphere. Up to now, ground experiments have dominated the scene at very high energies, in the region of 100 TeV and more, while present space-borne and balloon experiments can explore prevalently lower energies below the PeV scale.

Ground experiments are usually composed of array of detectors (often scintillators) arranged in such a way to cover a wide surface, and designed to measure, at ground level, the shower of secondary charged particles produced in the atmosphere, when a primary cosmic ray undergoes an electromagnetic or hadronic interaction. The measurement of the density of charged particles in each detector (prevalently electrons, positrons and muons), allows to infer the lateral distribution of the electromagnetic component of the shower, and yields information on the position of the core and on the total number of secondary particles produced. Moreover, the orientation of the shower can be reconstructed measuring the different arrival times of the particles in the several detectors of the array, and additional information on the secondary particles cascade can be provided by supplementary detectors, like imaging telescopes for fluorescent light measurements. From all these information, using some interaction model, like for instance QGSJET or SYBILL, it is then possible to

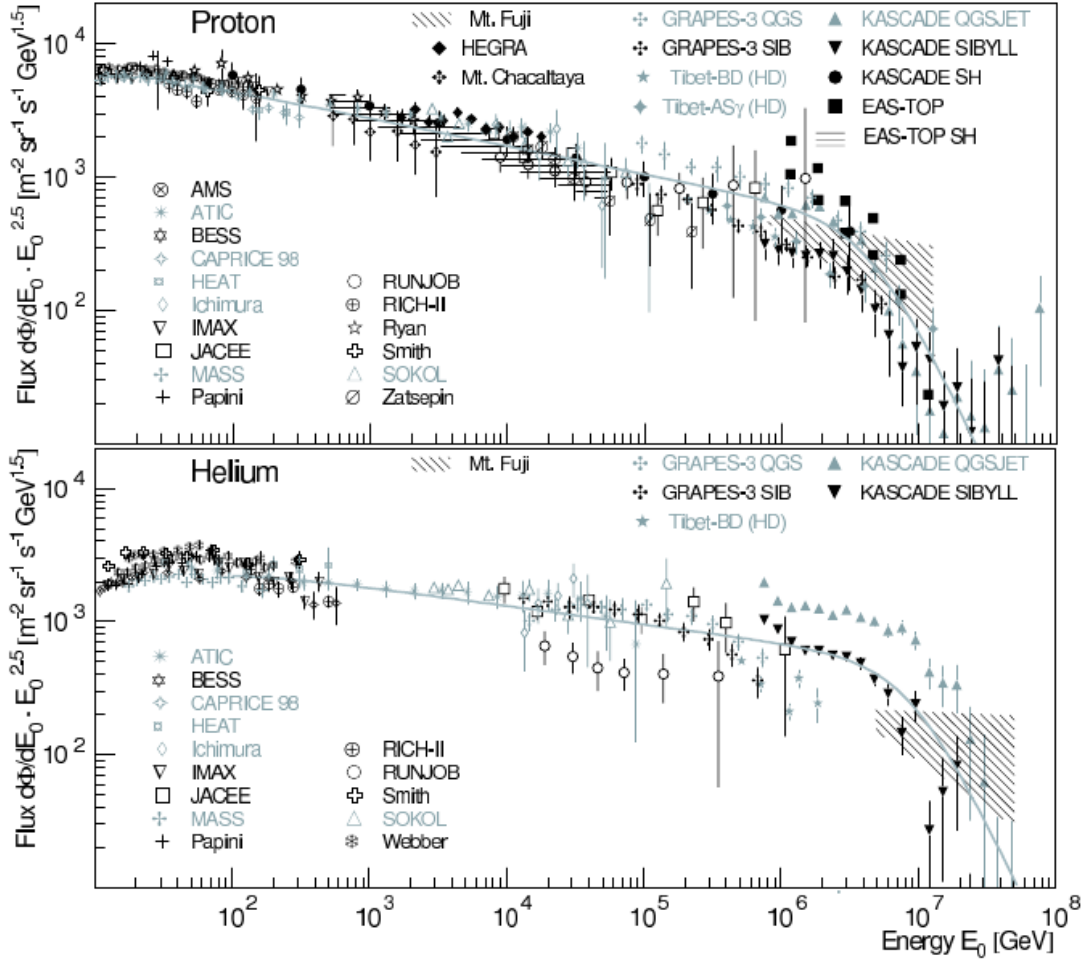


Figure 6.1: A compilation of proton and helium fluxes from ground based experiments. Results from balloon flights and space missions are reported as well [97].

reconstruct the primary CRs energy, direction and nature.

Other important ground based detectors include Cherenkov telescopes, or array of telescopes, that are designed to measure the Cherenkov light produced by the developing shower in the atmosphere, leading to the reconstruction of the primary information.

In figure 6.1 it is illustrated a collection [97] of recent results from ground based experiments on proton and helium fluxes measurements at very high energies. An ensemble of observations at lower energies by balloon and space based experiments is shown as well. For what concerns air shower experiments, some of the main results shown in the figure 6.1 are from detector arrays based on scintillators like KASCADE and GRAPES-3, or on Cherenkov light detectors as EAS-TOP, capable to

provide data up to the knee region. Moreover, other experiments like HEGRA and H.E.S.S (whose results are not shown in the figure), make use of imaging Cerenkov telescope systems, while the Tibet group uses a burst detector as well as emulsion chambers and scintillators arrays.

Looking again at figure 6.1, EAS-TOP results for protons are compatible with a single power-law from 0.5 TeV up to about 500 TeV. The KASCADE experiment, despite the well-known differences between the predictions of the QGSJET and SYBILL models, shows a gradual decrease of proton and helium fluxes in the knee region, with a significant deviation from a single power law around 4-5 PeV for protons. The TIBET-AS γ results [98] for protons between 5×10^{14} and 10^{16} eV exhibit a 3.1 ± 0.1 spectral index, compatible with a broken power law with $\Delta\gamma \sim 0.4$ and a knee around 700 TeV.

In summary, the current situation of the flux measurements of individual elements in the knee region is still unclear, due to the large model dependence used in the analysis of the data from indirect measurements. Even if there are convincing evidence of a depletion of the light component of nuclei above the knee, the discrepancies between different experiments like KASCADE and TIBET-AS γ leave open the question of an accurate determination of the “knee” energy for individual elements. The CALET mission will provide an unprecedented possibility to further investigate these questions with new input from direct measurements.

Space based missions and balloon flights are the only techniques capable to measure directly CRs energy and their chemical composition. Several detectors have been employed for this purpose, depending on the energy region under investigation. Usually, solid-state detectors are used up to hundreds of MeV/n and Cerenkov detectors up to few GeV/n, while magnetic spectrometers actually span over an energy range from few GeV/n up to few TeV/n. For higher energies (up to some hundreds of TeV), instead, nuclear emulsions, calorimeters and transition radiation detectors are most commonly used.

Up to now the highest energy for proton and helium data were collected in the 1990s by the balloon borne experiments RUNJOB and JACEE, that employed traditional detection techniques based on emulsions. However, their results are affected by large

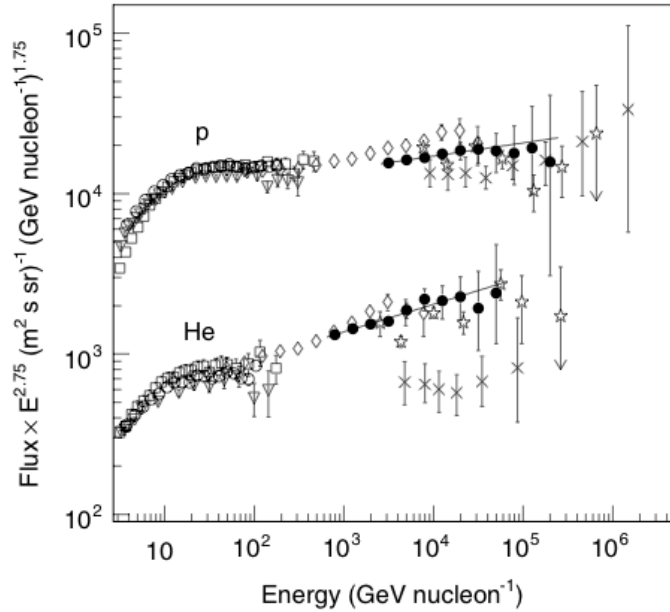


Figure 6.2: The CREAM proton and helium spectra (filled circles) together with a compilation of previous measurements: BESS (squares), CAPRICE98 (downward triangles) [104], AMS-01 (open circles), ATIC-2 (diamonds) [105], JACEE (stars), and RUNJOB (crosses). The CREAM data are fitted with power laws (solid line) with spectral index -2.66 for protons and -2.58 for helium nuclei [101].

errors and inconsistent with each other. The JACEE data [99] suggested that the proton spectrum is steeper than the helium one, but the following measurements from RUNJOB [100] did not confirm this result, and were consistent with a similar spectral index for the two elements.

This scenario was partly clarified by another balloon experiment, CREAM, that was able to collect the largest statistics (up to now) for a direct measurement of cosmic protons and helium nuclei above 100 TeV. The CREAM data [101] are in agreement with JACEE, while suggesting higher fluxes, in particular for helium, with respect to RUNJOB. The proton and helium spectra measured by CREAM in the multi-TeV energy region are described by two power laws (E^γ) with different spectral indices: $\gamma_p = -2.66 \pm 0.02$ and $\gamma_{\text{He}} = -2.58 \pm 0.02$ in the energy range from 2.5 up to 250 TeV/n. At such high energies the proton spectrum is softer with respect to the helium one, and both spectra are harder than at lower energies (<100 GeV/n). In fact, precedent measurements from AMS-01 [102] and BESS [103] show a spectral index for proton of -2.78 ± 0.009 at 10-200 GV, and -2.732 ± 0.011 from 30 GeV to a few 100 GeV, respectively. Similarly, the observed helium spectrum is -2.740 ± 0.01 at

20-200 GV for AMS-01 and -2.699 ± 0.040 from 20 GeV/n up to a few 100 GeV/n for BESS.

Figure 6.2 shows the comparison between the CREAM data and a compilation of previous measurements from: the already mentioned AMS-01, BESS, JACEE, RUNJOB with CAPRICE98 [104] and ATIC-2 [105]. A fit of the CREAM observations with a single power law is shown as well (black solid line).

6.1.1 Recent measurement from PAMELA and AMS-02

At present, the only way to reconcile different spectral indexes, as measured by AMS-01/BESS and CREAM at different energies, is to assume an hardening of the spectrum in the hundred GeV region.

This phenomenon was in fact observed by the magnetic spectrometer PAMELA, which measured proton and helium spectra clearly inconsistent with single power laws, but exhibiting an abrupt hardening between 230 and 240 GV, with a change in the spectral index $\Delta\gamma \sim 0.2$ for protons and ~ 0.3 for helium nuclei, respectively [95]. Recently, also AMS-02 published its measurements on proton flux [65] and presented results for helium nuclei [96, 106]. The spectral hardening is measured precisely, and the spectral break is confirmed, for both elements.

AMS-02 is a space based multi-purpose spectrometer, launched in 2011 and installed on the ISS.

The core of the telescope is a 0.14 T permanent magnet coupled with a precise tracking system, based on silicon strip detectors. The tracker is capable to determine accurately the trajectory of charged particles inside the magnet and to measure the particle rigidity $R = Pc/Ze$ (where P is the momentum, Z the charge of the particle, and e the unitary charge). The maximum detectable rigidity (MDR), that corresponds to the value where the error of the measured rigidity becomes 100%, is of ~ 2 TV for proton and 3.2 TV for helium nuclei, respectively.

The charge of the incident particle is determined by multiple dE/dx measurements in the tracker and the resolution obtained is $\Delta Z \simeq 0.05$ for $|Z| = 1$ and 0.07 for $|Z| = 2$. Redundant charge and energy measurements are also provided by the Time of Flight counters (TOF), the Ring Image Cerenkov Counter (RICH), and the

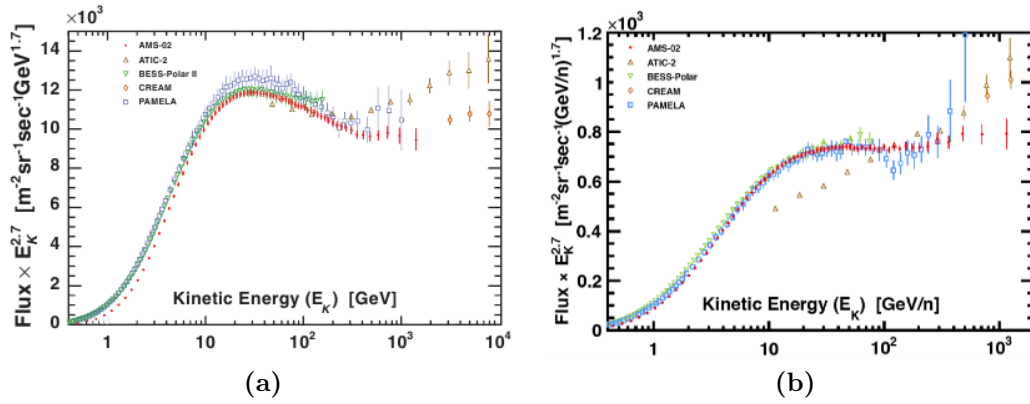


Figure 6.3: The AMS-02 measurements of proton (a) and helium (b) fluxes multiplied by $(E_k/n)^{2.7}$, as a function of kinetic energy per nucleon E_k/n . A comparison with the most recent results from spectrometers (BESS, PAMELA) and calorimetric experiments (ATIC-2, CREAM) is shown as well [65, 96].

Electromagnetic Calorimeter (ECAL). Moreover, a Transition Radiation Detector (TRD) is used to separate electrons and from protons, while a veto system (ACC) rejects events that enter the inner tracker from the side.

The AMS-02 mission has collected an unprecedented statistics of about 68×10^9 events, corresponding to more than the whole statistics of all the previous balloon-borne and space-based experiments. The flux measurements were carried out, as a function of rigidity, on a selection of events containing $\sim 300 \times 10^6$ protons and 50×10^6 helium nuclei, in the range between 1 GV and 1.8 TV, and from 1.9 GV to 3 TV for p and He, respectively. Also, the huge statistics surviving the selection allowed sophisticated analyses, comparable with that of collider experiments, allowing an accurate study of the systematic uncertainties.

The AMS-02 results for proton and helium flux measurements are illustrated in figures 6.3 and 6.4, as a function of kinetic energy per nucleon and rigidity, respectively. In figure 6.3 the latest AMS-02 results for proton (a) and helium (b) fluxes are shown as a function of kinetic energy per nucleon E_k/n and multiplied by $(E_k/n)^{2.7}$, in comparison with a compilation of recent results. In particular the recent observations of PAMELA [95] and BESS-Polar II [103] magnetic spectrometers are reported, as well as the results of balloon-borne calorimetric experiments ATIC-2 [105] and CREAM [101]. From the figure it is evident the really good agreement between PAMELA and AMS-02 results. In fact, in the energy region not affected

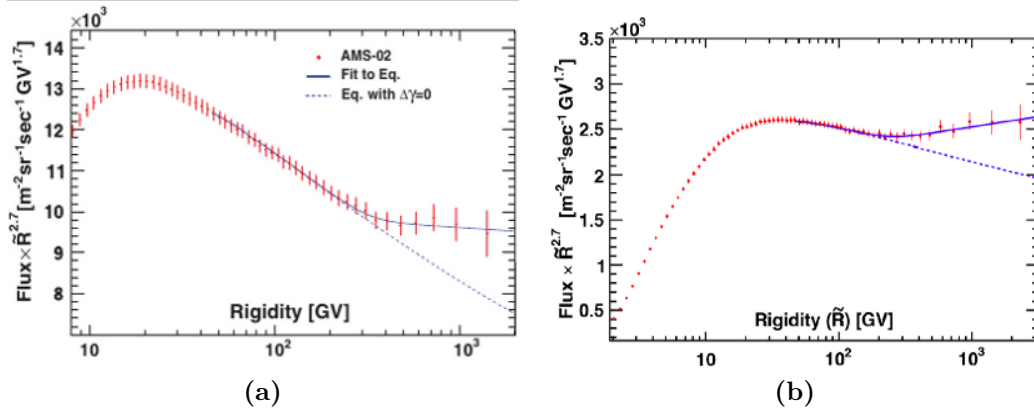


Figure 6.4: The spectra of proton (a) and helium (b) as a function of rigidity R and multiplied by $R^{2.7}$, from the latest AMS measurements. The solid line in both plots represents a fit with equation 6.1, while the dotted line shows the fit with $\Delta\gamma = 0$ (single power-law) [65, 96].

by solar modulation (rigidities >30 GV), the ratio between the two experimental flux measurements has been found to be 0.988 for protons and 1.036 for helium nuclei [107]. This is important to point out, as it is the first time in CRs history that the absolute fluxes observed by different experiments are in agreement at the percent level.

Figure 6.4 illustrates the proton (a) and helium (b) spectra as a function of rigidity R , and multiplied by $R^{2.7}$, in order to highlight the spectral hardening. Due to the huge statistics collected by AMS-02, the flux measurements are dominated by systematic uncertainties in the whole rigidity range. The statistical uncertainty is $< 1\%$, while the total proton flux error is about 4% at 1 GV, $< 2\%$ between 2 and 350 GV, and 6% above 1.1 TV. The systematic uncertainties come from several sources, including: the event selection, the unfolding procedure, the trigger efficiency, the background contamination, the acceptance calculation, the geomagnetic cut-off factor, the rigidity resolution function, and the absolute rigidity scale.

The presence of a deviation, around 300 GV, of the spectra from a single power law behaviour, is suggested as the data do not fit with $\Phi = CR^\gamma$ (at 99.9% C.L. for protons with $R > 45$ [65]). A more complex parametrization with a modified spectral index is proposed by the AMS-02 collaboration to fit the fluxes above 45 GV [65, 96]. Equation 6.1 shows the proposed fitting function, that represents a double power law, with a smooth transition from a spectral index γ , below the

transition rigidity R_0 , to $\gamma + \Delta\gamma$ above.

$$\Phi = C \left(\frac{R}{45\text{GV}} \right)^\gamma \left[1 + \left(\frac{R}{R_0} \right)^{\frac{\Delta\gamma}{S}} \right]^S \quad (6.1)$$

The fit performed with function 6.1 is illustrated in figure 6.4 by the solid line, both for protons (a) and helium (b), while the dotted line represent the fitted function with $\Delta\gamma$ set to 0. The fits results show that the spectral hardening is $\Delta\gamma = 0.133^{+0.032}_{-0.021}(\text{fit})^{+0.046}_{-0.030}(\text{sys}) \pm 0.005(\text{sol})^1$ for protons, and occur at $R_0 = 336^{+68}_{-44}(\text{fit})^{+66}_{-28}(\text{sys}) \pm 1(\text{sol})$ GV, while $C = 0.4544 \pm 0.0004(\text{fit})^{+0.0037}_{-0.0047}(\text{sys})^{+0.0027}_{-0.0025}(\text{sol})$, $S = 0.0024^{+0.020}_{-0.013}(\text{fit})^{+0.027}_{-0.016}(\text{sys})^{+0.006}_{-0.004}(\text{sol})$ and $\gamma_p = -2.849 \pm 0.002(\text{fit})^{+0.004}_{-0.003}(\text{sys})$. On the other hand the helium spectrum exhibits a different spectral index $\gamma_{He} = -2.780 \pm 0.005(\text{fit}) \pm 0.001(\text{sys})$, but a very similar rigidity dependence, with $\Delta\gamma = 0.119^{+0.013}_{-0.010}(\text{fit})^{+0.033}_{-0.028}(\text{sys})$ and $R_0 = 245^{+35}_{-31}(\text{fit})^{+33}_{-30}(\text{sys})$ GV. Moreover, the flux ratio of proton over helium can be fitted to a single power law with a constant spectral index, for rigidities above 45 GV, with $\gamma_{p/He} = -0.077 \pm 0.002(\text{fit}) \pm 0.007(\text{sys})$.

In conclusion, the recent measurements from PAMELA and AMS-02 finally cast some light on the proton and helium spectra from few GV to the TV region, and dictate a revision of the GCRs standard model, to find theoretical explanations for the origin of the observed hardening. Open scenarios include: a different acceleration mechanism at the source (i.e. distributed acceleration by multiple SNRs [108, 109], re-acceleration by weak shocks [110], non-linear DSA models [111, 112]); effects of CR propagation like an inhomogeneous diffusion [113], or a non-linear coupling of CRs with the diffusion coefficient [85, 114]); effects of the presence of local young sources [115–117], or of mixture of sources with different properties [118].

Moreover, AMS-02 results confirm that the proton spectrum is softer than the spectra of helium and heavier nuclei. This observation can be met by several theoretical explanations, including: different astrophysical sources for the two elements [119],

¹ The first error (fit) refers to the statistical and uncorrelated systematic errors of the flux measurement. The second (sys) is the error from the remaining systematic uncertainties (rigidity resolution function, unfolding, absolute rigidity scale) with their bin-to-bin correlations. The third (sol) is the uncertainty due to the variation of the solar potential.

a more efficient injection mechanism for helium [120], different abundance of p and He in SNR environments [121,122], or even different spallation rates during propagation [123].

Finally, a remark is in order. AMS-02 has already reached its upper limit (MDR) for magnetic measurements of p and He spectra, and therefore cannot push its momentum measurements much beyond a few TeV/n^2 . Thus, a precise observation of the proton and helium fluxes, above the spectral break, up to several 100 TeV/n is expected from purely calorimetric experiments already in orbit like CALET, or DAMPE and ISS-CREAM [125] in the near future.

6.2 Expected CALET performances

In this section a summary of CALET perspectives for proton and helium flux measurements is presented, the main expected uncertainties for these measurements are discussed, as well as the performance of the telescope for cosmic ray spectral observations. More detail is provided on tracking and charge identification, the main focus of this thesis work.

The number of expected helium and proton events is given in the energy range from 50 GeV/n to 25 TeV/n , assuming the AMS-02 parametrization for the fluxes and an observation period of 3 years. In addition to the observation period and detector acceptance, the event counts are computed taking into account the High Energy Trigger (HET) rate and the tracking and charge identification efficiencies. The expected proton and helium spectra in the energy range under investigation are shown as well, together with their relative statistical uncertainties. The systematic uncertainties arising from several sources are not directly investigated in detail, but their expected origin and evaluation strategy during the data analysis are outlined.

² AMS-02 can extend its energy range by using the TRD for nuclei with $Z \geq 2$, see [124] and the calorimeter's energy measurement. Unfortunately the latter has a thickness equivalent to only ~ 0.5 interaction length limiting the expected number of proton interactions in the instrument.

6.2.1 An estimate of proton and helium events in CALET

To evaluate the number of events expected in the CALET telescope, the proton and helium spectra from the most recent AMS-02 measurements have been used. In particular, for protons the flux has been taken directly from [65], in the form of equation 6.1, with the published coefficient. For helium, the flux is assumed again to be described by 6.1, while γ_{He} , $\Delta\gamma$ and R_0 are taken from the preliminary analysis results presented at ICRC 2015 conference (see [106] for a review). To obtain the unquoted parameters (C and S) a fit has been performed on the data extracted by figure 6.4 (b), with γ_{He} , $\Delta\gamma$ and R_0 fixed at the known values.

Since the AMS-02 spectra are parametrized as a function of rigidity, whereas for a calorimetric instrument a dependence on the measured energy seems more natural, a conversion from rigidity to kinetic energy per nucleon has been operated. It makes use of the well known kinematical formulae [126] shown by equation 6.2:

$$E_{k/n} = (\gamma - 1)E_{0/n} \quad (6.2)$$

where $E_{k/n}$ is the kinetic energy per nucleon, $E_{0/n}$ represent the rest mass energy per nucleon and γ is expressed in terms of rigidity by means of equation 6.3:

$$\gamma = \left[\left(\frac{RZ}{A/E_{0/n}} \right) + 1 \right]^{\frac{1}{2}} \quad (6.3)$$

where A is the atomic number of the particle under investigation, and $E_{0/n}$ can be computed as $(M_A/A)m_u$, with M_A the atomic mass expressed in a.m.u. (atomic mass unit) and m_u the value of 1 a.m.u. in GeV/c^2 .

Keeping in mind the relations 6.2 and 6.3 for the conversion from rigidity to energy per nucleon, and knowing that:

$$\frac{dN}{dE_{k/n}} = \frac{dN}{dR} \frac{dR}{dE_{k/n}}$$

the expression 6.4 for flux conversion is obtained [127]:

$$\frac{dN}{dE_{k/n}} (\text{m}^2\text{sr s GV})^{-1} = \frac{A}{Z} \frac{(E_{k/n} + E_{0/n})}{\sqrt{E_{k/n}(E_{k/n} + 2E_{0/n})}} \frac{dN}{dR} (\text{m}^2\text{sr s GeV/n})^{-1}. \quad (6.4)$$

Then, as the AMS-02 spectra parametrization is valid above 45 GV and the charge identification performances have been studied till 100 TeV per nucleus, we decided to perform a first evaluation of the expected number of events in the energy range from 50 GeV/n to 25 TeV/n. The whole energy range has been divided into 18 logarithmic bins, calculated in equal steps of $10^{0.15}$. Then, for each bin, the number of proton and helium events is calculated taking into account the integral flux on the bin ($\Delta\Phi$), the detector acceptance ϵ , and the exposure time (T):

$$N_{evt} = \Delta\Phi \cdot \epsilon \cdot T.$$

This provides an estimate of the number of physical events that are expected in the detector per energy bin. To obtain the number of events that can be effectively used for analysis purposes, this value has to be scaled with the fraction that fired the High Energy Trigger. In fact to reconstruct precisely the CR energy it is needed that the incoming particle undergoes an interaction in the calorimeter generating an HET. For this reason, only the fraction of HET events are suitable for the analysis. Moreover, a proper tracking of the event and the reconstruction of the particle charge are mandatory. To obtain an estimate of the number of proton and helium events, their HET fraction, the tracking efficiency (with respect to triggered events) and the charge reconstruction efficiency for each bin under study, the FLUKA Monte Carlo was used.

In figure 6.5 the charge reconstruction efficiencies are shown, together with the contamination, as resulting from a calculation over the 18 logarithmic bins in energy per nucleon from 50 GeV/n to 25 TeV/n, both for helium (a) and protons (b). The evaluation of the charge discrimination efficiency is made with the same analysis method reported in figure 5.14 (i.e.: the CHD detector is used to reduce the contamination of the sample selected by the IMC), but with two important differences. The first one is that the analysis is carried out as a function of the kinetic energy per nucleon rather than on total kinetic energy. The second, more significant, is that in this case no additional selection (on the true primary track identity) is made on the candidate tracks before charge reconstruction.

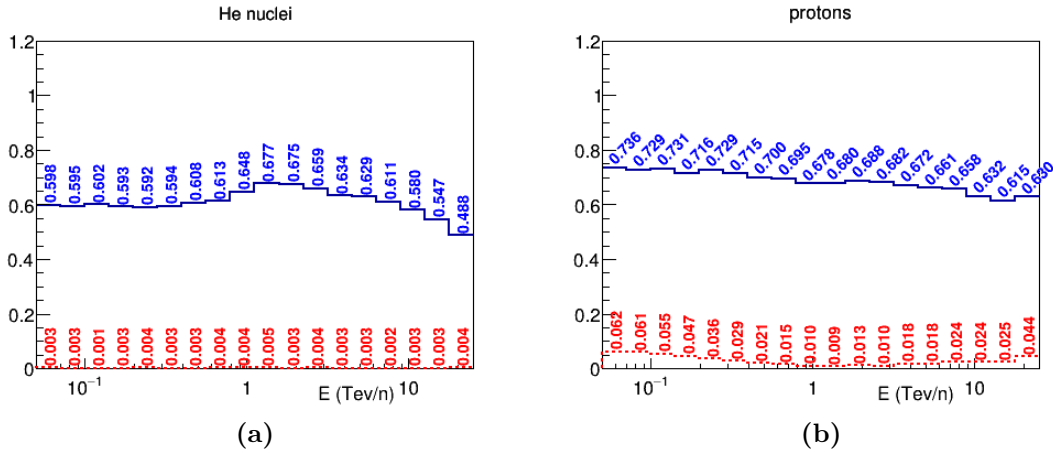


Figure 6.5: Efficiency (blue continuous line) and contamination (red dashed line) of helium (left) and proton signals (right) vs. bin energy. The results are obtained for 18 logarithmic bins in kinetic energy per nucleon, from 50 GeV/n to 25 TeV/n, for the whole sample of tracked HET events.

The results of the analysis are displayed at the end of this chapter, in table 6.1 for protons and in table 6.2 for helium nuclei. In both cases, the first column shows the bin number, and the second one the bin energy range, while the third reports the total number of expected events evaluated on the basis of AMS-02 fluxes parametrization, and taking into account an acceptance of $0.042 \text{ m}^2\text{sr}$ for type 1 events (see 2.3). In the other columns it is shown, both in counts and in percentage, the number of HET events, the tracked ones, the cases whereby the charge is identified correctly and those where it is misidentified. The percentage of HETs is computed with respect to the total, while the tracking efficiency is normalized to HET triggers, and finally both fractions of correct and wrong charge tagging are calculated with respect to the number of tracked events.

The information displayed in detail in tables 6.1 and 6.2 are illustrated by figures 6.6 and 6.7 respectively. In the first figure (top) the number of expected protons are shown bin per bin by the blue solid line, while the black markers show the number of reconstructed proton events and the red empty triangles are the number of contaminating cosmic helium nuclei. On the bottom side of the same figure, instead, the red markers show for each bin the ratio between the number of helium events reconstructed as protons with respect to the signal itself, with a contamination of the order of 1%, or better.

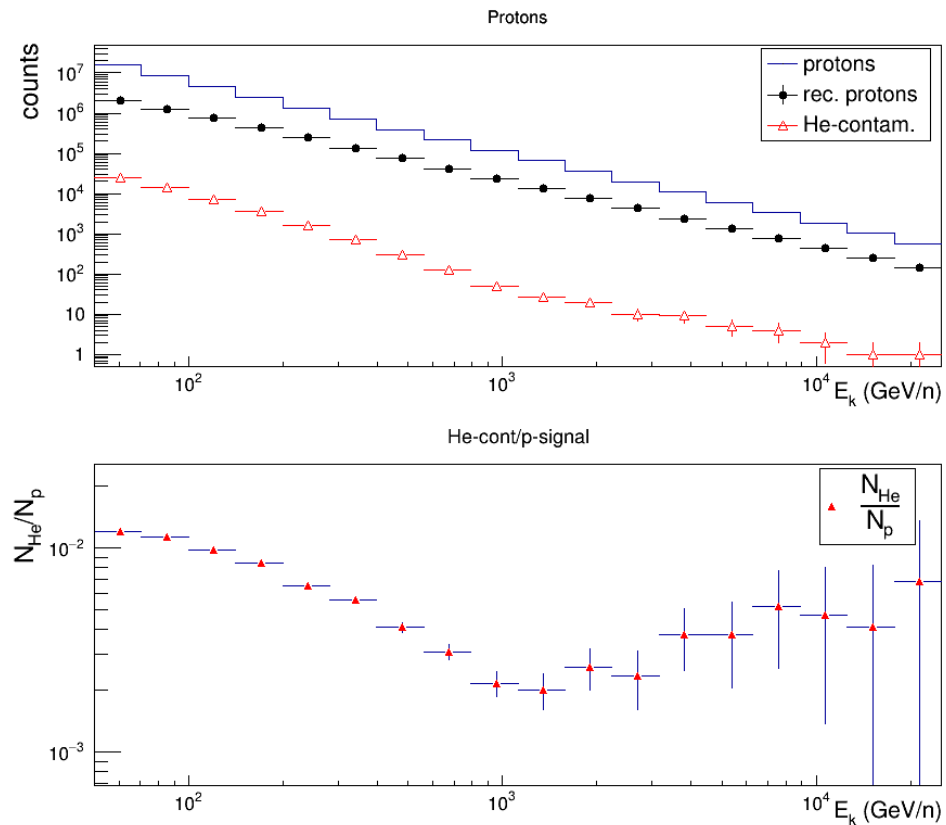


Figure 6.6: Top: anticipated number of protons events in 3 years in a restricted acceptance region of CALET (blue solid line) vs. kinetic energy per nucleon, together with the reconstructed protons (black solid circles), and the contamination from helium events (red empty triangles). Bottom: ratio N_{He}/N_p between the number of helium nuclei contaminating the proton signal and the signal itself.

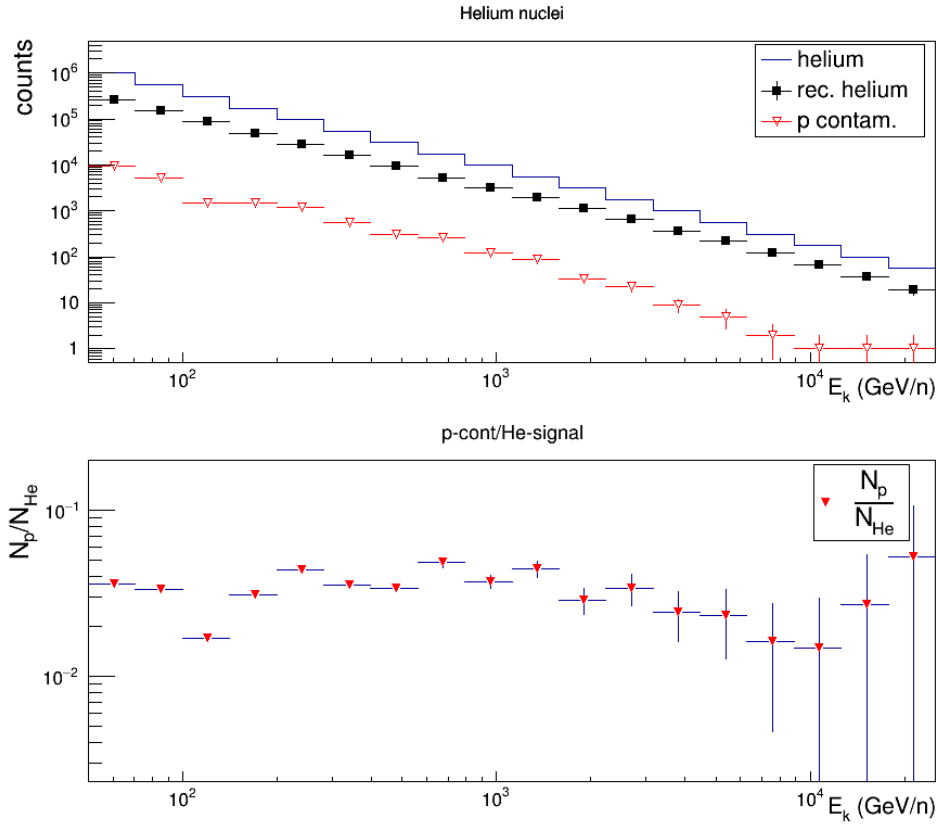


Figure 6.7: Top: the anticipated number of helium nuclei in 3 years in a restricted acceptance region of CALET (blue solid line) is shown per energy bin, together with the reconstructed signal (black solid squares), and the contamination from proton events (red downward triangles). Bottom: ratio N_p/N_{He} between the number of protons contaminating the signal and the helium nuclei properly reconstructed.

In figure 6.7 (top side), the blue solid line represents the expected helium ions, the black squares are the nuclei properly reconstructed by the telescope, and the red downward triangles are the proton events contaminating the signal. Once again, the plot at the bottom side shows the ratio of contaminating particles with respect to the reconstructed signal. This time the contamination is noticeably higher than for the protons sample, though below the 5% level.

6.2.2 Flux measurements perspectives with the CALET telescope

In this section a brief summary on how the CALET telescope can achieve accurate flux measurements is given by discussing the major points of the analysis and the

contribution of the developed method for tracking and charge identification.

For each energy bin i under investigation, the isotropic flux for each element Φ_i is evaluated as:

$$\Phi_i = \frac{N_i}{A \varepsilon_i T \Delta E_i}, \quad (6.5)$$

where N_i is the number of energy deconvoluted events in the bin, ΔE_i is the size of the bin, A is the acceptance, T is the live time, and ε_i is the efficiency resulting from all the analysis steps, as described by the following equation:

$$\varepsilon_i = \varepsilon_i^{trig} \cdot \varepsilon_i^{rec} \cdot \varepsilon_i^{sel} \cdot \varepsilon_i^{charge} \quad (6.6)$$

Where ε_i^{trig} is the trigger efficiency, i.e. the fraction of events satisfying the trigger condition among all the particles within the geometrical acceptance of the detector (energy dependent); ε_i^{rec} is defined as the ratio of events satisfying the reconstruction and trigger conditions normalized to all triggered events, where “reconstruction condition” means that for the selected event all the basic information needed for the analysis (in particular tracking), has been properly reconstructed; ε_i^{charge} refers to the percentage of events of a given element for which the corresponding charge has been reconstructed, and takes into account event losses (e.g. instrumental inefficiency, interaction before charge detection) as well as misidentified charges. Finally ε_i^{sel} is needed to take into account the fraction of events removed from the analysis for different reasons, as for instance a too late interaction in the calorimeter or rejected by other cuts.

Operatively, to measure the flux, the N_i^{dep} entries in the deposited energy bins must first be deconvoluted into bins of incident energy. Several methods can be used to achieve this result. Widely used is the “deconvolution matrix” one [101, 128]:

$$N_i^{inc} = \sum_j P_{ij} N_j^{dep}. \quad (6.7)$$

Where N_i^{inc} is the number of events in the incident energy bin i , estimated from the measured counts N_j^{dep} . The matrix element P_{ij} gives the probability that the events in the deposited energy bin j come from the incident energy bin i . It is

possible to compute each element of the energy mixing matrix P_{ij} directly from MC simulations, considering each simulated CR with an energy in bin i falling into measured energy bin j , and incrementing the response matrix element α_{ij} and the count n_j . The deconvolution matrix is then given by $P_{ij} \equiv \alpha_{ij}/n_j$. Clearly, two separate deconvolution matrices are needed for protons and helium nuclei.

Then, all the other parameters for the flux estimate must be evaluated by MC simulation or, whenever possible, directly from the measured data. In particular, the acceptance A and the trigger efficiency ε_i^{trig} should be evaluated mainly via MC simulations, and cross-checked with flight data studying the relative efficiencies of sub-system components, while for ε_i^{rec} , ε_i^{charge} and ε_i^{sel} direct measurements from flight data are possible, and should be checked against MC predictions.

Furthermore, statistical and systematics uncertainties must be evaluated for each one of the above correction factors.

- The use of extensive MC simulations for the A estimate can in principle reduce at will its statistical error, but the systematic uncertainties must be evaluated. For example, one can compute A with different codes MC (FLUKA, EPICS, GEANT4) and compare the results with data (using flux values from previous measurements or measuring the ratio between different acceptance definitions).
- ε_i^{trig} can be estimated from MC simulations and can be checked comparing the ratio between different trigger conditions with data and MC.
- For ε_i^{charge} , different algorithms or even different detectors (CHD and IMC) can be used to measure directly the relative efficiencies on flight data. For example it is possible to measure the incoming charge with the CHD and use it as reference to compute the IMC charge tagging efficiency (and vice versa). The same thing can be made also for the two different algorithms used for the charge reconstruction. Consequently, systematic uncertainties can be computed comparing these different measurements of the same quantity with each other, and vs. MC simulations. Moreover, the parameters used to make the charge selection with a given algorithm can be varied over a certain range to get an estimate of the systematics.

- A similar procedure can be applied in principle to ε_i^{rec} and ε_i^{sel} too, but it is more difficult to achieve a redundant tracking or interaction point identification with different detectors, and therefore the efficiency calculation and estimates of systematical errors would rely more on MC simulations.
- For N_i the systematic uncertainty arises mainly from the deconvolution process. A way to estimate it, is to compare different unfolding procedures, and additionally apply many times the same procedure but relying on different MC simulations. For example, the simulated spectral shape used for the P_{ij} calculation can be varied, testing the deconvolution matrix dependence on it.
- Live time calculation, calibration accuracy and background events (like those entering the detector from the bottom), must be taken into account as possible error sources and treated appropriately.

In addition to the above, for the proton flux measurement also the irreducible physical background from antiprotons must be taken into account, as the CALET telescope does not have the possibility to distinguish between positive and negative charges. Anyway, the ratio between the antiproton and proton fluxes is comfortably small, as it is shown in figure 6.8 where different measurements of this quantity are reported [92]. Electron and positron misidentified as protons, could in principle

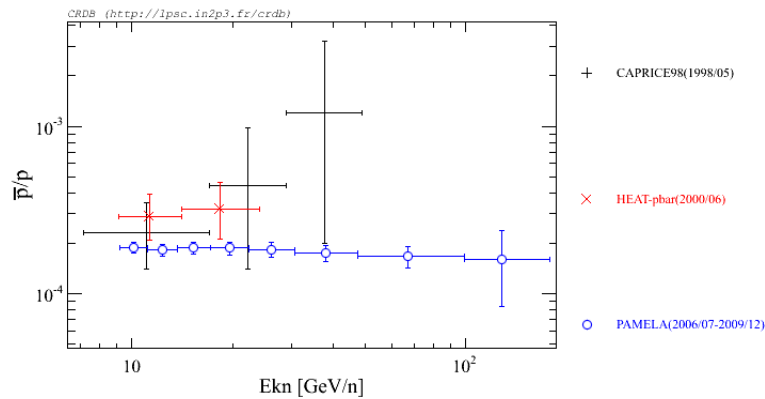


Figure 6.8: Antiproton to proton flux ratio from different experiments [92].

represent another physical background for the proton flux measurement, However, similar considerations hold, as their flux is 3-4 orders of magnitude lower than proton one and, in addition to that, a really efficient discrimination between the two

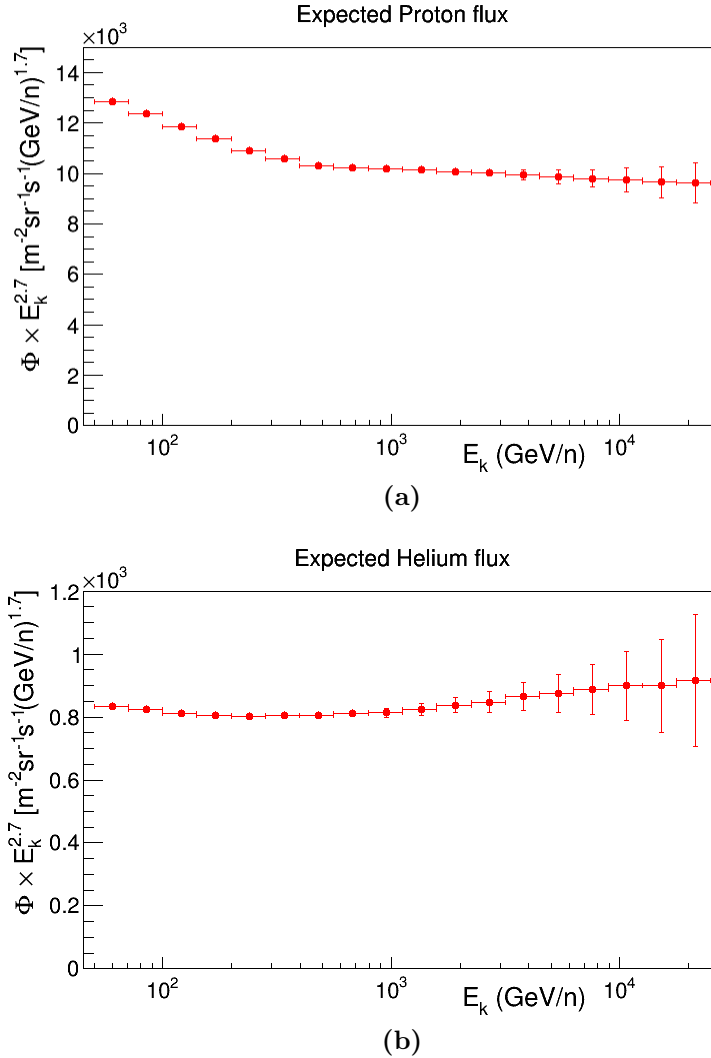


Figure 6.9: The expected proton (a) and helium (b) fluxes as a function of kinetic energy per nucleon E_k multiplied by $E_k^{2.7}$, in the range from 50 GeV/n up to 25 TeV/n in a restricted range of the acceptance. The error bars show the statistical uncertainty for each bin for 3 years of data taking, assuming the AMS-02 measured spectra.

species is possible with the CALET detector (see section 3.1.2), making this background definitively not an issue for the proton flux measurement.

In figure 6.9 it is shown an estimate of the proton (a) and helium (b) fluxes, multiplied by $E_k^{2.7}$ as expected after 3 years of data taking with the CALET telescope using a restricted fiducial acceptance (type 1). This flux estimate is made starting from the anticipated number of events reported in table 6.1 and 6.2, and the error bars are representative only of the statistical uncertainty propagated to the fluxes. For this exercise the flux is obtained from equation 6.5 without energy deconvolution, and taking for acceptance, live time and efficiencies the same parameters used

to compute the expected number of events. No statistical fluctuations are introduced in the flux estimates, except than caused by rounding the event numbers to integers. For what concerns the efficiencies, ε_i^{trig} refers to the fraction of HETs in bin i , while ε_i^{rec} represents only the tracking efficiency and $\varepsilon_i^{sel} = 1$ as no additional selections are applied. Instead, ε_i^{charge} stands for the percentage of properly identified particles, where a biased measurement of charge can arise both from inefficiencies of the adopted algorithm and from a wrong identification of the primary particle (due to tracking). It has to be mentioned that the simulated points in the figure are drawn for each bin in correspondence to an energy value \bar{E}_i , taken as the arithmetic mean of E_i and E_{i+1} in the logarithmic bin. For a more refined analysis a suitably weighted average of the flux inside each bin can be used, or \bar{E}_i can be taken, more properly, as the point where the value of the predicted flux is equal to its mean value over the width of the bin [129], or in other words it has to satisfy equation 6.8:

$$\Phi(\bar{E}_i) = \frac{1}{E_{i+1} - E_i} \int_{E_i}^{E_{i+1}} \Phi(E) dE \quad (6.8)$$

The actual binning of the events will be chosen according to the energy dependence of the calorimetric energy resolution, in order to minimize the spill-over from a given energy bin into the adjacent ones. For an accurate measurement of the spectrum curvature in the region between 100 GeV and a few TeV, the bin size will be probably similar (or smaller) than the one used in the above exercise, while in the region above 10 TeV up to several hundreds TeV the bin width will be larger and the exploration of the highest energies will take advantage of the full exposure of CALET with a goal of 5 years of data taking.

In conclusion, it was shown that the CALET telescope has good perspectives to perform its first measurement of the p and He spectra up to 25 TeV/n in 3 years of data taking, using only the most conservative acceptance and the algorithms for tracking and charge reconstruction developed within this thesis work. Clearly this is neither the arrival point of the analysis nor the limit of the CALET potential for these measurements. It just represents a starting point. In a second stage of the analysis, when the behaviour of the detector in flight will be completely understood,

refinement of the algorithms and improvements in the efficiencies will open the way to the use of the full detector acceptance, allowing CALET to increase its energy reach and to extend its spectral measurements to less abundant nuclei.

bin number:	bin range:	tot. events:	HET events: count. - (%)	tracked: count. - (%)	rec. protons: count. - (%)	p rec. as He: count. - (%)
1	[50.0,70.6269]	16315115	3459701 (0.212)	2813771 (0.813)	2072302 (0.736)	9505 (0.00338)
2	[70.6269,99.7631]	8727656	1961671 (0.225)	1713211 (0.873)	1248358 (0.729)	5049 (0.00295)
3	[99.7631,140.919]	4651769	1110521 (0.239)	1005943 (0.906)	735772 (0.731)	1465 (0.00146)
4	[140.919,199.054]	2473699	623174 (0.252)	583816 (0.937)	418058 (0.716)	1494 (0.00256)
5	[199.054,281.171]	1316052	343638 (0.261)	329079 (0.958)	239878 (0.729)	1206 (0.00367)
6	[281.171,397.164]	706227	188691 (0.267)	183151 (0.971)	130913 (0.715)	559 (0.00306)
7	[397.164,561.01]	385580	108334 (0.281)	105778 (0.976)	74051 (0.7)	311 (0.00294)
8	[561.01,792.448]	212774	60509 (0.284)	59597 (0.985)	41427 (0.695)	255 (0.00428)
9	[792.448,1119.36]	117698	34129 (0.29)	33834 (0.991)	22942 (0.678)	121 (0.0036)
10	[1119.36,1581.14]	65115	19053 (0.293)	18887 (0.991)	12841 (0.68)	87 (0.00462)
11	[1581.14,2233.42]	36018	11173 (0.31)	11114 (0.995)	7647 (0.688)	33 (0.00299)
12	[2233.42,3154.79]	19920	6219 (0.312)	6176 (0.993)	4209 (0.682)	22 (0.00361)
13	[3154.79,4456.27]	11016	3551 (0.322)	3536 (0.996)	2375 (0.672)	9 (0.00273)
14	[4456.27,6294.64]	6091	2021 (0.332)	2010 (0.995)	1329 (0.661)	5 (0.0025)
15	[6294.64,8891.42]	3368	1180 (0.35)	1173 (0.995)	771 (0.658)	2 (0.00226)
16	[8891.42,12559.5]	1862	678 (0.364)	673 (0.994)	425 (0.632)	1 (0.00253)
17	[12559.5,17740.7]	1029	400 (0.39)	398 (0.996)	244 (0.615)	1 (0.0032)
18	[17740.7,25059.5]	569	234 (0.412)	233 (0.996)	146 (0.63)	1 (0.0043)

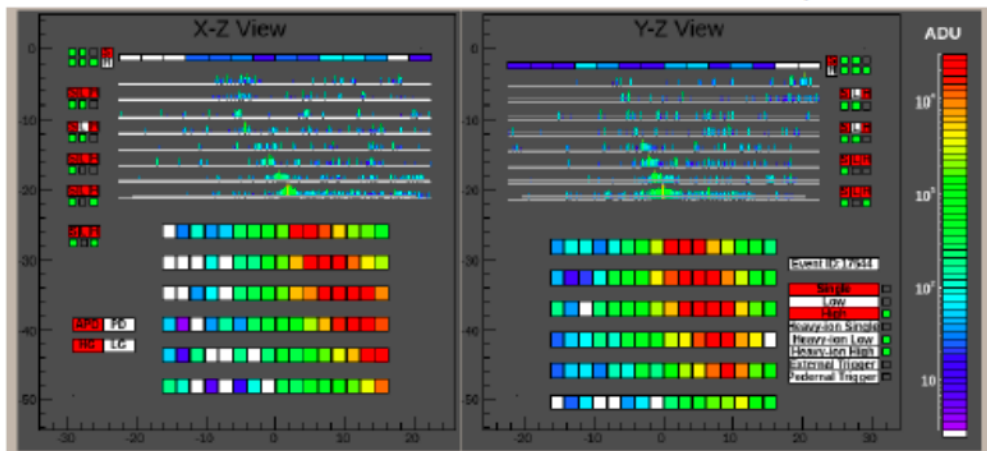
Table 6.1: Expected total number of protons in the CALET telescope in 3 years, within a restricted fiducial acceptance of 0.042 m²sr for type 1 events, together with the expected numbers of HETs, properly tracked events, correctly identified particles and misclassified ones.

bin number:	bin range:	tot. events:	HET events: count. – (%)	tracked: count. – (%)	rec. protons: count. – (%)	He rec. as p: count. – (%)
1	[50.0,70.6269]	1014385	419234 (0.413)	402621 (0.96)	240798 (0.598)	25156 (0.0625)
2	[70.6269,99.7631]	558005	238225 (0.427)	231346 (0.971)	137568 (0.595)	14140 (0.0611)
3	[99.7631,140.919]	308376	134998 (0.438)	131885 (0.977)	79336 (0.602)	7218 (0.0547)
4	[140.919,199.054]	172115	76840 (0.446)	75694 (0.985)	44872 (0.593)	3528 (0.0466)
5	[199.054,281.171]	96822	44432 (0.459)	43811 (0.986)	25925 (0.592)	1576 (0.036)
6	[281.171,397.164]	54626	25523 (0.467)	25308 (0.992)	15039 (0.594)	732 (0.0289)
7	[397.164, 561.01]	30832	14780 (0.479)	14663 (0.992)	8912 (0.608)	303 (0.0207)
8	[561.01,792.448]	17397	8459 (0.486)	8397 (0.993)	5147 (0.613)	129 (0.0155)
9	[792.448,1119.36]	9812	4964 (0.506)	4928 (0.993)	3193 (0.648)	50 (0.0103)
10	[1119.36,1581.14]	5533	2879 (0.52)	2862 (0.994)	1937 (0.677)	26 (0.00923)
11	[1581.14,2233.42]	3119	1671 (0.536)	1665 (0.997)	1124 (0.675)	20 (0.0125)
12	[2233.42,3154.79]	1758	970 (0.552)	966 (0.997)	636 (0.659)	10 (0.0105)
13	[3154.79,4456.27]	990	571 (0.577)	569 (0.998)	360 (0.634)	9 (0.0176)
14	[4456.27,6294.64]	558	338 (0.606)	336 (0.997)	211 (0.629)	5 (0.0178)
15	[6294.64,8891.42]	314	199 (0.635)	198 (0.998)	120 (0.611)	4 (0.0239)
16	[8891.42,12559.5]	177	115 (0.652)	114 (0.995)	66 (0.581)	2 (0.0235)
17	[12559.5,17740.7]	99	67 (0.68)	66 (0.99)	36 (0.547)	1 (0.0249)
18	[17740.7,25059.5]	56	39 (0.698)	38 (0.98)	18 (0.488)	1 (0.0441)

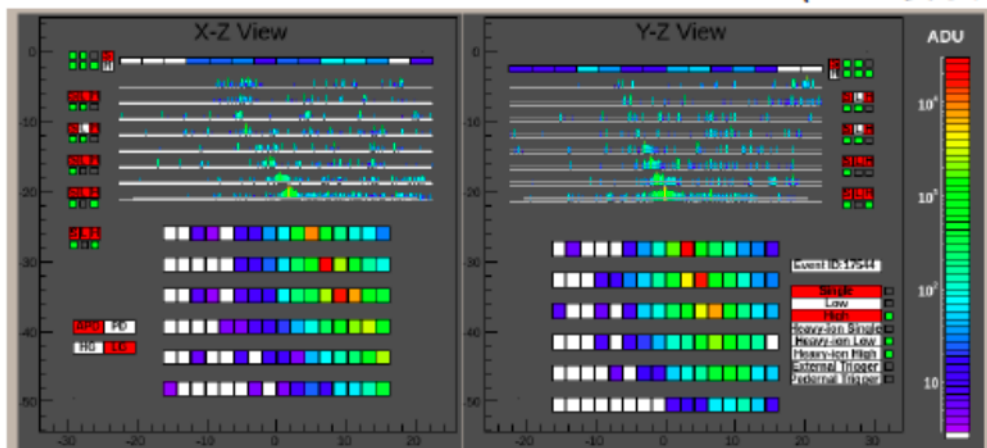
Table 6.2: Expected total number of helium nuclei in the CALET telescope during 3 years, within a restricted fiducial acceptance of 0.042 m²sr for type 1 events, together with the expected numbers of HETs, properly tracked events, correctly identified particles and misclassified ones.

Present status of CALET

After the successful launch from the Tanegashima Space Center on August 19th (EDT) on board the Japanese H2-B rocket, the berthing with the ISS a few days later (August 24th), and the installation on the external platform JEM-EF of the Japanese module (KIBO), the check-out phase of the instrument went on smoothly. The on-orbit commissioning phase aboard the International Space Station, was successfully completed in the first days of October, and CALET is now moving to science operations for a first initial period of 2 years. The observations of high energy charged particles and photons coming from space has started, and the first events at energies in the Tera electron Volt region have been recorded and are under study. In figure 6.10 it is shown the detailed shape of the development of a shower of secondary particles generated by the impact of a candidate electron with an estimated energy larger than 1 TeV (raw data). We are looking forward to collect a large statistics, to check out the instrument behaviour and perform precise in-flight calibrations and accurate studies to validate and improve the present algorithms for flight data analyses, leading to physical measurements.



(a)



(b)

Figure 6.10: An event image (raw data) acquired at higher sensitivity (a) and lower sensitivity (b) showing an event preliminarily identified as an electron candidate in the TeV region.

Conclusions

The IMC detector is of fundamental importance for CALET to achieve its extensive physics program. In particular, tracking is mandatory to reconstruct the incident particle's angle and direction, as well as the shower starting point, essential for precise energy measurements.

In this thesis work, a Kalman filter algorithm has been developed for tracking inside the IMC, together with a strategy to identify the primary particle among all the reconstructed tracks. This algorithm allows to achieve a high tracking efficiency together with a good resolution, both in spatial and in angular coordinates, for different particle species.

Tests to validate the tracking have been applied, both on Monte Carlo samples (of electrons, protons, helium and carbon nuclei), and on Test Beam data (electrons, protons and muons). The conclusion of these studies is that the measured performances turn out to meet the requirements of the CALET instrument.

As expected, for the MC sample the performances are better for MIPs and electrons with ($\geq 97\%$ efficiency and $\leq 0.1^\circ$ angular resolution), while they are worse for HET events ($\geq 91\%$ efficiency and $\leq 0.32^\circ$ of angular resolution), because track finding and also primary track identification are complicated by the much higher track and cluster multiplicity in the detector.

The tracking algorithm was found to behave as expected also in the case of real data with an efficiency higher than 95% for all the beam test data samples analysed.

Another important topic of this thesis, resulting from the original work of the candidate, is the development of analysis tools for the particle's charge reconstruction with the IMC.

It consists mainly of two parts, the first one is the reconstruction of the Interaction

Point (IP) of the incoming particle in the IMC and the second one is the determination of the particle's charge using multiple samples of ionization energy loss from the IMC layers upstream of the IP.

Two different algorithms have been developed for the IP reconstruction and are described in detail in chapter 4. Both of them are found to work well and with good accuracy for helium and protons events. From extensive tests on MC samples, it turns out that in most cases the IP is reconstructed correctly within plus or minus one plane (about ± 2 cm along z), and only in a limited number of cases the reconstruction fails. There are not significant differences in the behaviour between the two different methods, nor between the two kind of particles under test. An issue for these algorithms is represented by the events interacting upstream of the IMC, or in the first layers of the instrument, as in this case no IP reconstruction is possible, but only a rejection of the event depending on some specific cuts. Some possible rejection cuts and their effectiveness are discussed.

For the measurement of the incident particle's charge, three different methods have been developed. All of them produce quite good results, but none of them is prominent. All have to tackle the demanding issue of particle interactions upstream the IMC.

In most cases not only the performances, but also the behaviour of the different methods is similar. The signal efficiency depends on energy, both for helium and for proton, decreasing from more than 90-95% around 100 GeV to about 50-60% at higher energies (100 TeV), while the contamination remains below 5-6% with a maximum around 400-700 GeV for helium and below 3-4% for protons with a maximum around ~ 100 GeV. These results are promising, but to perform an accurate measurement of the proton and helium fluxes, an additional effort has been made to achieve better performances with a combined use of the IMC detector and the CHD. Using the CHD detector to refine the IMC charge identification, an important reduction of contamination has been achieved (reaching a few 1‰ residual contamination) without a significant loss of efficiency.

After this detailed MC study, the developed methods were then validated on Test Beam data samples at energies up to 400 GeV/n. Also in this case the charge tag-

ging performances were found to be quite good for all the developed algorithms, and comparable with those expected from the analysis of MC data. The percentage of charge properly identified for protons varies from about 87% to 91%, and rises to about 93% to 97% for helium, while the fraction of misidentified events is less than 1% for helium nuclei, and of the order of 2–4% for protons (using only the IMC for the charge reconstruction).

Finally, using the developed algorithms for tracking and charge reconstruction, with the most conservative acceptance, the anticipated proton and helium counts in CALET are computed, for 3 years of data taking, up to an energy of 25 TeV/n. The expected proton and helium flux measurements (in the energy range from 50 GeV/n to 25 TeV/n) are shown as well, together with their relative statistical uncertainties. Systematic errors and their evaluation strategy during the data analysis are outlined. It was shown that the CALET telescope has good perspectives to perform its first measurement of the p and He spectra up to at least 25 TeV/n in 3 years of data taking, and using the most conservative fiducial acceptance. The energy of 25 TeV/n doesn't represent neither the arrival point of the analysis, nor the limit of the CALET potential for these measurements. It is just an upper limit chosen for the present analysis in a restricted range of the acceptance. The methods for tracking and charge reconstruction presented in this thesis are intended as a starting point of the analysis of flight data for a direct measurement of proton and helium spectra with CALET. In a second stage of the analysis, a comprehensive understanding of the in-flight detector behaviour will allow a refinement of the algorithms, to use the full detector acceptance and improved efficiencies. A target period of 5 years of observations on the ISS will allow CALET to increase its energy reach and to extend its spectral measurements to less abundant nuclei.

Brief summary of candidate's activity

The candidate started its research activity as a Ph.D. student in 2012, working with the Italian team of the CALET collaboration on the development of the offline analysis software.

In particular he focused his efforts in understanding the imaging calorimeter (IMC) response to different incoming particle species of interest (electrons, protons, muons, helium and carbon ions), and then he used the acquired knowledge to provide an important contribution to the development of suitable algorithms for tracking and charge reconstruction. This has been a challenging work but of great importance for the experiment. The aim was to extend to the IMC the capability to provide a redundant charge tagging (via multiple dE/dx samples from several layers of scintillating fibers) in addition to the charge measurement from the dedicated charge detector CHD.

The candidate accomplished this task working both on Monte Carlo simulations to study the behaviour of the algorithms, and on real Test Beam (TB) data, to validate the MC results. At the end of his Ph.D. term, different methods for tracking and charge identification were implemented and validated, showing a good level of performance.

Then, in perspective of in-flight measurements of the spectra of proton and helium, he calculated the expected fluxes and the effective collection power of CALET for a first data taking period of 3 years, evaluating the statistical uncertainties as well as the main sources of systematic errors and a strategy for their assessment from the data. The candidate played also an active role in test beam activities, during three

different campaigns with SPS extracted beams at the CERN North Area facility, in October 2012, January 2013 and March 2015. As part of his work on the TB data he was also involved in the IMC fibers calibrations and in the analysis of the data. In 2015 he attended two conferences on behalf of the CALET collaboration: the International Cosmic Ray Conference (ICRC) in The Hague, where he showed partial results of this thesis work [130], and the 101st National Congress of the Italian Physical Society (SIF) in Rome, where he presented an overview of the CALET experiment (that had been installed on the ISS just a few days before) and its expected physics goals.

Furthermore, during the whole period as Ph.D. student, the candidate worked in parallel on two different R&D projects funded by INFN and carried out by the same group at the University of Siena (this work is not described in the thesis). In particular he contributed to the development of custom electronic boards and wrote the firmware for the readout of silicon sensor matrix arrays for cosmic ray charge measurements [131, 132], and for an innovative prototype of Focused Differential Internal Reflection Cherenkov (FDIRC) detector [133]. Within this last project, he also contributed to the construction of the mechanical support structure of the prototype and gave an important contribution to the test with ion beams at CERN, during the 2015 campaign [134].

Acknowledgements

At the end of this thesis work, it is a pleasure for me to thank all the people that made this thesis possible. In particular I would like to express my gratitude to Prof. Pier Simone Marrocchesi for his tireless help, guide and teaching, and to Dr. Paolo Maestro for his precious assistance and support.

I'm pleased to thank Simone Bonechi, Gabriele Bigongiari, Francesco Palma, Francesco Stolzi, Nicola Mori and all the CALET Italian team for their aid to my thesis and to me with their knowledge and friendship. I am grateful to all the CALET people, in Italy and not, that helped me during this period.

I'm also indebted with all my colleagues and friends at the University of Siena: Lilliana, Roberto, Maria Grazia, Leonardo, Cesare, Arta and many others for providing a stimulating and fun environment in which to learn and work.

A special thanks goes to all my friends that stand by me since a long time. Thanks Guys.

Lastly, and most importantly, I wish to thank my parents, my family and Valentina for all the great and small things they do everyday for me.

Alla fine di questo lavoro di tesi, vorrei spendere due parole per ringraziare tutti coloro che mi hanno aiutato e ne hanno reso possibile la realizzazione. Prima di tutto voglio ringraziare il Prof. Pier Simone Marrocchesi che durante questo lavoro di tesi mi ha corretto, guidato ed insegnato molto.

Voglio quindi ringraziare il Dr. Paolo Maestro per l'aiuto, il supporto ed i preziosi consigli.

Un ringraziamento particolare va poi a Simone Bonechi, Gabriele Bigongiari, Fran-

cesco Palma, Francesco Stolzi, Nicola Mori e tutti gli altri membri italiani di CALET, per il loro aiuto durante tutto questo periodo sia nella parte tecnica, con la loro conoscenza, che in quella umana, con la loro amicizia.

Voglio ringraziare tutte le persone della collaborazione CALET che mi hanno aiutato in questo periodo.

Inoltre ringrazio tutti i miei amici e colleghi dell'Università di Siena: Liliana, Roberto, Maria Grazia, Leonardo, Cesare, Artà e molti altri, per il loro supporto nel lavoro e non solo.

Ai miei amici di sempre dedico un grazie speciale, perché da molto tempo condividono con me i momenti importanti rendendoli più veri, ed il tempo che spendo con loro è sempre per me prezioso, nei momenti belli come in quelli brutti.

Infine il ringraziamento più importante va alla mia famiglia e a Valentina. Perché sono loro che con piccoli o grandi gesti mi sostengono ogni giorno, dando senso a questo come agli altri momenti della vita.

La dedica di questo lavoro va ai miei genitori, con affetto.

Bibliography

- [1] Hess V., Phys. Z. 13 (1912) 1084.
- [2] J. Clay, Proc. Acad. Wetesch., Amsterdam, 30:633 (1927).
- [3] T. H. Johnson, Phys. Rev., 43:834 (1934).
- [4] L. Alvarez & A. H. Compton, Phys. Rev. 43:835 (1934).
- [5] B. Rossi, Phys. Rev., 45:212 (1934).
- [6] C.D. Anderson, *The Positive Electron*. Physical Review 43 (6): 491. (1933).
- [7] P. Auger et al., *Extensive Cosmic-Ray Showers*. Rev. Mod. Phys. 11 (3-4): 288–291.
- [8] E. Fermi. *On the Origin of the Cosmic Radiation*. Physical Review, 75: 1169–1174. (1949).
- [9] J. Beringer et al. (Particle Data Group), Phys. Rev. D86, 010001 (2012).
- [10] K. Greisen. *End to the Cosmic-Ray Spectrum?* Phys. Rev. Lett., 16:748–750, 1966.
- [11] G. T. Zatsepin and V. A. Kuzmin. *Upper Limit of the Spectrum of Cosmic Rays*. Soviet Journal of Experimental and Theoretical Physics Letters, 4:78–80, 1966.
- [12] A.V. Olinto. *AstroParticle Physics at the Highest Energies*. arXiv:1202.0355v2 [astro-ph.HE].
- [13] C. Grupen. *Astroparticle Physics*. 1st ed. Springer, 2005.

- [14] J. L. Han. *The Large-Scale Magnetic Field Structure of Our Galaxy: Efficiently Deduced from Pulsar Rotation Measures*. The Magnetized Interstellar Medium (2004), p. 3.
- [15] M. S. Longair. *High Energy Astrophysics. 3rd ed.* Cambridge University Press, 2011.
- [16] A. R. Bell and S. G. Lucek. *Mon. Not. R. Astron. Soc.* 321, 433–438 (2001).
- [17] P. L. Biermann, and J. P. Cassinelli, *Astron. Astrophys.*,1993, 277, 691.
- [18] R. Budnik, B. Katz, A. MacFadyen, and E. Waxman, *ApJ*, 2008, 673, 928–933.
- [19] Todor Stanev, *Ultra High Energy Cosmic Rays*, SLAC Summer Institute on Particle Physics (SSI04), Aug. 2-13, 2004.
- [20] J.W. Cronin, arXiv:astro-ph/0402487.
- [21] Jörg R. Hörandel, arXiv:astro-ph/0501251v1.
- [22] T. Gaisser. *Cosmic Rays and Particle Physics*. Cambridge University Press, 1990.
- [23] D.C. Ellison, S.P. Reynolds and F.C. Jones. *First-order Fermi particle acceleration by relativistic shocks*. *Astrophys. J.* 360 (Sept. 1990), pp. 702–714.
- [24] W. Blaade and F. Zwicky , *Phys. Rev.* 46 (1934) 76.
- [25] V.L. Ginzburg and S.I. Syrovatskii, *The origin of Cosmic Rays*. Macmillan (1964).
- [26] D.H. Perkins *Particle Astrophysics*. Oxford University Press, 2003.
- [27] Bell A., *Mon. Not. Roy. Astron. Soc.* 182, 147, 443 (1978).
- [28] R. D. Blandford and J. P. Ostriker *Astrophys. J.* 221, L29 (1978).
- [29] L. D. Landau and E. M. Lifshitz *Fluid mechanics*. Oxford: Pergamon Press (1978).

- [30] P.O. Lagage and C.J. Cesarsky, 1983. *The maximum energy of cosmic rays accelerated by supernova shocks*. *Astron. Astrophys.* 125 249–257.
- [31] E.G. Berezhko , *Astropart. Phys.* 5 (1999) 367.
- [32] A.M. Hillas, *Ann. Rev. Astron. Astrophys.*, 22, 425 (1984).
- [33] M. Ahlers, L. A. Anchordoqui, J. K. Becker, T. K. Gaisser, F. Halzen, D. Hooper, S. R. Klein. P. Mészáros, S. Razzaque, and S. Sarkar, FERMILAB-FN-0847-A, YITP-SB-10-01.
- [34] A. W. Strong, I. V. Moskalenko , 1998, *ApJ*, 509, 212.
- [35] V. S. Berezhinskii, S. V. Bulanov, V. A. Dogiel, V. S. Ptuskin *Astrophysics of cosmic rays*. edited by V. L. Ginzburg, Amsterdam (1990).
- [36] R. Schlickeiser *Cosmic ray astrophysics*. Astronomy and Astrophysics Library. Berlin: Springer (2002).
- [37] M. S. Longair, *High Energy Astrophysics, Vol. 2: Stars, the Galaxy and the Interstellar Medium* Cambridge University Press (2008).
- [38] A. Obermeier et al. , *Galactic propagation of cosmic rays and the B/C ratio*, Proceeding of the 32nd International Cosmic Ray Conference, Beijing 2011.
- [39] N. E. Yanasak et al. , *Astrophys. J.* 563:768 (2001).
- [40] A. W. Strong and I. V. Moskalenko, arXiv:astro-ph/0101068v1 4 Jan 2001.
- [41] S. Stephens and R. Streitmatter, *Astrophys. J.* 505 (1998) 266.
- [42] B. Wiebel-Soth et al., *Astron. & Astroph.* 330 (1998) 389.
- [43] S. Torii et al. *The Calorimetric Electron Telescope (CALET) for High Energy Astroparticle Physics on the International Space Station* 33rd International Cosmic Ray Conference, Rio de Janeiro 2013.
- [44] K. Yamaoka et al. *CALET Gamma-ray Burst Monitor (CGBM)* Proceeding of the 33rd International Cosmic Ray Conference, Rio de Janeiro 2013.

- [45] Y. Shimizu, *The CALET CHD for determination of nuclear charge*, Proceeding of the 32nd International Cosmic Ray Conference, Beijing 2011.
- [46] R. Dwyer et al., *Nuclear Instruments and Methods in Physics Research, Section A* 242 (1985) 171.
- [47] P. S. Marrocchesi et al., *Nuclear Instruments and Methods in Physics Research, Section A* 659 (2011) 477–483.
- [48] S. Bonechi, *Charge Identification of Cosmic Nuclei with the CALET Electron Telescope on the ISS* Ph.D. Thesis.
- [49] T. Yamashita et al., *Performance of 64-multi-anode photomultiplier and scintillating fiber for the CALET detector* 28th International Cosmic Ray Conference, Tsukuba 2003.
- [50] T. Tamura et al., *Development of a PMT Readout System with Viking Chips for the SciFi Detector of CALET* 28th International Cosmic Ray Conference, Tsukuba 2003.
- [51] S. Torii et al. *Development of front-end electronics with large dynamic range for space applications* Nuclear Physics B - (Proc. Suppl.) 150 (2006) 390–393.
- [52] I. Daijito et al., *High-dynamic range readout system using dual APD/PD for the CALET-TASC* Proceedings of the 32nd International Cosmic Ray Conference, Beijing 2011.
- [53] CALET D.H.&A. Japan *CALET Trigger System* CALET internal note WCOC-2015-001NC.
- [54] J.D. Sullivan, *Geometrical factor and directional response of single and multi-element particle telescopes* Nuclear Instruments and Methods 95 5 (1971).
- [55] *EPICS web page* <http://cosmos.n.kanagawa-u.ac.jp/EPICSHome/>
- [56] *COSMOS web page* <http://cosmos.n.kanagawa-u.ac.jp/COSMOSHome/>
- [57] *The official FLUKA site* www.fluka.org/

- [58] *Geant4 web page* <http://geant4.cern.ch>.
- [59] A. Capella et al., Phys. Rep. 236 (1994) 225.
- [60] S. Roesler, R. Engel and J. Ranft *The Monte Carlo event generator DPMJET-III* Proc. Monte Carlo 2000 Conference, Lisbon, October 23–26 2000,
- [61] H. Sorge, H. Stoecker and W. Greiner *Poincarè invariant Hamiltonian dynamics: Modelling multi-hadronic interactions in a phase space approach* Ann. Phys. 192, 266-306 (1989)
- [62] M.B. Emmett, *The MORSE Monte Carlo radiation transport system* Oak Ridge National Laboratory report ORNL-4972 (1975).
- [63] F. Palma, *Study of the performance of the CALET calorimeter-based orbital observatory for High-Energy Astroparticle Physics*, Ph.D. Thesis.
- [64] F. Aharonian et al., *Probing the ATIC peak in the cosmic-ray electron spectrum with H.E.S.S.* Astron. Astrophys. 508 561–564 (2009).
- [65] M. Aguilar et al., *Precision Measurement of the Proton Flux in Primary Cosmic Rays from Rigidity 1 GV to 1.8 TV with the Alpha Magnetic Spectrometer on the International Space Station* Phys. Rev. Lett. 114, 171103 (2015). doi:10.1103/PhysRevLett.114.171103
- [66] C.S. Shen et al. 1971, Astrophys. Lett., 9, 169.
- [67] T. Kobayashi et al. 2004, Astrophys.J., 601, 340.
- [68] K. Yoshida, *The science objectives for CALET*. Proceedings of the 32nd International Cosmic Ray Conference, Beijing 2011.
- [69] O. Adriani et al., 2011. *Cosmic-Ray Electron Flux Measured by the PAMELA Experiment between 1 and 625 GeV*. Physical Review Letters 106(20) 201101.
- [70] S. Torii et al., 2008. *High-energy electron observations by PPB-BETS flight in Antarctica*. ArXiv e-prints.

- [71] J. Chang et al., 2008. *An excess of cosmic ray electrons at energies of 300-800 GeV*. Nature 456 362–365.
- [72] F. Aharonian et al., 2009. *Probing the ATIC peak in the cosmic-ray electron spectrum with H.E.S.S.* Astron. Astrophys. 508 561564.
- [73] M. Ackermann et al., 2010. *Fermi LAT observations of cosmic-ray electrons from 7 GeV to 1 TeV*. Physical Review D 82(9) 092004.
- [74] W.B. Atwood et al. , Ap. J., 2009, 697: 1071–1102.
- [75] S. Torii, *CALET collaboration meeting*.
- [76] K. Yoshida, S. Torii et al., *Scientific Performance of the CALET Instrument for the 20MeV-10TeV Gamma-ray Observation*. Proceedings of the 28nd International Cosmic Ray Conference, Tsukuba 2003.
- [77] F. Zwicky, 1933. *Die Rotverschiebung von extragalaktischen Nebeln*. Helvetica Physica Acta 6 110–127.
- [78] G. Jungman, M. Kamionkowski and K. Griest, 1996. *Supersymmetric dark matter*. Phys. Rept 267 195–373.
- [79] L. Bergström, 2000. *Non-baryonic dark matter: observational evidence and detection methods*. Reports on Progress in Physics 63 793841.
- [80] G. Bertone, D. Hooper and J. Silk, 2005. *Particle dark matter: evidence, candidates and constraints*. Phys. Rept 405 279390.
- [81] H. Cheng, J.L. Feng and K.T. Matchev, 2002. *Kaluza-Klein Dark Matter*. Physical Review Letters 89(21) 211301.
- [82] A. Ibarra, D. Tran and C. Weniger, 2010. *Decaying dark matter in light of the PAMELA and Fermi LAT data*. Journal of Cosmology and Astroparticle Physics 1 9.
- [83] S. Torii, *CALET Mission on JEM/EF of the ISS*. J. Phys. Soc. Jpn. 78 (2009) Suppl. A, pp. 68–73.

- [84] P. Maestro, *Journal of Physics: Conference Series* 409 (2013) 012026, doi:10.1088/1742-6596/409/1/012026.
- [85] P. Blasi, E. Amato and P.D. Serpico, 2012. *Spectral Breaks as a Signature of Cosmic Ray Induced Turbulence in the Galaxy*. *Physical Review Letters* 109(6) 061101.
- [86] P.S. Marrocchesi et al, *CALET measurements with cosmic nuclei and performance of the charge detectors*. Proceeding of the 33nd International Cosmic Ray Conference, Rio de Janeiro 2013.
- [87] B.F. Rauch et al., *Predicted CALET Measurements of Heavy and Ultra-Heavy Cosmic Ray Nuclei* Proceeding of the 34nd International Cosmic Ray Conference, The Hague 2015.
- [88] B.F. Rauch et al., *Cosmic Ray origin in OB Associations and Preferential Acceleration of Refractory Elements: Evidence from Abundances of Elements $_{26}\text{Fe}$ through $_{34}\text{Se}$* . *ApJ*, 697 (2009) 2083-2088, [arXiv:0906.2021].
- [89] R. Frühwirth, *Application of Kalman filtering to track and vertex finding*, *NIM A*, 262 (1987), 444-450.
- [90] A. Strandlie and R. Frühwirth, *Track and vertex reconstruction: From classical to adaptive methods*, *Rev. Mod. Phys.*, 82 (2010), 1419-1458.
- [91] S. Eidelman et al. (Particle Data Group), *Phys. Lett. B* 592, 1 (2004).
- [92] D. Maurin, F. Melot and R. Taillet, *A database of charged cosmic rays*, *A&A* 569, A32 (2014).
- [93] A.G. Frodesen, O. Skjeggstad and H. Tøfte, *Probability and statistics in particle physics* Universitetsforlaget 1979 ISBN: 88-00-01906-3
- [94] Shiu-Hang Lee et al. 2012 *ApJ* 750 156, doi:10.1088/0004-637X/750/2/156.
- [95] O. Adriani et al., *Science* 332 (2011) 69

- [96] S. Haino et al., *Precision Measurement of the Helium Flux in Primary Cosmic Rays of 1.9 GV to 3 TV Rigidity with the Alpha Magnetic Spectrometer on the International Space Station* PoS(ICRC2015)236.
- [97] J. Blümer, R. Engel, J.R. Hörandel. *Progress in Particle and Nuclear Physics* 63 (2009) 293 (arXiv:0904.0725).
- [98] M. Amenomori, *Astrophys. Space Sci. Trans.*, 7, 15–20, 2011.
- [99] K. Asakimori et al., *ApJ* 502 (1998) 278.
- [100] V. A. Derbina et al. 2005, *ApJ*, 628, L41.
- [101] Y.S. Yoon et al., *ApJ* 728 (2011) 122.
- [102] M. Aguilar et al. 2002, *Phys. Rep.*, 366, 331.
- [103] S. Haino et al. 2004, *Phys. Lett. B*, 594, 35.
- [104] M. Boezio et al. 2003, *Astropart. Phys.*, 19, 583.
- [105] A. D. Panov et al. 2009, *Bull. Russ. Acad. Sci. Phys.*, 73, 564.
- [106] P. Maestro, *Cosmic rays: direct measurements* PoS(ICRC2015)016.
- [107] M. Boezio, M. Martucci, A. Bruno, V. Di Felice and R. Munini, *Nine Years of Cosmic Ray Investigation by the PAMELA Experiment* PoS(ICRC2015)037.
- [108] Y.M. Butt, A.M. Bykov, *ApJ* 677 (2008) L21.
- [109] E. Parizot et al., *A&A* 424 (2004) 747.
- [110] S. Thoudam, J. R. Hrandel, *A&A* 567 (2014) A33.
- [111] D.C. Ellison, E.G. Berezhko, M.G. Baring, *ApJ* 540 (2000) 292.
- [112] V. Ptuskin, V. Zirakashvili, E.S. Seo, *ApJ* 763 (2013) 47.
- [113] N. Tomassetti, *Inhomogeneous diffusion model for recent data on high-energy cosmic rays* Pos(ICRC2015) 551.

- [114] L. Nava et al., *Non-linear Cosmic Ray propagation close to the acceleration site* Pos(ICRC2015) 541.
- [115] S. Thoudam, J. R. Hrandel, MNRAS 435 (2013) 2532.
- [116] W. Liu, P. Salati, X. Chen, Res. Astron. Astrophys. 15 (2015) 1.
- [117] Y. Zhang et al., *On the primary model to explain the relation between a rigidity-dependent spectral hardening of proton and helium spectra and a sharp knee of the all-particle spectrum* Pos(ICRC2015) 546.
- [118] N. Tomassetti, *Consistent description of leptonic and hadronic spectra in cosmic rays* Pos(ICRC2015) 552.
- [119] V.I. Zatsepin, N.V. Sokolskaya, A&A 458 (2006). 1
- [120] M.A. Malkov et al., PRL 108 (2012) 081104.
- [121] L.O. Drury, MNRAS 415 (2011) 1807.
- [122] Y. Ohira, K. Ioka, ApJ 729 (2011) L13.
- [123] P. Blasi, E. Amato, JCAP 1201 (2012) 011.
- [124] A. Obermeier et al., *Measuring the energy of cosmic-ray helium with the TRD of AMS-02* Pos(ICRC2015) 286.
- [125] E.S. Seo, *Cosmic Ray Energetics And Mass: from balloons to the ISS* Pos(ICRC2015) 574.
- [126] D. F. Smart and M. A. Shea *Cosmic ray exposure factors for shuttle altitudes derived from calculated cut-off rigidities* Adv. Space Res. Vol.4, No.10, pp.161–164, 1984.
- [127] A. Chandra *Energy spectrum of the primary cosmic rays in the range 10 GeV–10 TeV* PoS(ICRC2015) 235.
- [128] J. Buckley et al., 1994, *A new measurement of the flux of the light Cosmic-Ray nuclei at high energies* ApJ, 429, 736.

-
- [129] G.D. Lafferty and T.R. Wyatt, *Where to stick your data points: The treatment of measurements within wide bins* 1995, Nucl. Instrum. Methods. A, 355, 541
- [130] P. Brogi et al. *CALET measurements with cosmic nuclei: expected performances of tracking and charge identification* PoS(ICRC2015) 595.
- [131] P.S. Marrocchesi et al. *Conceptual design of a charge identifier array for cosmic ray composition measurements in CALET* Proceedings of the 30th International Cosmic Ray Conference, Merida 2007, vol. 2, 301–304.
- [132] P.S. Marrocchesi et al. *A silicon array for cosmic-ray composition measurements in CALET* J. Phys. Soc. Jpn. 78 (2009) Suppl. A, 181-183.
- [133] P.S. Marrocchesi et al. *An high resolution FDIRC for the measurement of cosmic-ray isotopic abundances* Astroparticle Physics 35 (2011) 21–27.
- [134] P.S. Marrocchesi et al. *Digital FDIRC: a Focused Differential Internal Reflection Cherenkov imaged by SiPM arrays* forthcoming on Nucl. Instrum. Methods.